



저작자표시-비영리-변경금지 2.0 대한민국

이용자는 아래의 조건을 따르는 경우에 한하여 자유롭게

- 이 저작물을 복제, 배포, 전송, 전시, 공연 및 방송할 수 있습니다.

다음과 같은 조건을 따라야 합니다:



저작자표시. 귀하는 원저작자를 표시하여야 합니다.



비영리. 귀하는 이 저작물을 영리 목적으로 이용할 수 없습니다.



변경금지. 귀하는 이 저작물을 개작, 변형 또는 가공할 수 없습니다.

- 귀하는, 이 저작물의 재이용이나 배포의 경우, 이 저작물에 적용된 이용허락조건을 명확하게 나타내어야 합니다.
- 저작권자로부터 별도의 허가를 받으면 이러한 조건들은 적용되지 않습니다.

저작권법에 따른 이용자의 권리는 위의 내용에 의하여 영향을 받지 않습니다.

이것은 [이용허락규약\(Legal Code\)](#)을 이해하기 쉽게 요약한 것입니다.

[Disclaimer](#)

**Doctor of Engineering**

**2D QUANTUM DOTS COMPOSITES WITH NICKEL-  
BASED MATERIALS FOR ENERGY STORAGE  
DEVICES**

**The Graduate School of the University of Ulsan**

**Department of Chemical Engineering**

**HONG YIWEN**

**2D QUANTUM DOTS COMPOSITES WITH NICKEL-  
BASED MATERIALS FOR ENERGY STORAGE  
DEVICES**

Supervisor: Won Mook Choi

A Dissertation

Submitted to  
The Graduate School of the University of Ulsan  
In partial Fulfillment of the Requirements  
For the Degree of

Doctor of Engineering

By

HONG YIWEN

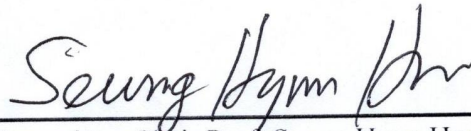
Department of Chemical Engineering

University of Ulsan, Korea

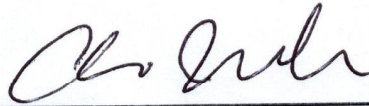
August 2021

**2D QUANTUM DOTS COMPOSITES WITH NICKEL-  
BASED MATERIALS FOR ENERGY STORAGE  
DEVICES**

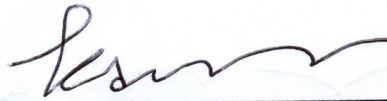
This certifies that the dissertation thesis  
of HONG YIWEN is approved



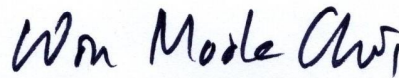
Committee Chair Prof. Sueng Hyun Hur




Committee Member Prof. Jin Suk Chung



Committee Member Prof. Sung Gu Kang



Committee Member Prof. Won Mook Choi



Committee Member Prof. Jing Xia Yang

Department of Chemical Engineering

University of Ulsan, Korea

August 2021

## ACKNOWLEDGEMENTS

I would like to convey my sincerest gratitude and respect to my supervisors, Prof. Choi Won Mook for his precious guidance and constant support during PhD study at School of Chemical Engineering, University of Ulsan. It is inspiring for me that he is always overflowed with enthusiasm and energy for research. When I was confused with my research or meeting difficulty during experiment, professor usually gave me some suggestion.

I am grateful for other professors in our school that they have instructed me many knowledges as assistant to complete my research more easily. And also, I want to thank other members in our lab, Dr. Tran Van Tam and Ms. Liu Di, for their kind help and cooperation in my research work.

I extend my thanks for Prof. Xu Jingli and Prof. Yang Jingxia for their taking care of me during my visit study in Shanghai University of Engineering Science latest two years. They have shared the research experience, provided experiment equipment for me and gave warm hospitality and valuable suggestions. I am also thankful to Prof. Wang Jinjie, Ms. Shi Yunjing, Ms. Li Xia, Ms. Zhang Huiqing and Mr. Zou Bingjie in Department of Chemical Engineering for their support regarding characterization measurements.

I also thank for my mother Ms. Tian HeXiang and my boyfriend Mr. Wu ZeQin for their supporting my advance study in these five years.

Finally, I gratefully acknowledge Basic Science Research Program through the National Research Foundation of Korea (NRF) funded by The Ministry of Education and Research Fund of the University of Ulsan for providing financial support.

## ABSTRACT

For increasing the electrochemical properties of lithium-ion batteries and supercapacitors, we have developed several kinds of electrode materials by environment-friendly methods. One of composite materials is p-type semiconductor nickel oxide/hydroxide, the other is n-type semiconductor of quantum dots. In this my doctor subjects, there are four topics about 2D quantum dots composites with nickel-based materials. The composites were further used as a supercapacitor electrode or lithium-ion battery anode, and their electrochemical properties were checked by electrochemical workstation, that exhibited outstanding cycling performance.

In first part, we prepared hierarchical nanostructured NiO (h-NiO) microtubes by a simple wet-chemical synthesis without the use of template or surfactant, followed by the calcination of  $\alpha$ -Ni(OH)<sub>2</sub> precursor. As anode electrode of Li-ion batteries, the h-NiO microtubes deliver largely enhanced cycle capacity of 770 mAh/g at a current density of 0.5 C (1 C= 717 mA/g) after 200 cycles and extremely high columbic efficiency of 98.8%, as compared to the NiO rods. In second part, we have composites graphene quantum dots (GQDs)/Ni(OH)<sub>2</sub> on carbon cloth (G-NH//CC) prepared through simple hydrothermal reactions. It has a maximum specific capacitance of 1825 F/g at 1 A/g and a high energy density of 80.8 Wh/kg at 2021 W/kg. In third part, boron doping g-C<sub>3</sub>N<sub>4</sub> quantum dots (B-CNQDs) were synthesized by KOH cutting. Then adsorbed on the surface Ni(OH)<sub>2</sub> nanoflowers by impregnation method. The best B-CNQD<sub>x</sub>-Ni sample has an excellent specific capacitance of 1700 F/g at 1.5 A/g. Finally, Mxene quantum dots were synthesized by hydrothermal reactions with microwave assistant with different solvent. The best MQD-Ni//Ni foam sample has an excellent specific capacitance of 1660 F/g at 1 A/g.

# TABLE OF CONTENTS

<b>ACKNOWLEDGEMENTS</b> .....	<b>I</b>
<b>ABSTRACT</b> .....	<b>II</b>
<b>TABLE OF CONTENTS</b> .....	<b>III</b>
<b>LIST OF FIGURES</b> .....	<b>V</b>
<b>LIST OF TABLES</b> .....	<b>IX</b>
<b>CHAPTER 1: INTRODUCTION</b> .....	<b>1</b>
1.1 LITHIUM-ION BATTERIES AND SUPERCAPACITORS.....	1
1.2 NICKEL BASED MATERIALS .....	6
1.3 QUANTUM DOTS .....	6
1.4 THE OBJECTIVES OF THESIS .....	8
1.5 THE ORGANIZATION OF THESIS.....	8
<b>CHAPTER 2: LITERATURE REVIEW</b> .....	<b>11</b>
2.1 INTRODUCTION.....	11
2.2 NICKEL-BASED MATERIALS FOR LITHIUM-ION BATTERIES AND SUPERCAPACITORS .....	11
2.3 QUANTUM DOTS FOR LITHIUM-ION BATTERIES AND SUPERCAPACITORS .....	15
2.3.1 Graphene Quantum dots.....	16
2.3.2 g-C <sub>3</sub> N <sub>4</sub> quantum dots (CNQDs).....	17
2.3.3 Mxene quantum dots (MQDs).....	17
2.4 SUMMARY .....	17
<b>CHAPTER 3: EXPERIMENTAL SECTION</b> .....	<b>19</b>
3.1 MATERIALS .....	19
3.2 SYNTHESIS OF COMPOSITES .....	19
3.2.1 Hierarchical nanostructured NiO (h-NiO) microtubes .....	19
3.2.2 Graphene quantum dots (GQDs)/Ni(OH) <sub>2</sub> composites on carbon cloth (G-NH//CC).....	20
3.2.3 Boron doped g-C <sub>3</sub> N <sub>4</sub> quantum dots (B-CNQDs) coating on Ni(OH) <sub>2</sub> nanoflowers (B-CNQD <sub>x</sub> -Ni).....	20
3.2.4 Mxene quantum dots (MQDs) compositing with Ni(OH) <sub>2</sub> on Ni foam (M-NH//NF) .....	21
3.3 CHARACTERIZATIONS.....	22
3.3.1 X-ray photoelectron spectroscopy (XPS) .....	22
3.3.2 X-ray diffraction (XRD).....	24
3.3.3 Fourier-transform Infrared Spectroscopy (FT-IR).....	26
3.3.4 Scanning Electron Microscope (SEM) and Transmission Electron Microscope (TEM) .....	27
3.4 ELECTROCHEMICAL MEASUREMENTS .....	29
3.4.1 Lithium-ion batteries.....	29
3.4.2 Supercapacitors.....	31
3.4.3 Electrochemical impedance spectroscopy (EIS).....	31
3.4.4 Calculations of electrochemical performance.....	33

<b>CHAPTER 4: HIERARCHICAL NiO (H-NiO) MICROTUBES FOR LITHIUM-ION BATTERIES .....</b>	<b>35</b>
4.1 INTRODUCTION .....	35
4.2 MORPHOLOGIES AND STRUCTURES .....	36
4.3 ELECTROCHEMICAL PERFORMANCE .....	42
4.4 SUMMARY .....	45
<b>CHAPTER 5: GRAPHENE QUANTUM DOTS/Ni(OH)<sub>2</sub> NANOCOMPOSITES ON CARBON CLOTH FOR SUPERCAPACITORS .....</b>	<b>47</b>
5.1 INTRODUCTION .....	47
5.2 MORPHOLOGIES AND STRUCTURES .....	49
5.3 THREE ELECTRODES SYSTEM .....	53
5.4 TWO ELECTRODES SYSTEM .....	58
5.5 SUMMARY .....	60
<b>CHAPTER 6: BORON DOPED G-C<sub>3</sub>N<sub>4</sub> QUANTUM DOTS/ Ni(OH)<sub>2</sub> NANOCOMPOSITES ON NICKEL FOAM FOR SUPERCAPACITORS .....</b>	<b>62</b>
6.1 INTRODUCTION .....	62
6.2 MORPHOLOGIES AND STRUCTURES .....	63
6.3 ELECTROCHEMICAL PERFORMANCE .....	72
6.4 SUMMARY .....	77
<b>CHAPTER 7: MXENE QUANTUM DOTS/ Ni(OH)<sub>2</sub> NANOCOMPOSITES ON NICKEL FOAM FOR SUPERCAPACITORS .....</b>	<b>78</b>
7.1 INTRODUCTION .....	78
7.2 MORPHOLOGIES AND STRUCTURES .....	79
7.3 ELECTROCHEMICAL PERFORMANCE .....	82
7.4 SUMMARY .....	84
<b>CHAPTER 8: SUMMARY .....</b>	<b>85</b>
8.1 CONCLUSION .....	85
8.2 RECOMMENDATION .....	86
<b>REFERENCE .....</b>	<b>87</b>
<b>LIST OF PUBLICATIONS .....</b>	<b>98</b>
<b>요약 .....</b>	<b>99</b>



## LIST OF FIGURES

<b>Figure 1.1</b> Industry estimates of economically viable fossil fuel reserves .....	1
<b>Figure 1.2</b> The comparison of energy density and power density for different energy storage devices .....	2
<b>Figure 1.3</b> The operation of a Li-ion battery during discharging and charging .....	3
<b>Figure 1.4</b> Schematic diagrams of (a) an electrostatic capacitor, (b) an electric double-layer capacitor, (c) pseudocapacitor and (d) lithium-ion capacitor .....	4
<b>Figure 1.5</b> Some properties of QDs for electrochemical applications.....	7
<b>Figure 2.1</b> Advantages of using carbonaceous materials .....	13
<b>Figure 2.2</b> HRTEM image and PL spectra of GQDs according to their diameters .....	16
<b>Figure 3.1</b> The schematic of X-ray photoelectron spectroscopy.....	24
<b>Figure 3.2</b> The explanation of Bragg's law in detail .....	25
<b>Figure 3.3</b> A schematic of an interferometer used in a Fourier Transfer Infrared Spectrometer (FTIR).....	26
<b>Figure 3.4</b> Structure diagram of scanning electron microscope (SEM) .....	27
<b>Figure 3.5</b> The Nyquist plots model and inset equivalent circuit diagram .....	32
<b>Figure 4.1</b> FE-SEM image of the obtained Ni(OH) <sub>2</sub> precursor products at the different reaction time. (a) 0.5 hr, (b) 1 hr, (c) 3 hr, and (d) 4 hr.....	37
<b>Figure 4.2</b> (a) XRD patterns of the obtained Ni(OH) <sub>2</sub> precursor products at the different reaction time, (b-c) TGA curves of Ni(OH) <sub>2</sub> nanorods and h-Ni(OH) <sub>2</sub> .....	38
<b>Figure 4.3</b> (a) XRD patterns of the h-Ni(OH) <sub>2</sub> and h-NiO. (b) FE-SEM image of the h-NiO and (c) its high magnified image .....	40
<b>Figure 4.4</b> (a) TEM image and (b) HR-TEM image of h-NiO microtubes. (c) Nitrogen adsorption-desorption isothermal of h-NiO microtubes and NiO rods .....	41
<b>Figure 4.5</b> Cyclic voltammetry curves of (a) h-NiO microtubes and (b) NiO rods ....	43
<b>Figure 4.6</b> (a) The cycle performance and (b) the rate performance of h-NiO microtubes and NiO rods .....	44
<b>Figure 4.7</b> Nyquist plots of fresh electrode and after five cycles for (a) h-NiO	

microtubes and (b) NiO rods.....	45
<b>Figure 5.1</b> Schematic illustration for the synthesis of GQDs/Ni(OH) <sub>2</sub> nanocomposite on carbon cloth .....	49
<b>Figure 5.2</b> (a) Raman spectra and (b) FT-IR spectra of the as-synthesized GQDs .....	50
<b>Figure 5.3</b> (a-b) SEM images of pristine CC. (c) Photo images of pristine CC and as-synthesized G-NH//CC .....	50
<b>Figure 5.4</b> (a-c) SEM images of G-NH//CC nanocomposite. (d) TEM image of G-NH//CC and (e) its high magnification image. (f) EDS elementary mapping of G-NH//CC .....	51
<b>Figure 5.5</b> (a-b) SEM images and (c-d) TEM images of NH//CC. (e) XRD spectra of GNH//CC and NH//CC .....	52
<b>Figure 5.6</b> (a) The XPS survey scan of G10-NH//CC and NH//CC. (b) High resolution C 1s and (c) Ni 2p XPS spectrum of G10-NH//CC.....	53
<b>Figure 5.7</b> (a) CV curves of different G-NH//CC composites and NH//CC. (b) CV curves of G10-NH//CC at different scan rates .....	54
<b>Figure 5.8</b> (a) Galvanostatic charge-discharge curves of different G-NH//CC composites and NH//CC, (b) galvanostatic charge-discharge curves of G10-NH//CC at different current densities. (c) Obtained specific capacitance of G10-NH//CC at different current densities. (d) Nyquist plots of G10-NH//CC and NH//CC .....	54
<b>Figure 5.9</b> Specific capacitance comparison of the prepared electrodes at different current densities.....	56
<b>Figure 5.10</b> (a) Specific capacitance retention of G10-NH//CC and NH//CC. (b) Nyquist plots of G10-NH//CC and NH//CC after 2000 cycles.....	57
<b>Figure 5.11</b> SEM images of G10-NH//CC electrode after 2000 cycles (a-b) and 8000 cycles (c-d).....	57
<b>Figure 5.12</b> Simplified energy band diagram of GQDs and Ni(OH) <sub>2</sub> (a) before contact and (b) after contact.....	58
<b>Figure 5.13</b> (a) Schematic illustration of all-solid-state symmetric supercapacitor using	

G-NH//CC electrodes and photo images of the bending state. (b) CV curves at different scan rates and (c) galvanostatic charge-discharge curves at different current densities of the G-NH//CC SSC. (d) The Ragone plots of the G-NH//CC SSC and reported Ni(OH) <sub>2</sub> -based supercapacitors. (e) CV curves of the G-NH//CC SSC at different bending states. (f) Photo image of lighting LED bulb powered by two G-NH//CC SSCs in series .....	60
<b>Figure 6.1</b> Diagram illustration for the synthesis of B-CNQD <sub>x</sub> -Ni nanoflowers .....	63
<b>Figure 6.2</b> (a) XRD pattern of B-C <sub>3</sub> N <sub>4</sub> and g- C <sub>3</sub> N <sub>4</sub> ; (b) FT-IR pattern of B-C <sub>3</sub> N <sub>4</sub> and g- C <sub>3</sub> N <sub>4</sub> ; (c) PL spectrum of B-CNQDs and CNQDs .....	65
<b>Figure 6.3</b> XRD pattern of Ni(OH) <sub>2</sub> and B-CNQD <sub>x</sub> -Ni.....	66
<b>Figure 6.4</b> (a) SEM images of Ni(OH) <sub>2</sub> nanoflowers, (b) SEM images of B-CNQD10-Ni nanocomposites, (c) TEM and (d) HRTEM images of B-CNQD10-Ni nanocomposites .....	67
<b>Figure 6.5</b> Zeta Potential Power spectra obtained from B-doped g-C <sub>3</sub> N <sub>4</sub> quantum dots and Ni(OH) <sub>2</sub> (a) standing after 1 day, (b) standing after 5 days.....	67
<b>Figure 6.6</b> (a) BET-N <sub>2</sub> adsorption/desorption isotherm and (b) Poresize distribution of B-CNQD10-Ni and Ni(OH) <sub>2</sub> .....	68
<b>Figure 6.7</b> (a) The XPS survey scan of B-CNQD10-Ni and Ni(OH) <sub>2</sub> . (b) High resolution Ni 1s, (c) B 1s and (d) C 1s XPS spectrum of B-CNQD10-Ni.....	69
<b>Figure 6.8</b> The XPS survey scan of B-C <sub>3</sub> N <sub>4</sub> and g-C <sub>3</sub> N <sub>4</sub> .....	70
<b>Figure 6.9</b> UV-Vis diffuse reflectance spectra (a) and Kubelka-Munk plot (b) for estimating bandgap energy of Ni(OH) <sub>2</sub> and B-CNQD10-Ni. (c) PL emission spectra of pure Ni(OH) <sub>2</sub> and B-CNQD10-Ni.....	71
<b>Figure 6.10</b> Sketch of charge transfer between B-CNQDs and Ni(OH) <sub>2</sub> .....	72
<b>Figure 6.11</b> CV curves of (a) B-CNQD10-Ni and (b) Ni(OH) <sub>2</sub> at a scan rate of 10-200 mV·s <sup>-1</sup> ; (c) Capacitances as a function of scan rate; (d) Nyquist plots and insets show the enlarged Nyquist plots at high to medium frequencies.....	74
<b>Figure 6.12</b> (a) GCD curve of Ni(OH) <sub>2</sub> and B-CNQD <sub>x</sub> -Ni nanocomposites at 1.5 A·g <sup>-1</sup> ; GCD curves of (b) B-CNQD10-Ni and (c) Ni(OH) <sub>2</sub> at different current densities	

of 1.5-12 A·g <sup>-1</sup> ; (d) cycling specific capacitance retention of Ni(OH) <sub>2</sub> and B-CNQD <sub>x</sub> -Ni, (e-f) SEM images of Ni(OH) <sub>2</sub> after 1000 cycles in 1 M KOH, (g-h) SEM images of B-CNQD10-Ni after 1000 cycles in 2 M KOH.....	76
<b>Figure 7.1</b> Diagram illustration for the synthesis of M-NH//NF.....	79
<b>Figure 7.2</b> FT-IR pattern of (a) Mxene and (b) Ni(OH) <sub>2</sub> , e-MQDs-Ni, f-MQDs-Ni and o- e-MQDs-Ni .....	79
<b>Figure 7.3</b> XRD pattern of f-MQDs-Ni and Ni(OH) <sub>2</sub> .....	80
<b>Figure 7.4</b> The spectra of UV–vis absorption, maximum excitation (EX) and emission (EM) peaks of the as-prepared f-MQDs .....	80
<b>Figure 7.5</b> SEM images of (a) Bare Ni foam, (b) e- M-NH//NF, (c) f- M-NH//NF, (d) o-M-NH//NF .....	81
<b>Figure 7.6</b> CV curve of (a) NH//NF, (b) f- M-NH//NF, (c) e-M-NH//NF and (d) o-M-NH//NF .....	82
<b>Figure 7.7</b> CV curve of (a) 0.5% f- M-NH//NF, (b) 2% f- M-NH//NF .....	83
<b>Figure 7.8</b> GCD curve of (a) NH//NF and (b) f- M-NH//NF .....	84

## LIST OF TABLES

<b>Table 2.1</b> Nickel-base materials with different morphology and their electrochemical performance.....	14
<b>Table 3.1</b> FTIR frequency range and functional groups .....	27
<b>Table 3.2</b> Comparison for the properties of different microscope.....	29
<b>Table 4.1</b> Surface properties of nickel hydroxide and its calcined products.....	41
<b>Table 5.1</b> Electrochemical performance of recently Ni(OH) <sub>2</sub> -Carbon materials.....	48
<b>Table 7.1</b> the specific capacitance of NH//NF, f- M-NH//NF, e-M-NH//NF and o-M-NH//NF calculated by CV curve with different scan rate (F/g) .....	83

## Chapter 1: Introduction

This chapter gives a brief introduction of nickel-based materials, quantum dots and electrochemical devices as lithium-ion battery and supercapacitor. In a manner of speaking, energy storage devices, especially lithium-ion battery and supercapacitor, are catching trend for world energy demand during decade. They play a vital role in the energy exploration and environment protection cause. The background, mechanism and classify of lithium-ion battery and supercapacitor have been introduced in this chapter. Subsequently, the development and the intrinsic properties of quantum dots (graphene, g-C<sub>3</sub>N<sub>4</sub> and Mxene) and nickel-based materials are also be discussed. Finally, the objectives and organization of thesis are articulation in the last part of this chapter.

### 1.1 lithium-ion batteries and Supercapacitors

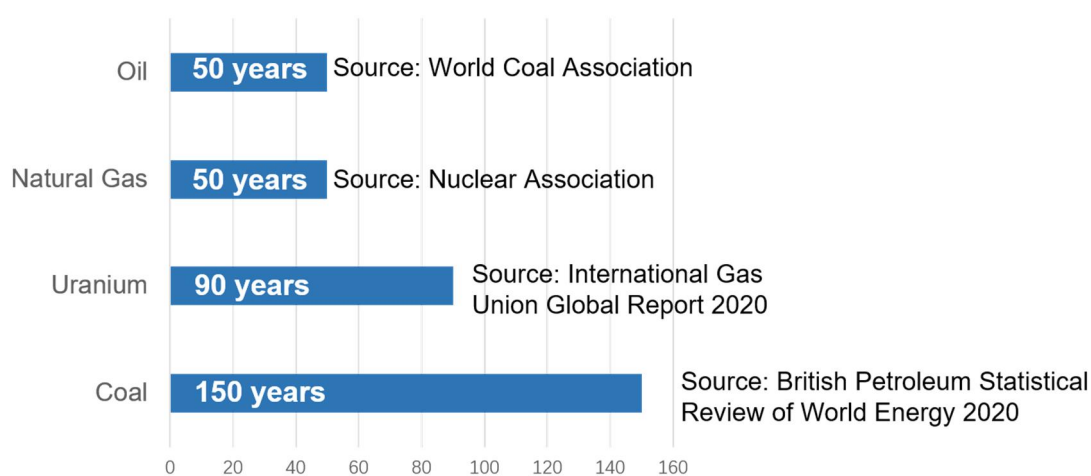


**Figure 1.1** Industry estimates of economically viable fossil fuel reserves.<sup>1</sup>

With the scientific and technological development, the growing importance of the energy demand cries for being sorted out. Nevertheless, the amount of global energy storage is dramatic decrease during several decades. The Industry estimates of economically viable fossil fuel reserves is shown in Fig.1.1. The amount of oil and natural gas only can support all humanity using in fifty years, concurrently, the uranium will be used up at 90 years and quickly running out of coal will happened in 150 years.

Energy storage devices are the most heated debate by the researchers, including fuel cell, supercapacitors, solar cell and batteries. Among these energy storage devices, due to their working mechanisms, batteries and supercapacitors are much accounted of more and more research laboratories and enterprises. The vital parameter of different energy storage devices is Power Density-Energy Density (Fig.1.2), which can illuminate their advantages and disadvantages in applications. In this section, we talk about the background, working mechanism and classification of lithium-ion batteries and supercapacitors.

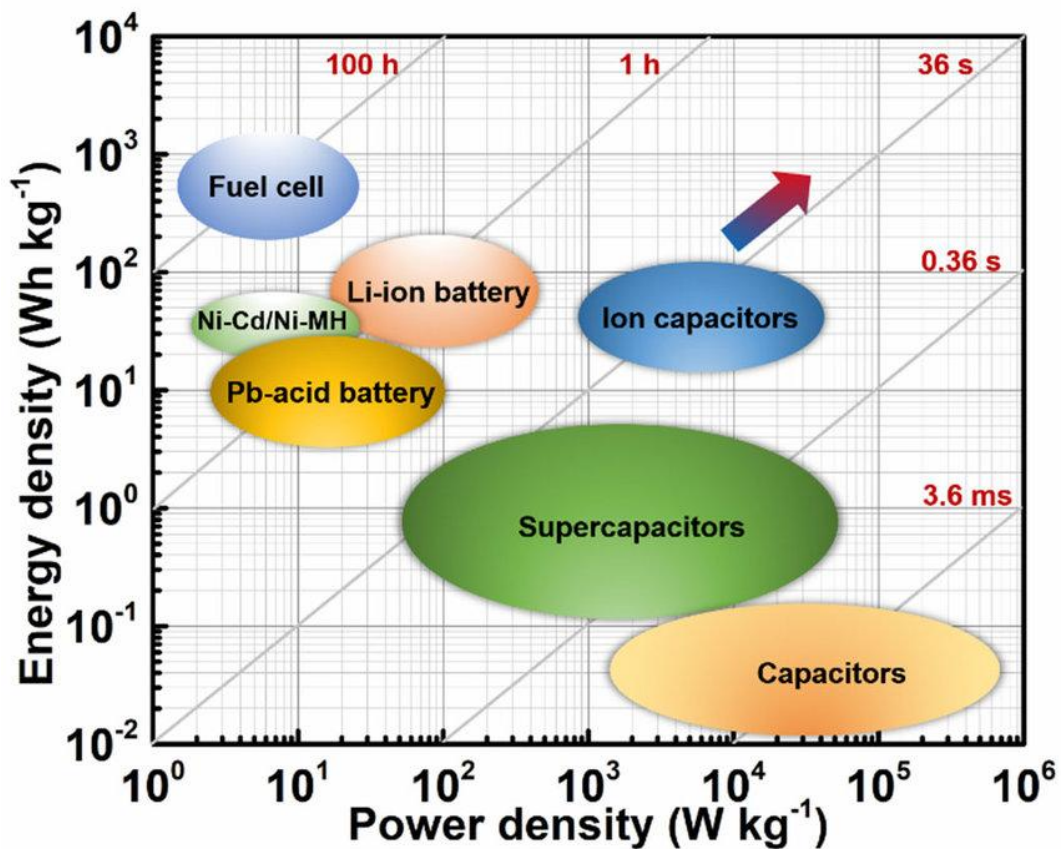


**Figure 1.2** The comparison of energy density and power density for different energy storage devices.<sup>2</sup>

**LITHIUM-ION BATTERIES (LIB)** are the choice of power source for portable electronic devices such as motor vehicle, mobile phone and energy storage power station<sup>3-5</sup>. As shown in Fig.1.2, LIB has high energy density (more than 200 Wh/kg) and low self-discharge process compared with other rechargeable systems which due to

the higher operating voltages of  $\sim 4$  V.<sup>6</sup> However, it also has several great disadvantages which limits application in high-power devices as low power density (lower than 350 W/kg) and short cycle life. Not only the parameters of energy and power, but also cost, cycle life, charge-discharge rate, safety, and environmental impact need to be considered in adopting LIBs for various applications.<sup>7-10</sup> For promoting the quality of LIB, in the first place, we need to understand its working mechanism.

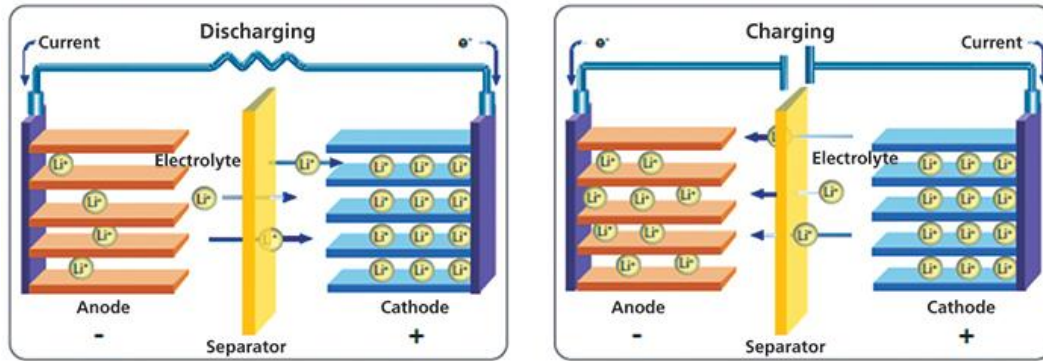


**Figure 1.3** The operation of a Li-ion battery during discharging and charging.<sup>11</sup>

From Fig.1.3, there is the operation of LIB during discharging and charge. Normally, the battery contains an anode (carbon, graphite)<sup>12,13</sup>, a cathode (lithium metal oxide)<sup>14-16</sup>, a separator (permeable membrane)<sup>17</sup>, electrolyte (a lithium-ion salt in a non-aqueous (aprotic) solvent)<sup>18,19</sup>, and current collectors (anode: Cu and cathode: Al)<sup>20</sup>. The separator has two main function that enables the Li-ions to shuttle between two electrodes and curbs a short circuiting.

Charging process is referred to intercalation. During intercalation, Li-ions will move from an ordered Li metal cathode lattice and after through separator become embedded between graphene sheets in the anode. Instead, discharging is de-intercalation process. During de-intercalation process, Li-ion migrate from anode to cathode and electrons move in an external circuit in the same direction as Li-ion.<sup>21-24</sup> During the initial charging cycle, on the surface of the anode, there will form the solid electrolyte interface (SEI) which compose of electrolyte reduction products.<sup>25</sup> The SEI film will prevent further secondary reaction and then reduce Li amount loss in LIB.<sup>26,27</sup>



As a result, the SEI film functions as a vital role to enables the LIB to operate in an efficient and reversible manner.

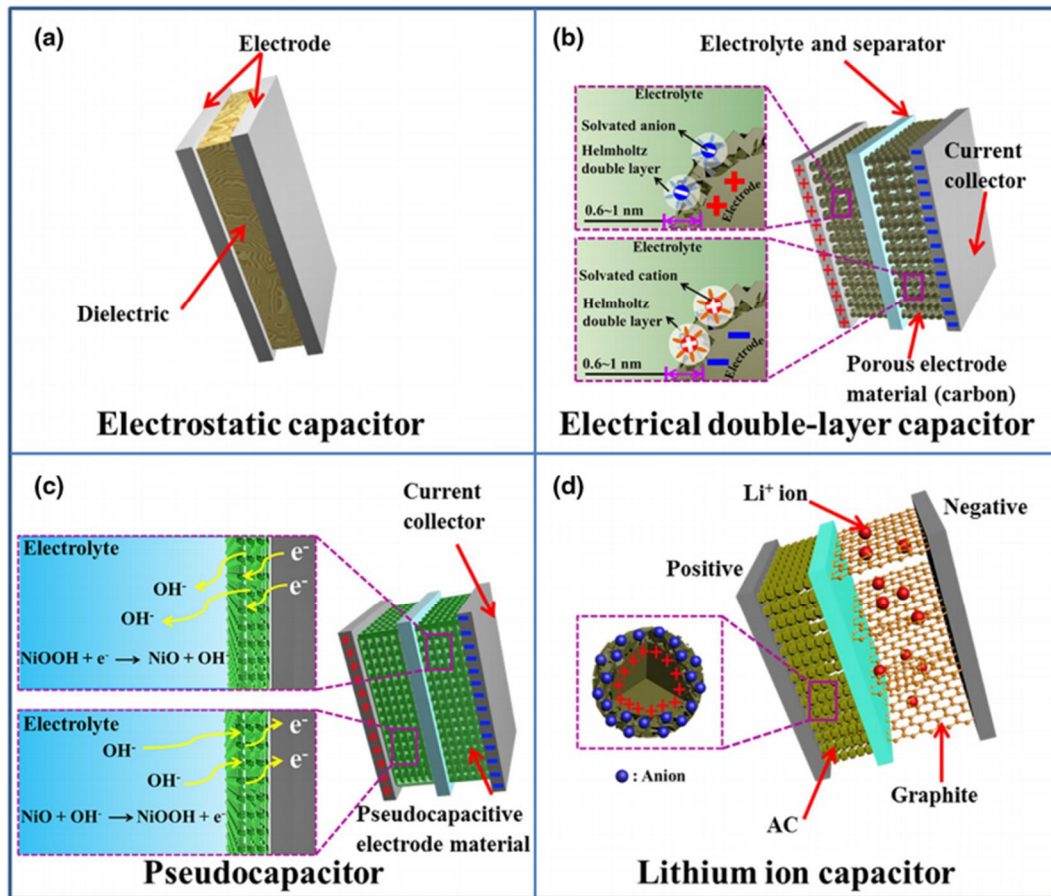


**Figure 1.4** Schematic diagrams of (a) an electrostatic capacitor, (b) an electric double-layer capacitor, (c) pseudocapacitor and (d) lithium-ion capacitor.<sup>28</sup>

**SUPERCAPACITOR (SC)** is another energy storage device including electrochemical double layer capacitor (EDLC) and pseudocapacitor. with ultra-high-power density (10 kW/kg) and excellent cycling stability (more than  $10^5$  cycles) different with LIB. That is due to their charge storage is based on the surface reactions of electrode materials without ion diffusion within the bulk of materials.<sup>29,30</sup> However, SC has low energy density of 5-20 Wh/kg (Fig.1.2) which will limit it used in long-range devices. More specifically, the energy density depends on the specific capacitance of the electrode materials and the overall cell voltage.<sup>31-33</sup> Therefore, to improve the energy density, we can choose the porous and nano-size electrode materials to condition

the specific capacitance and build hybrid/asymmetric supercapacitors to increase the overall cell voltage on account of the potential gap between the two electrodes.

Fig.1.4 has described two different charge storage mechanisms happening in SC containing EDLC and pseudocapacitor. Thereinto, EDLC stores energy by forming an electrochemical double layer at the interface of the electrodes and electrolyte which also called electrostatically storing charges. Generally, the fundamental equation for EDLC is given as followed:

$$C = (\epsilon_0 \times \epsilon_r \times A)/d \quad (1.1)$$

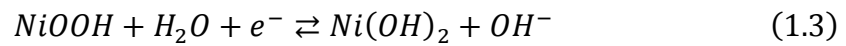
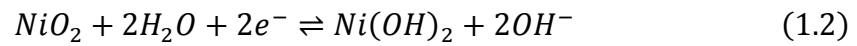
where A is the surface area (SA) of the electrodes;  $\epsilon_0$  is the permittivity of free space;  $\epsilon_r$  is the relative permittivity of the dielectric material; and d is the distance between two oppositely biased electrodes.<sup>34</sup> Considering these parameters, high-surface-area carbon-based materials usually be used into EDLC which has excellent cycling stability and without any significant changes even after several thousands of cycles. It is a pity that EDLC has inadequate specific energy. In contrary to EDLC, another kind of capacitor (pseudocapacitor) can solve this problem by the fast and reversible redox reactions of electroactive materials.<sup>35</sup> Every coin has two sides, the reversible oxidation-reduction reaction happening in pseudocapacitor causes swelling and shrinkage of the materials that will decrease the cycle performance stability.

The same with LIB, SC also have four major parts: positive, negative, electrolyte and separator.<sup>36</sup> SC can be divided into three types: hybrid SC, symmetric SC and asymmetric SC depended on configuration of two electrodes. Another way of classification is relied to electrolyte: aqueous solvent (acid or alkali) and organic solvent (proton inert solvent).<sup>37</sup>

## 1.2 Nickel based materials

In recent years, extensive studies have focused on developing potential electrode materials with high excellent electrochemical performance. Of these promising electrode materials, transition metal oxides (TMOs) and their mixtures are the most promising anode materials for energy storage devices due to their natural abundance, low cost, and their high theoretical capacity in comparison to the commercial graphite anode ( $372 \text{ mAh}\cdot\text{g}^{-1}$ ).<sup>38</sup>

Nickel oxide and Nickel hydroxide has a high theoretical capacitance (NiO:2584 F/g, Ni(OH)<sub>2</sub>: 2081 F/g), low cost and low environmental impact which is good for using as electrodes materials in LIB or SC.<sup>39-40</sup> Similarly, other nickel-based composites materials also have advantages for energy storage devices as that they can effectively prevent aggregation to improve the electrochemical performance. The charge-discharge reactions are extremely important for LIB and pseudo capacitor. Normally that of the nickel-based electrode have been expressed as followed:<sup>41</sup>



## 1.3 Quantum dots

Quantum dots (QDs) are a kind of nano size semiconductive materials with binding the excitons in three spatial directions.<sup>42-44</sup> This constraint can be attributed to the electrostatic potential, the interface between two different semiconductor materials, and the surface of the semiconductor. Because of their quantum mechanics, QDs have optical and electronic properties which are different with other bulk materials or large particles nanomaterials. Therefore, we also call QDs as 0-dimensional nano-semiconductor materials and generally spherical or quasi-spherical with diameter of 2-

20 nm.<sup>45</sup> Specific examples are silicon quantum dots, carbon(graphene) quantum dots, g-C<sub>3</sub>N<sub>4</sub> quantum dots, cadmium sulfide quantum dots, zinc selenide quantum dots, lead sulfide quantum dots, Mxene quantum dots and indium phosphide quantum dots.<sup>46-50</sup>

As microelectrode, quantum dots can be used not only as current collectors but also as electrochemical active electrodes which will enormously promote electrochemical properties due to that QDs with high electrical conductivity has uniformly dispersed on the microelectrodes and enlarged specific surface area (SSA) of microelectrodes presenting more active sites.<sup>51,52</sup> These advantages (as shown in Fig. 1.5) will contribute to using QDs composites with other conductive materials in the flexible film-based energy storage that require a fast charge/discharge rate and high-power density. This is vital for both LIBs and SCs.



**Figure 1.5** Some properties of QDs for electrochemical applications.<sup>53</sup>

For overcoming the disadvantage of a long diffusion length of Li<sup>+</sup> in LIBs, it is an effective way to decreasing the size of anode materials to QD scale.<sup>54</sup> However, decreasing the size blindly is not suitable for LIBs, because the larger SSA appeared the larger exposed surfaces to form the SEI. For another energy storage device SCs, the energy density is the key for development. QDs have been investigated as electrode materials or mixture materials in SCs because of their large quantity of accessible active

sites, good conductivity, and short diffusion length which will increase the energy density directly.

#### **1.4 The objectives of thesis**

In this thesis, nickel-based materials composited with different quantum dots (graphene, g-C<sub>3</sub>N<sub>4</sub> and Mxene) are studied for lithium-ion battery and supercapacitor. The main objectives of thesis are listed below:

I. Preparation of hierarchical nanostructured NiO (h-NiO) microtubes by a simple wet-chemical synthesis and investigation the application in lithium-ion batteries with high cycle capacity (770 mAh·g<sup>-1</sup>) and extremely high columbic efficiency (98.8%).

II. Preparation of graphene quantum dots (GQDs)/Ni(OH)<sub>2</sub> composites on carbon cloth (G-NH//CC) by hydrothermal method and its application in supercapacitor exhibiting a high energy density of 80.8 Wh·kg<sup>-1</sup> at a power density of 2021 W·kg<sup>-1</sup>.

III. Preparation of boron doped g-C<sub>3</sub>N<sub>4</sub> quantum dots (B-CNQDs) coating on Ni(OH)<sub>2</sub> nanoflowers (B-CNQD<sub>x</sub>-Ni) with p-n heterojunction which as symmetric supercapacitor electrode materials with high specific capacitance (1700 F·g<sup>-1</sup> at 1.5 A·g<sup>-1</sup>).

IV. Preparation of Mxene quantum dots (MQDs) by Microwave assistant dispersion with different solvent (DMSO, DMF, EtOH) compositing with Ni(OH)<sub>2</sub> on Ni foam (M-NH//NF) as symmetric supercapacitor.

#### **1.5 The organization of thesis**

In this thesis, chapter 1 briefly discussed about the background of energy storage devices (lithium-ion battery, supercapacitor ) and their classification, working

mechanism. Also, the normal information of quantum dots and nickel-based materials involving structures and application in energy storage devices.

Chapter 2 introduces the latest literatures of nickel-based and quantum dots used in lithium-ion batteries or supercapacitors. The structure and advantages of these materials of electrodes are thoroughly analyzed.

Chapter 3 focuses on the methodology, including sample preparation and characterization. Firstly, the methods of synthesizing samples are described. Subsequently, general characterization techniques, including, X-ray photoelectron spectroscopy (XPS), photoluminescence (PL), electron scanning microscopy (SEM), transmission scanning microscopy (TEM). Finally, the detail to electrochemical tests and formulate for the calculation of specific capacitance, specific energy and specific power are given.

Chapter 4 discussed about the result to synthesis of hierarchical nanostructured NiO (h-NiO) microtubes by a simple wet-chemical synthesis and investigation the application in lithium-ion batteries

Chapter 5 studies how to prepare graphene quantum dots (GQDs)/Ni(OH)<sub>2</sub> composites on carbon cloth (G-NH//CC) by hydrothermal method. Then, the structure and electrochemical performance of this composite are investigated.

Chapter 6 introduces the characterization and electrochemical properties of boron doped g-C<sub>3</sub>N<sub>4</sub> quantum dots (B-CNQDs) coating on Ni(OH)<sub>2</sub> nanoflowers (B-CNQDx-Ni). And also introduces the mechanism that p-n heterojunction has increase the performance of electrochemical.

Chapter 7 develops the Mxene quantum dots (MQDs) by microwave assistant dispersion with different solvent (DMSO, DMF, EtOH) compositing with Ni(OH)<sub>2</sub> on Ni foam (M-NH//NF) as symmetric supercapacitor. The main electrochemical performance is also provided.

Chapter 8 has summarized the novel and existent issue in the research. In addition, recommendations for future work are also noticed.

## **Chapter 2: Literature Review**

### **2.1 Introduction**

For improving the electrochemical properties of LIBs and SCs, the researchers investigated many kinds of composites materials as electrodes. These materials increasing the cycling stability and capacitances of energy storage devices by promoting the contact area with electrolyte, electrons transport pathway and well physical or chemical structure stability. Graphite is normally used as anode materials in commerce because of its low production cost and relatively stable electrochemical performance. However, there are still disadvantages for electrochemical: 1, The specific capacity is insufficient to meet the actual needs of power batteries. 2, The rate performance is poor, and high current charging and discharging cannot be carried out which will damage devices. 3, The charging and discharging voltage is too low.

To solve these issues, researchers published wide range of composites materials mixing graphite and TMO (TMHO, Quantum dots, doped materials). In this chapter, we will talk about the literature review of nickel base materials and quantum dots in detail and explain why they have better electrochemical performance for LIBs and SCs.

### **2.2 Nickel-based materials for lithium-ion batteries and supercapacitors**

Nickel-based materials are frequent materials used as anode in energy storage device, due to their excellent capacity and low cost. The common nickel-based materials are pristine nickel oxide/hydroxide, nickel oxide/hydroxide with incorporated or decorated carbonaceous materials, nickel-based bimetallic materials, nickel-containing metal–organic frameworks (MOF), nickel-sulfide-based materials, nickel-phosphide-based materials, and multi-component nickel-containing materials.

#### **(1) Pristine nickel oxide/hydroxide**



Pristine nickel oxide/hydroxide is the Easiest prepared materials among nickel-based electrodes. In addition, they have facile synthesis and favorable chemical stability that will foster the spread use. As early as 1997, Prof. Srinivasan<sup>55</sup> has reported porous nickel oxide as an electrochemical capacitor with a specific capacitance of 59 F/g. Simultaneously, in the nearest, prof. Lokhande's group<sup>56</sup> has reported the growth of nanobelts-like Ni(OH)<sub>2</sub> on the Ni foam with 50.29 mAh/g at 100 mV/s of specific capacitance and 96% capacitance retention after 2000 cycles. And in 2005, G.H. Yue<sup>57</sup> has reported a kind of flower-like nickel oxide nanocomposites anode materials used in lithium-ion batteries with reversible discharge capacities of 846 mAh/g. Not only flower-like, but also other morphologies of NiO have been developed as nanorods, nanofibers, nano-walls and so on. Yong Wang and Yuqin Zou<sup>58</sup> have published the manuscript about a self-assembled porous NiO nanorod under microwave assistant which has 1566 mAh/g of corresponding charge capacities. Xuelin Yang's group<sup>59</sup> have reported a novel material nickel oxide nano-walls on Ni foam with initial discharge and charge capacity of 1029 and 761 mAh/g at 0.15C.

However, the capacitances value is still relatively low for commercial application that leads to many groups study different semiconductive materials composites with nickel oxide/hydroxide.

## **(2) Carbonaceous materials**

One of composite material with nickel oxide/hydroxide is carbonaceous material, content graphite (graphene, rGO), carbon aerogels, carbon nanofibers/clothes (CNT), and carbon quantum dots. The benefits brought by carbonaceous materials is shown in Fig.2.1.

Prof. Ma with her group<sup>60</sup> has synthesized mesoporous nickel oxide/reduced graphene oxide composite by a facile hydrothermal method, which has 94.9% capacitance retention even after 5000 cycles. Gui et al<sup>61</sup> directly synthesized NiO/graphene aerogels by a simple solvothermal route. The nickel oxide was deposited

into the highly porous GA by electrostatic coating to form NiO/GA composites. Graphene aerogels provided high surface area between NiO and electrolyte, and obviously enhanced electronic transmission pathway. Carbon clothes is another available material for increasing the property of the nickel-based nanocomposites. Jing Zhang<sup>62</sup> has reported a novel flexible electrode material which composite carbon nanotubes with carbon fiber paper and NiO. This material has high specific capacitance of 1317 F/g at a current density of 1.2 A/g for flexible binder-free supercapacitor. Carbon clothes is not only skeleton for entire material increasing the mechanical property but also flexible for wearable devices.



**Figure 2.1** Advantages of using carbonaceous materials.<sup>28</sup>

### **(3) Nickel-based bimetallic materials**

Bimetallic materials not only have various excellent properties of nanomaterials, but also have better electrochemical performance than a single metal due to the unique synergistic effect between metals, so they can be well applied to energy storage devices. Commonly used nickel based bimetallic materials are Ni-Fe, Ni-Co, Ni-Cu and Ni-Mo. Ni-Co binary hydroxide system<sup>63</sup> is the most studied elements due to their abundance and high capacitance of 1030 F/g at mass loading of 1 mg/cm<sup>2</sup> at a current density of 3 A/g. Prof. Shen's group<sup>64</sup> has developed f-Ni/Fe cells with high energy/power densities

(100.7 Wh/kg at 287 W/kg) which also is binder-free, bendable, and durable in long-term cycling.

#### (4) nickel-containing metal–organic frameworks (MOF)

Metal organic frameworks (MOF) are organic-inorganic hybrid materials with intramolecular pores formed by self-assembly of organic ligands and metal ions or clusters through coordination bonds.<sup>65</sup> MOF have abundant pores, high specific surface area (SSA), controllable topology & morphology and multifunctionalities that is suitable for electronics transmission to enhance the electrochemical properties. Several groups have synthesized nickel-based MOFs as energy storage device electrode materials. Table 2.1 as shown in followed is nickel-base materials with different morphology and their electrochemical performance.

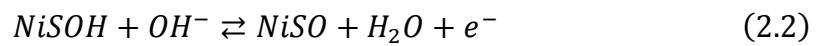
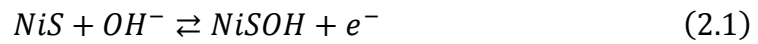
**Table 2.1** Nickel-base materials with different morphology and their electrochemical performance.

Materials	Electrolyte	Cs	Cycling stability	ref
Ni/Co-MOF	3M KOH	1067F/g (1A/g)	68.4% (2500 cycles)	66
Ni-MOF	3M KOH	1057F/g (1A/g)	70% (2500 cycles)	67
Ni-BPDC/CNF	6M KOH	250.6 mAh/g	92% (5000 cycles)	68
Flower like Ni-MOF	6M KOH	920F/g (1A/g)	75% (3000 cycles)	69
Ni-BPDC/GO	6M KOH	630 F/g (1A/g)	82.4% (1400 cycles)	70
Co/Ni-MOF	1M KOH	148 F/g (2A/g)	/	71
Ni <sub>2.6</sub> Cu <sub>0.4</sub> MOFs	2M KOH	1282 F/g (1A/g)	85.7% (2000 cycles)	72
PPy–CPO-27-Ni	1M KCl	354 F/g (1A/g)	70% (2500 cycles)	73

#### (5) nickel-nonmetal-based materials

Another class of nickel-based materials is nickel composited with nonmetal (Sulfide, phosphide). These materials have high theoretical capacitance and intrinsic conductivity which also improves the charge transfer kinetics as the electrode

materials.<sup>28</sup> Wang et al<sup>74</sup> have reported nickel sulfide/graphene oxide nanocomposite by a gentle solvothermal method. The charge translocation mechanism of the NiS have been expressed as followed:



The capacity achieved was 800 F/g at current density of 1 A/g as a promising material for the development of high-performance supercapacitors. Furthermore, it has excellent cycling performance under 1A/g even after 1000 cycles. There are also articles talked about the Ni<sub>x</sub>P<sub>y</sub> as conductor materials. Prof. Jun and his group<sup>75</sup> have synthesized the honeycomb like 3D self-supported nickel phosphide hetero nanoparticles applied in high performance supercapacitors. Ni<sub>x</sub>P<sub>y</sub>//AC not only has high specific capacitance of 1272 C/g at 2 A/g, extremely great cycle stability after 5000 cycles (90.9%), but also has 67.2 Wh/kg at a power density of 0.75 kW/kg.

### 2.3 Quantum dots for lithium-ion batteries and supercapacitors

Quantum dots (QDs) have novel electronic and optical properties that can be used in many important fields, such as electronics, optoelectronics, photovoltaics, and biomedicine. As 0D material exhibiting quantum confinement effects, QDs can fully contact the electrolyte, and provide a shorter ion diffusion distance which are easier to combine with other materials when used in energy storage devices.<sup>76</sup> It is particularly important to prepare fixed-size quantum dots that will affect the surface activity and conductivity. In addition, high specific surface area is often accompanied by high reactivity, which reduces the chemical stability of quantum dots. So QDs still have many bottlenecks.

### 2.3.1 Graphene Quantum dots

Graphene Quantum dots (GQDs) can increase the mechanical strength, elasticity, thermal stability, and electrical conductivity that is suitable for mixing in capacitor materials.<sup>77</sup> First of all, different sizes of GQDs can be classified by filtration method, and effects of size on structural is shown in fig.2.2.

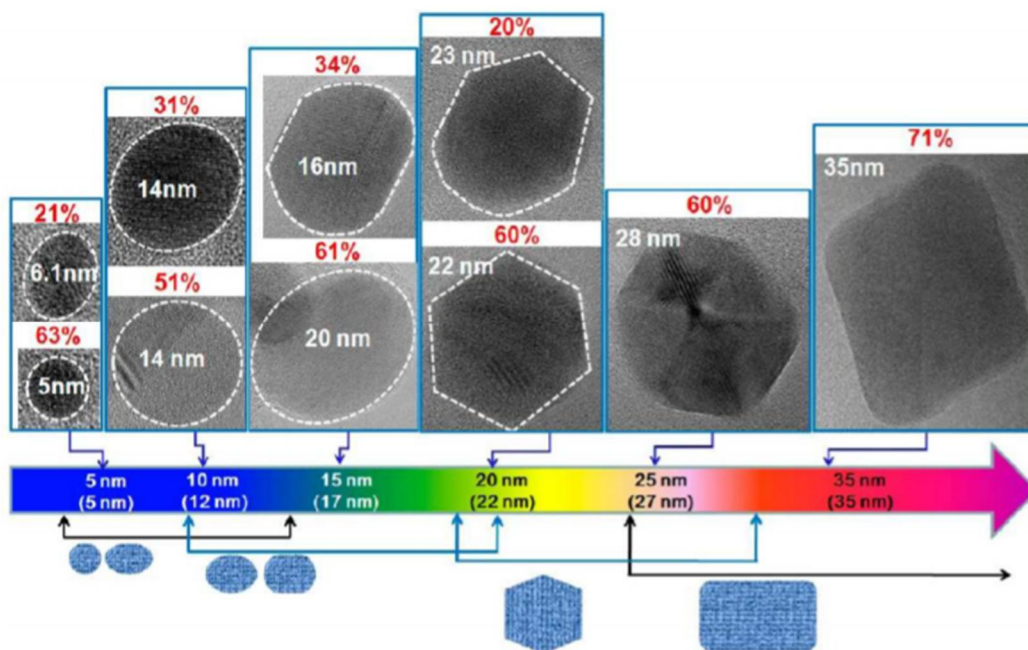


**Figure 2.2** HRTEM image and PL spectra of GQDs according to their diameters.<sup>78</sup>

In 2014, Zhang et al<sup>79</sup> have composited graphene quantum dots with 3D graphene by the electrochemical method. Owing to their desirable advantages of high electron mobility and tunable bandgaps, they have outstanding electrochemical performance of 268 F/g at 1.25 A/g higher than the bare 3D graphene (136 F/g). However, the article has not report transparent and flexible properties of GQDs. Prof. Lee<sup>80</sup> have synthesized ipG-GQDs as the flexible electrode with high stability even under bending angle 45° with 10000 cycles.

### 2.3.2 g-C<sub>3</sub>N<sub>4</sub> quantum dots (CNQDs)

The same as graphene, g-C<sub>3</sub>N<sub>4</sub> also is a typical 2D conjugated polymer material with excellent electronic energy band structure, electron-rich properties, surface functionalized modification, high physical and chemical stability, non-toxic and abundant raw materials.<sup>81</sup> Therefore, it is significant to cut the 2D g-C<sub>3</sub>N<sub>4</sub> into 0D used as electrode materials. Many groups have published the manuscripts about synthesize uniform CNQDs. 0D g-C<sub>3</sub>N<sub>4</sub> were successfully prepared from bulk g-C<sub>3</sub>N<sub>4</sub> directly by a thermal-chemical etching process.<sup>82</sup> Later, Prof. Yang has synthesized by the standard pyrolysis method using urea as the precursor.<sup>83</sup> Unfortunately, there are fewer reports about CNQDs use for the energy storage devices.

### 2.3.3 Mxene quantum dots (MQDs)

Mxene is a kind of novel nanosheet materials with M<sub>n+1</sub>X<sub>n</sub>T<sub>x</sub> structure where M is transition metals, X is carbon or nitride and T is surface group (OH<sup>-</sup>, F<sup>-</sup>, O<sup>2-</sup> etc.).<sup>84</sup> MXene has excellent electrical properties and is a promising electrode material for energy storage. Mxene quantum dots are generally directly crushed by Mxene materials through hydrothermal or some physical methods to form nanoparticles. As early as 2017, Zhi et al<sup>85</sup> have prepared MQDs by hydrothermal method with different temperature (100 °C, 120 °C, 150 °C) as multicolor cellular imaging reagents. TEM and AFM images of MQDs have illuminated that particle sizes are 2.9, 3.7, and 6.2 nm with thickness of 0.99, 0.91, and 0.89 nm. Later, Yan Li's group<sup>86</sup> has synthesized chlorine and nitrogen co-doped Ti<sub>3</sub>C<sub>2</sub> MXene quantum dots (Cl, N-Ti<sub>3</sub>C<sub>2</sub> MQDs) by the efficient electrochemical method.

## 2.4 Summary

For improving the electrochemical properties of LIBs and SCs, many groups have investigated many kinds of composites materials as electrode to increasing the cycling

stability and capacitances of energy storage devices. Nickel based materials have great intrinsic theoretical capacity and friendly for environment which is suitable for using in energy storage devices. In addition, nickel-based materials normally as a p-type semiconductor with high theoretical capacitance, and quantum dots as n-type semiconductor. When they composited, p-n heterojunction will be produced between the material interfaces. When different type of semiconductor contacts with together, the side of p type semiconductor loses of electron holes and leaves anions, and the side of n type leaves cations. It produces the paper-thin and high conductive space-charge region at the interfaces of semiconductors. This will improve electrochemical performance for LIBs or SCs.

## Chapter 3: Experimental Section

### 3.1 Materials

Nickel chloride hexahydrate ( $\text{NiCl}_2 \cdot 6\text{H}_2\text{O}$ ), ethylene glycol (EG,  $(\text{CH}_2\text{OH})_2$ ), sodium acetate ( $\text{CH}_3\text{COONa}$ ), nickel nitrate hexahydrate ( $\text{Ni}(\text{NO}_3)_2 \cdot 6\text{H}_2\text{O}$ ), urea ( $\text{CH}_4\text{N}_2\text{O}$ ) and citric acid ( $\text{C}_6\text{H}_8\text{O}_7$ ) were purchased from Sigma-Aldrich LLC. Carbon clothes HCP330 with density of  $160 \text{ g} \cdot \text{cm}^{-2}$  and thickness of  $320 \mu\text{m}$  was from WizMAC (Daejeon, South Korea). Melamine ( $\text{C}_3\text{H}_6\text{N}_6$ ), boric acid ( $\text{H}_3\text{BO}_3$ ), Potassium hydroxide (KOH), N,N-Dimethylformamide (DMF,  $\text{C}_3\text{H}_7\text{NO}$ ) and Dimethyl sulfoxide (DMSO,  $\text{C}_2\text{H}_6\text{OS}$ ) were purchased from Shanghai Macklin Biochemical Co., Ltd. Mxene ( $\text{Ti}_3\text{C}_2$ ) was purchased from Nanjing mission new material technology Co. Ltd. Nickel foam with density of  $350 \text{ g} \cdot \text{cm}^{-2}$  and thickness of  $0.5 \text{ mm}$  was from Kunshan Guangjiayuan New Materials Co., Ltd. The electrochemical materials containing poly(1,1-difluoroethylene) (PVDF,  $-(\text{C}_2\text{H}_2\text{F}_2)_n-$ ), N-Methyl pyrrolidone (NMP,  $\text{C}_5\text{H}_9\text{NO}$ ), Super-P Carbon black and polyvinyl alcohol (PVA,  $-(\text{C}_2\text{H}_4\text{O})_n-$ ) were purchased from Aladdin reagent (Shanghai) Co., Ltd. All chemical reagents were analytical grade without further purification.

### 3.2 Synthesis of composites

#### 3.2.1 Hierarchical nanostructured NiO (h-NiO) microtubes

Firstly, we synthesized  $\text{Ni}(\text{OH})_2$  precursor,  $0.56 \text{ g}$  of nickel chloride hexahydrate ( $\text{NiCl}_2 \cdot 6\text{H}_2\text{O}$ ) was dissolved in  $20 \text{ mL}$  of ethylene glycol (EG). Secondly,  $1.4 \text{ g}$  of sodium acetate was added into the above mixture solution under magnetic stirring at  $60^\circ\text{C}$  for  $30 \text{ min}$ . Then, the mixture solution was heated at  $170^\circ\text{C}$  for  $3 \text{ h}$ , as later, cooled to room temperature. The resulting precipitate was collected and washed with ethylene glycol and ethanol three times. Finally, the light green powder was dried overnight in a



vacuum oven at 60 °C. The prepared Ni(OH)<sub>2</sub> precursor was then calcinated in a furnace at 350 °C for 1 h under nitrogen atmosphere so as to obtain black h-NiO powder.

### **3.2.2 Graphene quantum dots (GQDs)/Ni(OH)<sub>2</sub> composites on carbon cloth (G-NH//CC)**

GQDs were synthesized as followed. Citric acid solution (50 mL, 1 mg/mL) was transferred into a Teflon-lined autoclave and heated in an oven at 200 °C for 4h. Then, the obtained solution was then dialyzed using dialysis tubing (3000 Da, Spectrum Lab. Inc) against DI water for 1 day to remove impurities, resulting in the GQDs solution (2 mg/mL).

Prior to the hydrothermal process, the CC (HCP330, WizMAC, 160 g/cm<sup>2</sup>, 320 μm-thick) was cleaned with acetone and DI water under ultrasonication for 10 min, followed by UV/ozone treatment for 4 h. Typically, the UV/ozone treated CC was immersed in a reaction solution (50 mL) containing Ni(NO<sub>3</sub>)<sub>2</sub>·6H<sub>2</sub>O (5 mmol), urea (10 mmol), and the prepared GQDs. The reaction solution was stirred at 60 °C for 2 h and then transferred into a Teflon-lined autoclave and kept in an oven at 120 °C for 24 h. After the hydrothermal reaction, the autoclave was allowed to cool down to room temperature, and the obtained samples were washed several times in DI water and ethanol. The samples were denoted as G10-NH//CC, meaning that 10 mg of GQDs was added in the reaction solution. For comparison, Ni(OH)<sub>2</sub> was also synthesized on CC without GQDs (denoted as NH//CC).

### **3.2.3 Boron doped g-C<sub>3</sub>N<sub>4</sub> quantum dots (B-CNQDs) coating on Ni(OH)<sub>2</sub> nanoflowers (B-CNQDx-Ni)**

1.5 g melamine, 1.5 g urea and 0.125 g boric acid were dissolved into 50 mL DI-water with sonication for 10 min. Then the mixture was dried in an oven at 80 °C until powder formed. The powder was further transferred into an alumina crucible for calcination (550 °C, 4 h, N<sub>2</sub>, 2.5 L/min). After cooling to room temperature, the yellow

powder was milled and named as B-C<sub>3</sub>N<sub>4</sub>. 60 mg B-C<sub>3</sub>N<sub>4</sub> was put into 60 mL ethanol, and then 2 mL KOH (2 M) was added. After sonicating for 30 min, the mixed solution was moved into a 90 mL autoclave and kept at 180 °C for 16 h to obtain B-CNQDs. Then, 1000 D dialysis bag with DI-water was used to remove KOH and EtOH. The collected B-CNQDs (yield ≈45%) was dispersed in EtOH (1 mg/mL) and stored in the refrigerator (4 °C). As contrast, pure g-C<sub>3</sub>N<sub>4</sub> quantum dots (CNQDs) was synthesized by the same method, but without boric acid at initial.

1.5 g Ni(NO<sub>3</sub>)<sub>2</sub>·6H<sub>2</sub>O and 1 g urea were dissolved into 60 mL ethanol with stirring for 30 min at room temperature. Then, the solution was moved into 90 mL autoclave and heated at 120 °C for 4 h. After cooling down, the product was washed by ethanol and DI water for three times followed by drying in an oven for whole night at 60 °C.

We used impregnation method to build composite B-CNQDs with Ni(OH)<sub>2</sub>. Different volume (0.5 mL, 1 mL, 1.5 mL) of B-CNQDs solution (1 mg/mL) was dropped by pipette into 100 mg as-prepared Ni(OH)<sub>2</sub> and impregnated for 2 h. Then the composites were washed by DI water for several times which followed by drying at 60 °C. We named the samples as B-CNQD5-Ni, B-CNQD10-Ni and B-CNQD15-Ni, according to the amount of B-CNQDs.

### **3.2.4 Mxene quantum dots (MQDs) compositing with Ni(OH)<sub>2</sub> on Ni foam (M-NH/NF)**

We used microwave assistant sonication to prepare Mxene quantum dots (MQDs). Firstly, 0.5 g Mxene (Ti<sub>3</sub>C<sub>2</sub>) was dissolved into 60 mL organic solvent (EtOH, DMF and DMSO) with magnetic stirring for 30 min at room temperature. Subsequently, the mixture solution was transmitted into 250 mL three-necked quartz round bottom flask, and sonication with microwave assistant at 80 °C for 1 h. After cooling down, the mixture solution was centrifugated at 1500 rpm for 10 min to remove the large scale Mxene particles. Then, the solution was removed into 90 mL autoclave with Teflon-liner in an N<sub>2</sub> atmosphere and kept in oven at 120 °C for 6 h. When being room temperature, the

solution was centrifugated again at 5000 rpm for 10 min. The MQDs could be obtained by filtering the mixture solution by 0.22  $\mu\text{m}$  membrane, followed by adjusted concentration as 2 mg/mL and name as e-MQDs, f-MQDs and o-MQDs.

Prior to the hydrothermal process, the 2 cm x 5 cm nickel foam was cleaned with acetone and DI water under ultrasonication for 10 min. Typically, the nickel foam was immersed in a reaction solution (60 mL) containing  $\text{Ni}(\text{NO}_3)_2 \cdot 6\text{H}_2\text{O}$  (0.75 g), urea (0.5 g), and the prepared MQDs. The reaction solution was stirred at 60  $^\circ\text{C}$  for 30 min and then transferred into a Teflon-lined autoclave and kept in an oven at 120  $^\circ\text{C}$  for 18 h. After the hydrothermal reaction, the autoclave was allowed to cool down to room temperature, and the obtained samples were washed several times in DI water and ethanol. The samples were denoted as x-M-NH//NF by different solution as EtOH, DMF and DMSO (e- M-NH//NF, f- M-NH//NF and o- M-NH//NF). For comparison,  $\text{Ni}(\text{OH})_2$  was also synthesized on NF without MQDs (denoted as NH//NF).

### 3.3 Characterizations

To understand the morphologies and structural details of the prepared samples, as well to unravel the roles of CNT structures in the electrochemical performance of composites, following measurements have been conducted.

#### 3.3.1 X-ray photoelectron spectroscopy (XPS)

X-ray photoelectron spectroscopy (XPS) is a technique for analyzing the chemical properties of the surface of a substance.<sup>87</sup> We can use XPS to measure the elementary composition of materials, chemical state of element and electronic state.<sup>88,89</sup> A beam of X-rays excites the solid surface for measuring the kinetic energy of electrons emitted within 1-10nm from the surface of the material as a result to obtain the XPS spectrum.<sup>90</sup> Moreover, the energy and intensity of the photoelectron peaks can be used for qualitative and quantitative analysis of all surface elements (except hydrogen).

According to the increasing of high-properties materials needs, surface modification becomes more and more important. For solving many problems related to modern materials, we need to understand the physical and chemical interactions at the surface and interface of the material layer. Surface chemistry properties will affect many aspects of the material, such as corrosion rate, catalytic activity, adhesion, surface wettability, contact barrier and failure mechanism.

The surface of materials is the position where the material interacts with the external environment and other materials. Therefore, in many applications, for changing or improving material properties and characteristics, surface modification seems particularly important. After materials treating such as faulting, slicing and scraping, XPS can be used to analyze its chemical properties and become the standard tool for surface material characterization.<sup>91</sup>

The principles of XPS are as follow two formulas:

$$E_{\text{binding}} = E_{\text{photon}} - (E_{\text{kinetic}} + \phi) \quad (3.1)$$

$$E_{\text{photon}} = h\nu \quad (3.2)$$

Where  $E_{\text{binding}}$  is the binding energy (BE) of electron,  $E_{\text{photon}}$  is the energy of the X-ray photons being used,  $E_{\text{kinetic}}$  is the kinetic energy of the electron as measured by the instrument and  $\phi$  is the work function of the spectrometer (not the material).<sup>92</sup> According to these formulas, we can get different materials electron with different value of BE. The schematic of XPS is as followed Fig.3.1.

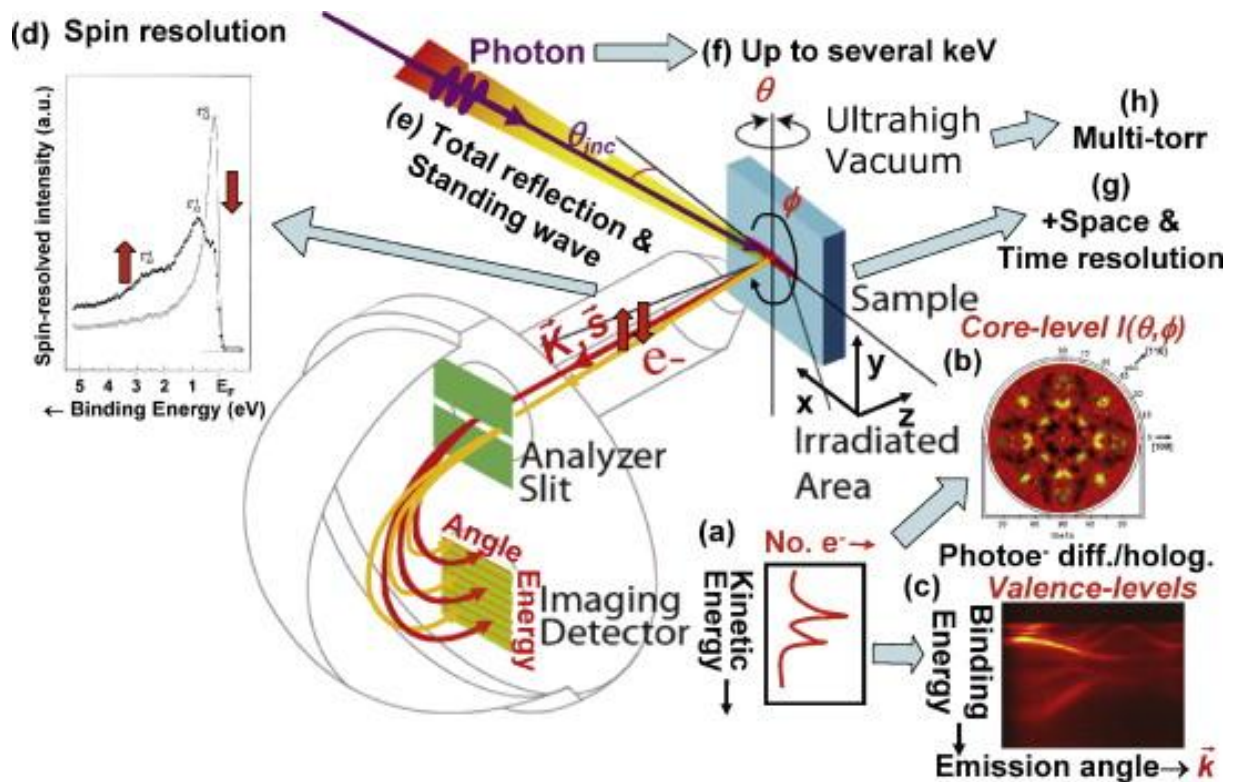


**Figure 3.1** The schematic of X-ray photoelectron spectroscopy.<sup>93</sup>

### 3.3.2 X-ray diffraction (XRD)

X-ray diffraction technology (XRD) is a research method that obtains information such as composition of the material, structure or morphology of the atoms or molecules inside the material by X-ray diffraction of a material and analyzing its diffraction pattern.<sup>94</sup> As a result, XRD is the main method to study the phase and crystal structure of substances. When a substance (crystalline or amorphous) is subjected to diffraction analysis, it will be irradiated by X-rays to produce different degrees of diffraction phenomena.<sup>95</sup> So that, the composition, crystal form, intramolecular bonding method, molecular configuration and conformation will determine its production of the substance unique diffraction pattern.<sup>96</sup> The XRD method has the advantages of no damage to the sample, no pollution, quickness, high measurement accuracy, and a large amount of information about crystal integrity. Therefore, as a modern scientific method of material structure and composition analysis, XRD has gradually been widely used in the research and production of various disciplines.

Normally, we can calculate the grain size and interplanar crystal spacing ( $d$ ) by the Scherrer equation and the Bragg's law. Bragg's law was used to explain the interference pattern of X-rays scattered by crystals which using diffraction to study the structure with any beam.<sup>97,98</sup> The Bragg's law is as following equation.

$$n\lambda = 2d \sin \theta \quad (3.3)$$

Where  $n = 1$  means first order diffraction,  $\lambda$  is incident wavelength ( $\text{Cu}_{\text{ka}} = 0.154 \text{ nm}$ ),  $\theta$  is diffraction angle and  $d$  is the interplanar crystal spacing. The explanation of Bragg's law in detail is shown in Fig.3.2.

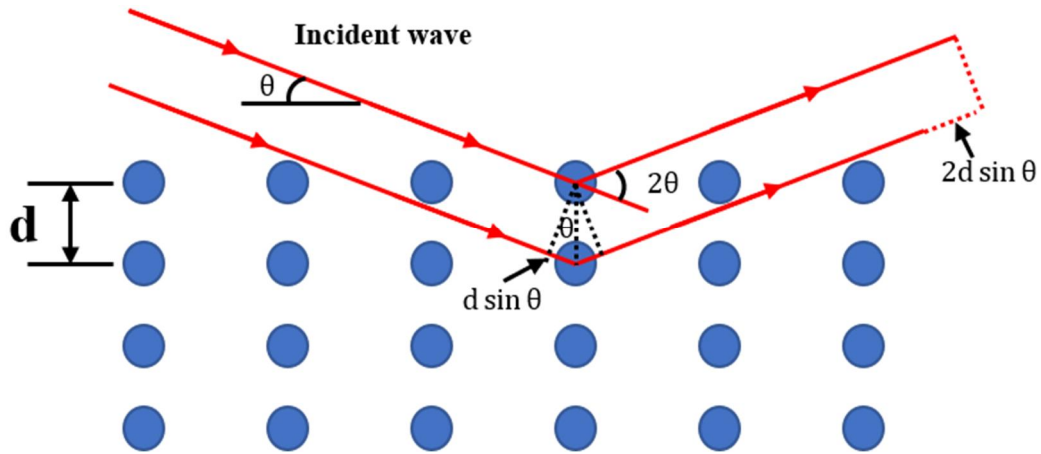


**Figure 3.2** The explanation of Bragg's law in detail.

The Scherrer equation is usually used to investigate the particle or grain size of crystal by peak position, width and intensity. The equation is shown as followed.

$$D = \frac{K\lambda}{\beta \cos \theta} \quad (3.4)$$

Where  $K$  is a constant (often taken as 1),  $\lambda$  is incident wavelength ( $\text{Cu}_{\text{ka}} = 0.154 \text{ nm}$ ),  $\theta$  is diffraction angle and  $D$  is a measure for the dimension of the particle in the direction perpendicular to the reflection plane.<sup>99</sup>

### 3.3.3 Fourier-transform Infrared Spectroscopy (FT-IR)

Fourier transform infrared spectroscopy (FTIR) is a measurement which is used to obtain infrared spectrum of absorption, emission, and photoconductivity of solid, liquid, and gas.<sup>100</sup> FTIR spectrum is recorded from 4000 to 400  $\text{cm}^{-1}$ .<sup>101</sup> The schematic of FTIR is as followed Fig.3.3.

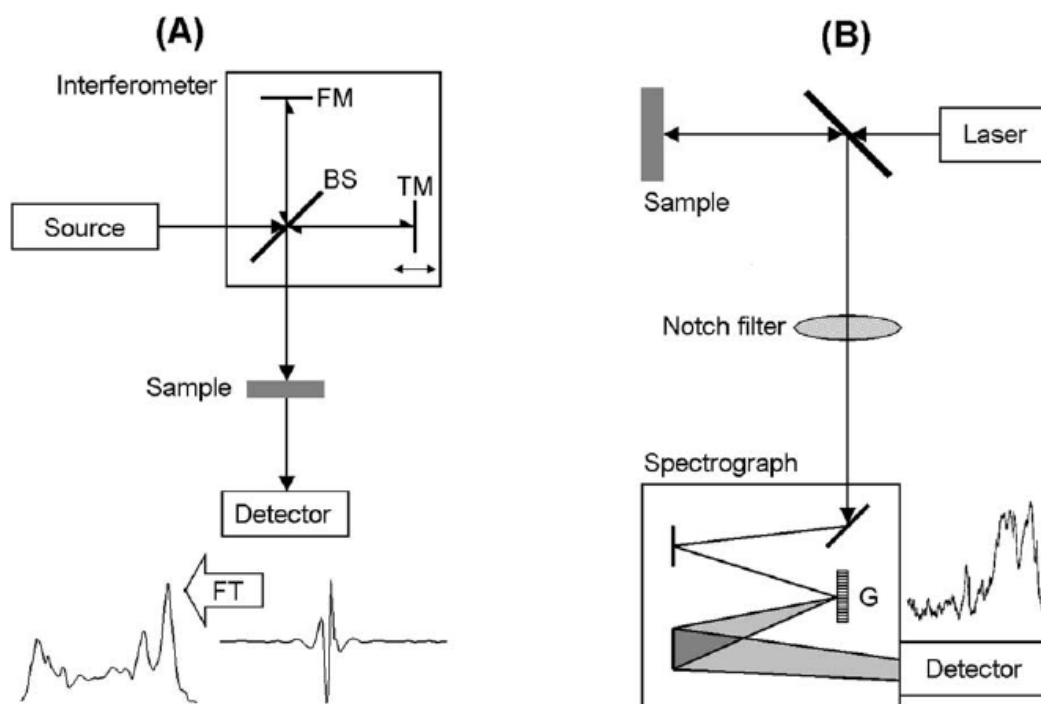


**Figure 3.3** A schematic of an interferometer used in a Fourier Transfer Infrared Spectrometer (FTIR).<sup>102</sup>

FT-IR is mainly composed of infrared light source, beam splitter, interferometer, sample cell, detector, computer data processing system, recording system, which is a typical representative of interferometric infrared. Different from the working mechanism of the dispersive infrared instrument, it does not have a monochromator and a slit and uses a Michelson interferometer to obtain the interferogram of the incident light, and then transforms the time-domain function interferogram into a frequency-domain function through fourier mathematical transformation. Table 3.1 shows FTIR frequency range and functional groups.

**Table 3.1** FTIR frequency range and functional groups.<sup>103</sup>

No.	Frequency range (cm <sup>-1</sup> )	Functional group
1	3854	O-H stretching vibration
2	3373-3422	Bonded N-H/C-H/O-H
3	2818.2-2954	C-H
4	2500-3300	Carboxyl acid
5	2138.1-2322.8	C-N
6	1415-1421	C-O/C-H bending
7	1036-1382	C-O
8	1026	Vibration of C-O in alcohol hydroxyl group

### 3.3.4 Scanning Electron Microscope (SEM) and Transmission Electron Microscope (TEM)

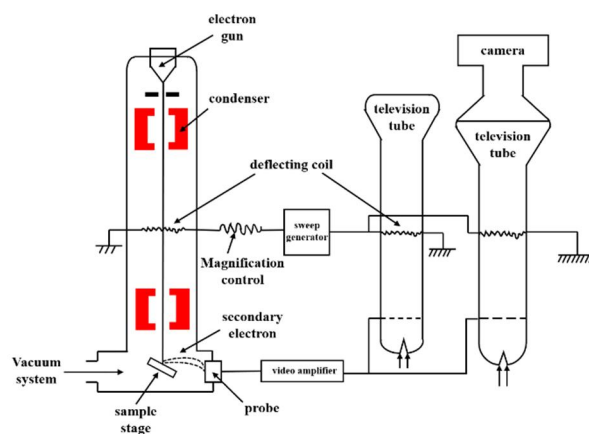


**Figure 3.4** Structure diagram of scanning electron microscope (SEM).

From the mid-1960s, scanning electron microscope (SEM) using as commercial electron microscope is a new type of electronic optical instrument which has been developed rapidly.<sup>104,105</sup> SEM has been applied in much research worldwide and industrial department as chemistry, biology, medical science, metallurgy, material science and semiconductor manufacturing. In Fig.3.4, there is the structure diagram of



SEM with several component systems. Of which most important systems are the electronic optical system, signal detection processing and display system, and vacuum system.

The working mechanism of SEM is shown as following. Several electron beams emitted by the electron gun are converged by the magnetic lens system under the action of the accelerating voltage, and then focused on the surface of the sample. Subsequently, under the action of the scanning coil installed on the final lens, the electron beam is scanned on the surface of the sample.<sup>106</sup> Along with the interaction of the high-energy electron beam with the sample material, various information will be generated as a result: secondary electrons, back-reflected electrons, absorbed electrons, X-rays, auger electrons, cathodoluminescence and transmission electrons. These signals are received by the corresponding receiver followed being enlarged and sent to the grid of the television tube with modulating the brightness. The current passing through the scanning coil corresponds to the brightness of the television tube which is means a bright spot appears on the fluorescent screen when the electron beam hits a point on the sample. Finally, we can observe various characteristic images on the surface of the sample through the fluorescent screen.<sup>107,108</sup>

Due to working mechanism of SEM, the sample must have excellent electrical conductivity. Otherwise, charge accumulation and discharge will occur, causing the incident electron beam to deviate from the normal path. This will result in unclear images and even impossible to observe or take pictures. One of solution is coating platinum or other metal conductive film on the surface of materials.

Transmission Electron Microscope (TEM) also is a very useful tool in the fields of materials, physics, chemistry, and life sciences similar with SEM. We often need to use TEM to obtain information on the surface (or morphology) and internals of samples. For example, scientific researchers can obtain the morphology of the new coronavirus by Cryo-TEM. It is of great help for us to understand the materials and to further deal with the materials in a targeted manner.<sup>109</sup>

Different with SEM using a set of specific coils to scan the sample in a raster pattern and collecting scattered electrons, TEM normally uses transmission electrons to collect the Electrons passing through the sample. Thus, TEM will provide sample internal structure as crystal structure and state of stress not only the surface morphology. The comparison for the properties of three different microscope (optical microscope, SEM, TEM) is shown in Table 3.2.

**Table 3.2** Comparison for the properties of different microscope.

	OM	SEM	TEM
Magnification	1-2000	5-200000	100-80000
Resolution	Highest	0.1 $\mu\text{m}$	0.8 nm
	Professional	0.2 $\mu\text{m}$	6 nm
	Ordinary	5 $\mu\text{m}$	10-50 nm
Focal Depth	Bad	Good	Good
Vision	Mid	Large	Small
Repair	Simple	Simple	Hard
Sample preparation	Metallographic	Any surface	Film
Price	Low	High	High

### 3.4 Electrochemical Measurements

#### 3.4.1 Lithium-ion batteries

##### (1) Electrodes and electrolyte

The coin half-cell (CR2025-type) with a working electrode containing the synthesized sample and lithium foil counter electrode was assembled as followed. The

working electrodes were prepared with 70 wt.% of active materials, 15 wt.% of super-P carbon black, and 15 wt.% of polyvinylidene fluoride (PVDF 10 wt.% in NMP) binder. The electrode mixtures were cast onto a copper foil, followed by drying in a convection oven at 130 °C for 30 min and subsequently vacuum-dried at 60 °C for 12 h. Li metal as a counter electrode, a porous polypropylene film as a separator, and 1 M of LiPF<sub>6</sub> in a 1:1:1 (v/v) mixture of ethylene carbonate, dimethyl carbonate, and ethyl methyl carbonate as the electrolyte were also used for the coin cell assembly.

## (2) Half-cell measurements

Firstly, we need to transfer the prepared working electrodes to the glove box in a protective atmosphere, and then prepare the button battery assembly parts: negative cases, metal lithium sheets, separator, gaskets, spring sheets, positive cases, electrolyte. In addition, a tablet die, pipette and insulated tweezers are required. Secondly, the negative electrode case is laid on the insulating table, and then the metal lithium sheet is placed in the center of the negative electrode case. Subsequently, the metal lithium sheets are flattened with a tablet die, then separator flat is laid on the upper layer of the lithium sheet followed adding amount of electrolyte by the pipette. Finally, we use insulated tweezers to place working electrode, gasket, spring sheet and positive electrode case on the upper layer of the diaphragm in turn, where the active material side of the working electrode should be close to the separator.

Further, we use insulated tweezers to place the button battery with the negative side up on the button battery sealing machine mold. Normally, the pressure of the machine mold is adjusted to 800Pa and pressed for 5 seconds to complete the assembly. The battery is taken out with insulated tweezers and cleaned with acetone several time for removing the overflowing electrolyte. The completed half-cell coin needs to be aged for one day.

### 3.4.2 Supercapacitors

The electrochemical workstation was VSP50 (Biologic) and CHI660E (CH Instrument ins.).

#### (1) Three electrodes system

The electrochemical performance of the prepared samples was conducted in a three-electrode system with aqueous 2 M KOH electrolytes, a platinum wire as the counter electrode and Ag/AgCl as the reference electrode. The G-NH//CC and M-NH//NF directly served as the working electrode without a binder. However, the working electrode of B-CNQDx-Ni were prepared by mixing active materials (Ni(OH)<sub>2</sub>, B-CNQDx-Ni), conductive materials (Super P carbon black) and binder (10% PVDF which solvent was NMP) with the mass ratio of 80:10:10. Then the mixture was dropped on the glassy carbon electrode with drying in an oven at 60 °C.

#### (2) Two electrodes system

The solid-state symmetric supercapacitor was fabricated by assembling two pieces of materials (G-NH//CC and M-NH//NF) as positive and negative electrodes with PVA/KOH gel electrolyte and a filter paper as a separator. The PVA/KOH gel electrolyte was prepared as follows: 6 g of PVA and 3.5 g of KOH was mixed with 60 ml of DI water with continuous stirring at 90 °C until a clear solution was obtained. Then, the solution was cooled down to room temperature for the gel formation. Two electrodes were dipped into the gel electrolyte for 10 min and then assembled face to face with filter paper between them using gentle pressure.

### 3.4.3 Electrochemical impedance spectroscopy (EIS)

Electrochemical impedance spectroscopy (EIS) is a powerful method to test the performance of electrode materials.<sup>110</sup> The EIS test is usually to collect the impedance data of the capacitor under the open circuit voltage and a small amplitude (normally 5

mV), to obtain the relationship between the impedance ( $|Z|$ ) and the frequency ( $f$ ). It uses a waveform generator to generate a small sinusoidal potential signal, and then, applies that to the electrochemical system through a potentiostat. Following, it uses lock-in amplifier or spectrum analyzer to convert the output current/potential signal into impedance and its modulus or phase angle. By changing the frequency of the sine wave, different modulus and phase angle can be obtained and thus the electrochemical impedance spectroscopy is composed. Since the disturbance electrical signal is an AC signal, electrochemical impedance spectroscopy is also called AC impedance spectroscopy.

Usually, we use Bode plots or Nyquist plots to present data results of electrochemical impedance spectroscopy. The Nyquist plots model is shown in fig.3.5.

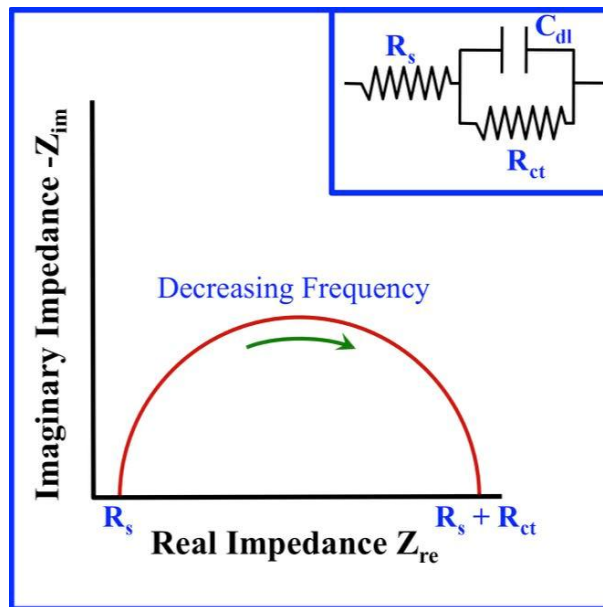


**Figure 3.5** The Nyquist plots model and inset equivalent circuit diagram.

The curve represents the type of experimental data that would be generated for a bare metal experiencing. In this case, the solution resistance ( $R_s$ ) is found using the high frequency data while the low frequency data defined the value for the charge transfer resistance ( $R_{ct}$ ).<sup>111</sup>

### 3.4.4 Calculations of electrochemical performance

Cyclic Voltammetry (CV) is one of the most basic and vital measurements during electrochemical performance test of electrode materials.<sup>112</sup> Normally, electrode material is coated on the surface of inert electrode as glassy carbon, graphite or platinum, and the CV curve can be recorded in the specific electrolyte. CV applies to both of electric potential changes in two electrodes system (between negative and positive) and three electrodes system (between working electrode and reference electrode). The rate and range of potential changes is named as scan rate and voltage window. The instantaneous current during scan refers to the electrochemical reaction. The specific capacitance is calculated by CV curves as follow formula:

$$C_s = \int IdV / (ms\Delta V) \quad (3.5)$$

Where  $C_s$  is specific capacitance (F/g),  $I$  is corresponding current (A) under CV curve,  $m$  is the mass of active materials (g),  $s$  is the scan rate (V/s) and  $\Delta V$  is the voltage window (V).<sup>113</sup> We can determine the working potential and voltage window of electrode materials, as the same time, reversibility of charge/discharge process, specific capacitance and energy properties can be investigated. Moreover, we can define the working mechanism (EDLCs or PCs) by CV test in SCs.

Galvanostatic charge/discharge (GCD) is another substantial electrochemical measurement for LIBs or SCs which is the most extensive, common, and accurate method to character the electrochemical properties at constant current.<sup>114</sup> We get the patterns of putout potential (E) vs. time (t) by charge/discharge test for working electrode at galvanostatic. In consequence, it is key to choose a suitable current for getting data in GCD test. Through three electrodes system of GCD test, specific capacitances, reversibility, and voltage window of the electrode materials also can be studied. The specific capacitance is calculated by GCD curves as follow formula:

$$C_s = I\Delta t / (m\Delta V) \quad (3.6)$$

Where  $C_s$  is the specific capacitance of electrode material (F/g),  $I$  is the corresponding current (A),  $m$  is the mass of active materials (g) and  $\Delta V$  is the voltage window (V).<sup>115</sup> Furthermore, we can get three kernel parameters from GCD that is the total capacitance of SC or LIBs ( $C_T$ ), equivalent series resistance ( $R_{ES}$ ) and working potential (V). These parameters can be used for investigating other properties likes time constant, power density and energy density, leakage and peak current, or cycling performance.

As shown in Fig.1.2, energy density and power density are two important parameters for energy storage device. If a system has a high energy density, it will be able to store a lot of energy in a small amount of mass. If a system has a high-power density, it will output large amounts of energy based on its mass. The calculation method of energy density and power density is shown as follow:

$$E = \frac{CV^2}{2} \quad (3.7)$$

$$P = \frac{E}{\Delta t} \quad (3.8)$$

Where  $E$  is energy density (Wh/g),  $P$  is power density (W/g)  $C$  is specific capacitance (F/g),  $V$  is potential window (V) and  $\Delta t$  is the discharging time (s).<sup>116,117</sup>

## Chapter 4: Hierarchical NiO (h-NiO) microtubes for Lithium-ion

### Batteries

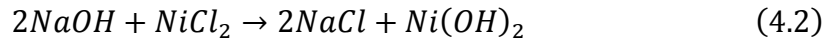
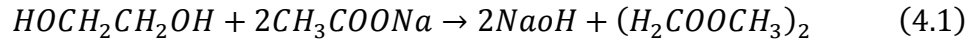
#### 4.1 Introduction

Transition metal oxides (TMOs) and their composites are considered to be the most promising anode materials for lithium-ion batteries (LIBs) due to their natural abundance, low cost, and their high theoretical capacity in comparison to the commercial graphite anode ( $372 \text{ mAh}\cdot\text{g}^{-1}$ ). NiO is one of TMOs with high theoretical capacity ( $718 \text{ mAh}\cdot\text{g}^{-1}$ ) and high volumetric energy density. But NiO suffers from a huge volume change during the charge/discharge process, which may lead to electrode pulverization and electrical detachment, resulting in poor capacity retention performance. One of solution is synthesizing hierarchical nanostructured NiO materials which can provide large specific surface area (SSA) to increase the effective contact with electrolyte, providing a fast ion/electron transfer, large reaction surface area, and good strain accommodation of large volume change to enhance electrochemical performance.

Nickel hydroxide has two kinds of phase named as  $\alpha$ -phase and  $\beta$ -phase. In this chapter, we demonstrate a simple wet-chemical method without using template or surfactant, followed by a conventional thermal annealing step to synthesize hierarchical NiO (h-NiO) microtubes. And we used  $\alpha$ -Ni(OH)<sub>2</sub> as precursor which is isostructural with a hydrotalcite-like structure having the intercalated water.<sup>118,119</sup> After calcination, the intercalated water will be evaporated, and hierarchical architecture will be occurrence. For these reasons, the morphology of NiO which used  $\alpha$ -phase as precursor makes electrons and ions transfer more easily.<sup>119</sup> For synthesizing new materials more quickly, at low cost, and under environmentally more friendly conditions,<sup>120</sup> in this article, we use a facile wet chemistry method to generate Ni(OH)<sub>2</sub>. With the reaction times going, the morphology also changes from nanorods to flake



covered nickel hydroxide nanotubes ( $\alpha$ -FC-Ni(OH)<sub>2</sub>). And after calcination, the sample transformed into nickel oxide without morphology change. The chemical equations are as below.



The obtained hierarchical architectures are hollow tubes covered with NiO nanoflakes, which provides more active site for the efficient insertion and extraction of Li-ions. When evaluated as an anode electrode for LIBs, the h-NiO microtubes exhibit large reversible capacity, good rate capability, and excellent cycle stability. The novel h-NiO microtubes are a promising candidate anode material for high performance LIBs.

We used X-ray diffraction (XRD), field-emission scanning electron microscopy (FE-SEM) and transmission electron microscopy (TEM) to characterize the morphologies and structure of the obtained composites. The SSA was analyzed from the results of N<sub>2</sub> adsorption and desorption at 77.3 K (Quantachrome Instruments), calculated using the Brunauer–Emmett–Teller (BET) method.

## 4.2 Morphologies and Structures

Nanostructured Ni(OH)<sub>2</sub> precursors were first synthesized via a simple wet-chemical method, followed by a subsequent calcination process, in order to prepare hierarchical NiO microtubes. Fig.4.1 shows the FE-SEM images of the prepared Ni(OH)<sub>2</sub> precursor products at 170 °C for different reaction times. After a 0.5 h reaction, it can be seen in Fig.4.1a that Ni(OH)<sub>2</sub> rods with diameter of ~1 μm are obtained. When the hydrothermal time was prolonged to 1 h, the surfaces of Ni(OH)<sub>2</sub> rods were decorated with small particles (Fig.4.1b and inset image), consisting of nanosheets. With the reaction time reaching 3 h, the morphology of Ni(OH)<sub>2</sub> was noticeably transformed as shown in Fig.4.1c and the inset image. It can be clearly seen that porous

Ni(OH)<sub>2</sub> microtubes were obtained, where flexible nanosheets covered the Ni(OH)<sub>2</sub> microtubes so as to form a hierarchical nanostructure. After a longer reaction of 4 h, hierarchical nanostructure of Ni(OH)<sub>2</sub> microtubes were collapsed or broken into pieces as seen in Fig.4.1d.

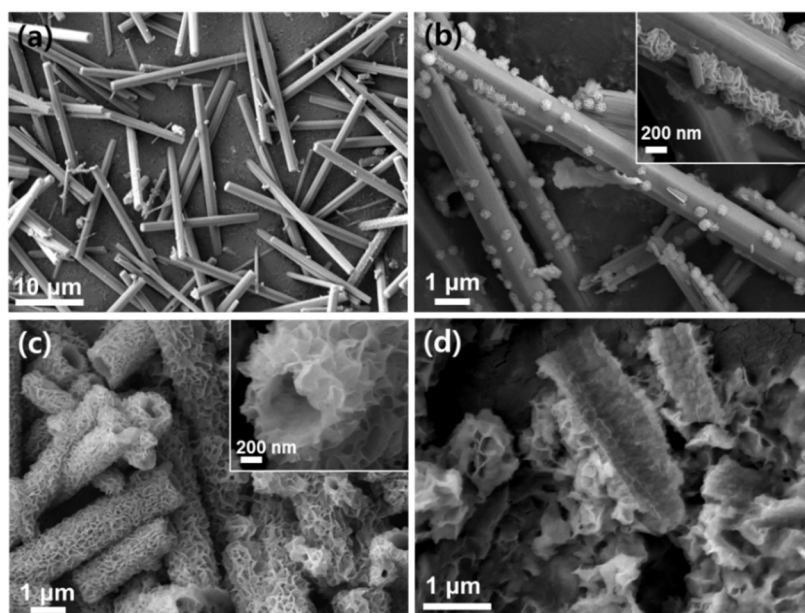


**Figure 4.1** FE-SEM image of the obtained Ni(OH)<sub>2</sub> precursor products at the different reaction time. (a) 0.5 hr, (b) 1 hr, (c) 3 hr, and (d) 4 hr.

The crystalline structures of the corresponding Ni(OH)<sub>2</sub> samples with different reaction time were analyzed by XRD. Fig.4.2a shows that the XRD patterns of the as-prepared Ni(OH)<sub>2</sub> samples can be indexed to a rhombohedral Ni(OH)<sub>2</sub>·0.75H<sub>2</sub>O phase (JCPDS No. 38-0715), which is also regarded as  $\alpha$ -Ni(OH)<sub>2</sub>. Four major diffraction peaks around at 10, 22, 33, and 60° can be well assigned to the (003), (006), (101), and (101) planes of  $\alpha$ -Ni(OH)<sub>2</sub>, respectively. Another forceful characterization analysis is Thermogravimetric Analysis (TGA) for precursor Ni(OH)<sub>2</sub>. TG curves as presented in Fig.4.2b-c shows two main steps about the decomposition of Ni(OH)<sub>2</sub>. From the room temperature 25 °C to 200 °C which is the first step in the TGA process, h-Ni(OH)<sub>2</sub> loss 44.55% of weight that could be cause by desorption of layer water on the surface of  $\alpha$ -Ni(OH)<sub>2</sub>.<sup>121</sup> However, the Ni(OH)<sub>2</sub> nanorods just loss 9.68% of weight that proves the mechanism of h-Ni(OH)<sub>2</sub> formation as expound before. The second step from 200 °C to

350□ is transformation  $\text{Ni}(\text{OH})_2$  to  $\text{NiO}$ , the weight loss of nanorods and h-NiO nanotubes are 47.31% and 27.18%, respectively.

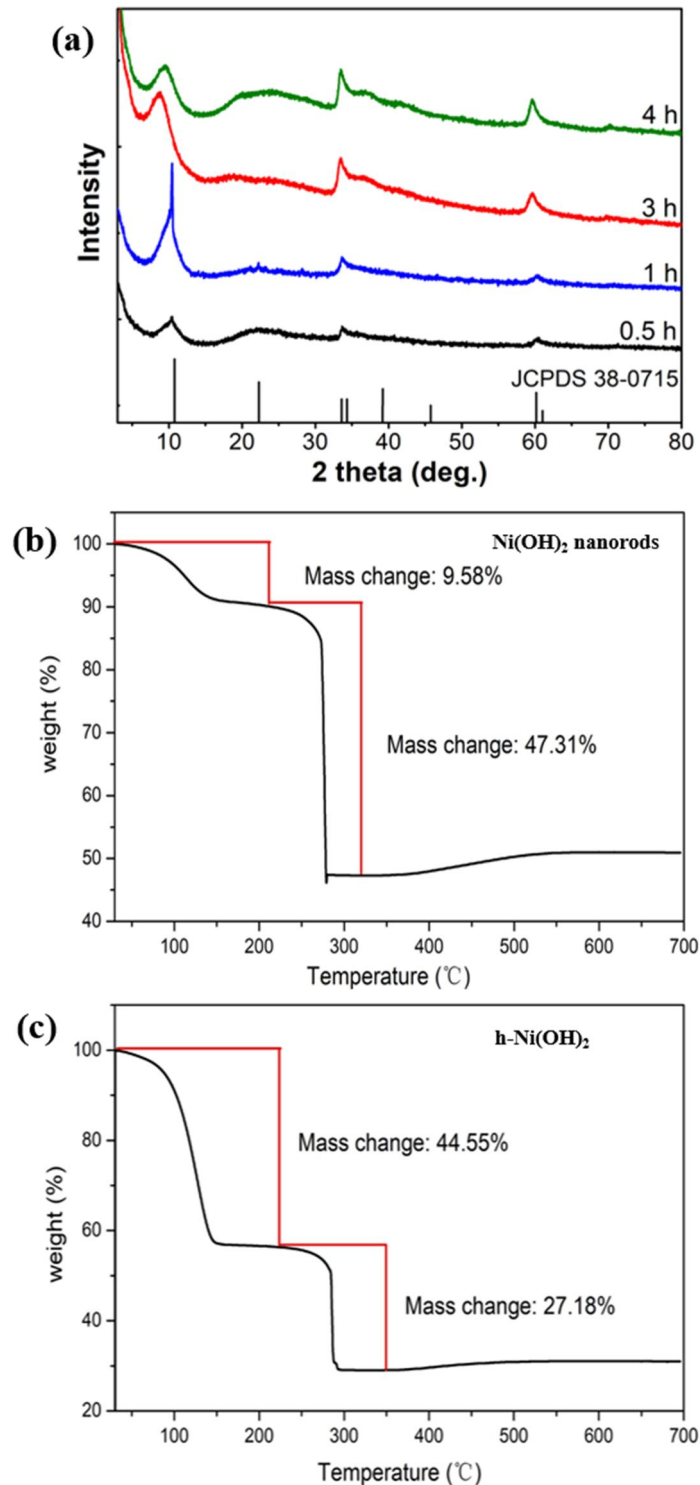


**Figure 4.2** (a) XRD patterns of the obtained  $\text{Ni}(\text{OH})_2$  precursor products at the different reaction time, (b-c) TGA curves of  $\text{Ni}(\text{OH})_2$  nanorods and h- $\text{Ni}(\text{OH})_2$ .

The as-synthesized hierarchical Ni(OH)<sub>2</sub> microtubes (h-Ni(OH)<sub>2</sub> microtubes) are then transformed to crystallize hierarchical NiO microtubes (h-NiO microtubes) by calcination at 350 °C for 1 h under nitrogen. Fig.4.3a shows the corresponding XRD patterns of h-Ni(OH)<sub>2</sub> microtubes and h-NiO microtubes. Following calcination, the patterns of h-Ni(OH)<sub>2</sub> microtubes completely convert into the NiO phase. All of the peaks in the pattern can be indexed to NiO with the face-centered cubic phase (JCPDS No. 47-1049). No diffraction peaks of α-Ni(OH)<sub>2</sub> can be observed, indicating that the h-Ni(OH)<sub>2</sub> microtubes are completely transformed to NiO after calcination. The morphology and structural characterization of the calcinated sample was performed by SEM as shown in Fig.4.3b and c. It can be observed that the h-Ni(OH)<sub>2</sub> microtube structure is well retained after the calcination and the hierarchical nanostructure of the surface of h-Ni(OH)<sub>2</sub> microtubes is also well reserved. As can be seen in the enlarged image of Fig.4.3c, the NiO microtubes are completely covered with nanosheets which are grown perpendicularly over the surface of tubes. In addition, the nanosheets of NiO are connected to each other, forming quite a lot of voids between nanosheets on NiO microtubes.

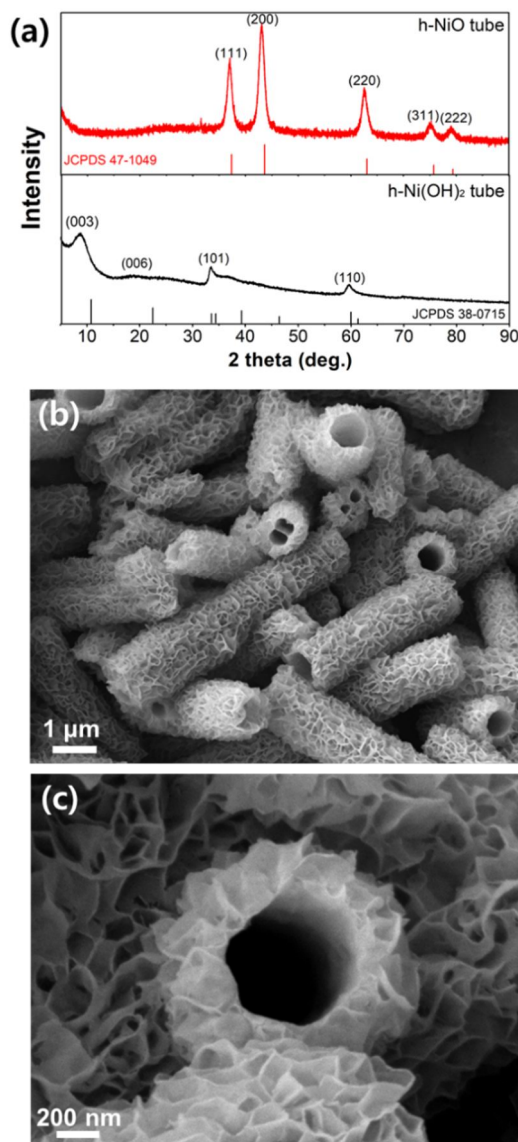


**Figure 4.3** (a) XRD patterns of the h-Ni(OH)<sub>2</sub> and h-NiO. (b) FE-SEM image of the h-NiO and (c) its high magnified image.

The detailed structural features of the h-NiO microtubes were further investigated by TEM analysis. The h-NiO microtube structure can be observed from the low-magnification TEM image in Fig.4.4a, which indicates that the NiO nanosheets are interconnected on the hollow NiO microtube. The high-resolution TEM image of nanosheets on the h-NiO microtubes is shown in Fig.4.4b. The measured lattice spacing of 0.24 nm is consistent with the (111) crystal plane of cubic NiO phase. The specific surface area of the h-NiO microtubes were further characterized by BET measurement and the N<sub>2</sub> adsorption-desorption isotherms are shown in Fig.4.4c. As a control sample,

BET measurement was also carried out for the NiO rods sample from the calcination of the Ni(OH)<sub>2</sub> rods of 0.5 h reaction. The specific surface area of h-NiO microtubes is calculated to be 98.5 m<sup>2</sup>/g, which is much larger than the 21.9 m<sup>2</sup>/g value of the NiO rods sample. The relatively high surface area of h-NiO microtubes can be ascribed to the hierarchical nanostructures of nanosheets and hollow microtubes. The unique nanostructure of h-NiO microtubes can provide a large electroactive surface area and porous nanostructure for the effective penetration of electrolyte and also buffer the volume expansion during the charge-discharge process. Therefore, these features of h-NiO microtubes can be beneficial to the superior electrochemical performance for charge transfer and cyclic stability.

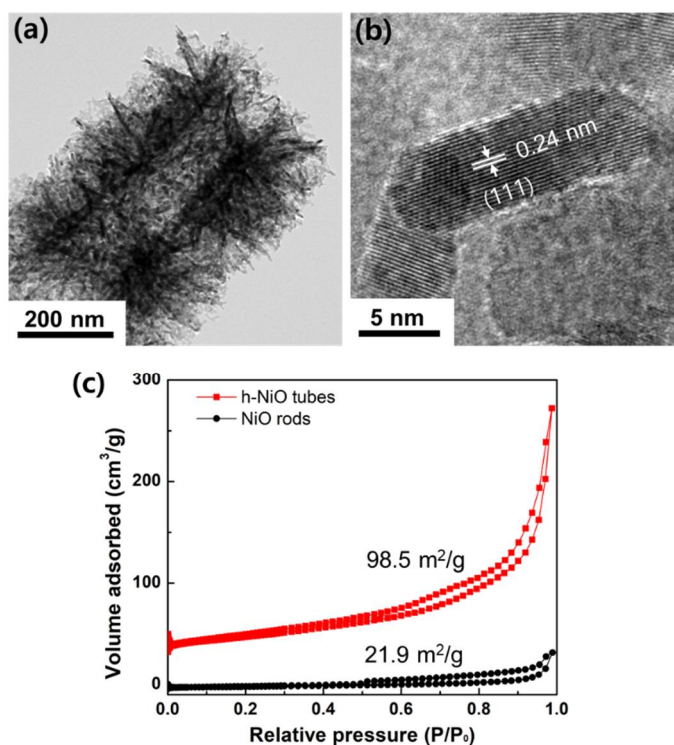


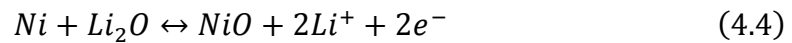
**Figure 4.4** (a) TEM image and (b) HR-TEM image of h-NiO microtubes. (c) Nitrogen adsorption-desorption isotherm of h-NiO microtubes and NiO rods.

**Table 4.1** Surface properties of nickel hydroxide and its calcined products.

samples	Surface Area (m <sup>2</sup> g <sup>-1</sup> )	Pore Volume (cc g <sup>-1</sup> )	Average Pore Radius (Å)
FC-NiO nanotubes	98.520	0.380	29.778
NiO nanorods	21.947	0.061	20.460

### 4.3 Electrochemical Performance

The electrochemical performance of the h-NiO microtubes was evaluated as an anode electrode for LIBs using half cells. Cyclic voltammetry (CV) of the initial six cycles for the NiO rod and h-NiO microtube electrodes were tested in the voltage range from 0.01-3.0 V at a scan rate of 0.5 mV·s<sup>-1</sup>. As shown in Fig.4.5, a strong reduction peak is observed at around 0.2 V in the first scan for the h-NiO microtubes, while a broad peak is observed at around 0.17 V for the NiO rods, which corresponds to the reduction of NiO to metallic Ni accompanied by the formation of Li<sub>2</sub>O and the formation of a solid electrolyte interface (SEI) layer induced by the decomposition of electrolyte.<sup>122,123</sup> The process is according to eq.4.4 as below.



The subsequent reduction peaks shift to 0.95 and 1.0 V for the NiO rods and h-NiO microtubes, respectively. In the anodic scan, a strong oxidation peak is observed at around 2.3 V and a weak peak is observed at around 1.6 V for both NiO rods and h-NiO microtubes, indicating the faraday reaction for the NiO formation and LiO<sub>2</sub> decomposition. In comparing the CV curves of the NiO rods and h-NiO microtubes, the current densities of peaks for the h-NiO microtubes are much larger than those for the NiO rods, which suggests higher capacity and faster reaction kinetics for the h-NiO microtubes. Also, the h-NiO microtubes exhibits smaller potential difference (1.22 V) between the oxidation and reduction peak in the second cycle than that of the NiO rods (1.44 V), suggesting a superior reversible and stable redox reaction between NiO and Li for the h-NiO microtubes.

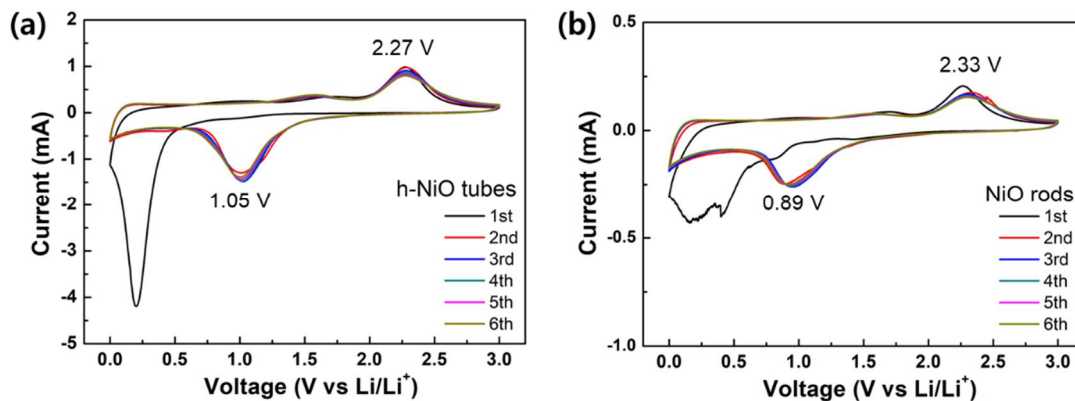


**Figure 4.5** Cyclic voltammetry curves of (a) h-NiO microtubes and (b) NiO rods.

The cycle performance was further evaluated at the current density of 0.5 C (1 C = 717 mA·g<sup>-1</sup>) and Fig.4.6a shows the discharge-charge capacity of the NiO rods and h-NiO microtubes electrodes for 200 cycles. It is evident that, as compared to the NiO rods, the h-NiO microtubes exhibit superior specific capacity over the cycles. The initial discharge and charge capacities of the h-NiO microtubes are 1302 and 915 mAh·g<sup>-1</sup>, respectively. The corresponding irreversible capacity loss of 29.7% could be attributed to the electrolyte decomposition and irreversible formation of SEI layer. Then, the specific capacity of the h-NiO microtubes decrease to 510 mAh·g<sup>-1</sup> after 120 cycles. In addition, the capacity increases during the subsequent cycles and reaches 747 mAh·g<sup>-1</sup> after 200 cycles, which may be ascribed to the formation of a polymeric gel-like film resulting from kinetically activated electrolyte degradation.<sup>124,125</sup> Another reason for increasing capacities of h-NiO microtubes after is because of Ni will act as effective catalysts for formation/decomposition of SEI layer during the charging process.<sup>126,127</sup> On the other hand, for the NiO rod electrode, the initial discharge and charge capacities are 660 and 422 mAh·g<sup>-1</sup>, respectively, with the irreversible capacity loss of 36%. Then, the specific capacity of the NiO rods decreases continuously after 30 cycles and reaches 140 mAh·g<sup>-1</sup> after 200 cycles. These results suggest that the h-NiO microtubes have a cycling performance superior to that of the NiO rods. The rate capability measurements of the h-NiO microtubes and NiO rods were performed at different current densities and the results are presented in Fig.4.6b. It can be seen that the h-NiO microtube electrode delivers discharge capacity of 884, 814, 725, 672, and 616 mAh·g<sup>-1</sup> as the current



density gradually increases from 0.1 to 0.2, 0.5, 1.0 and 2.0 C, respectively. Importantly, when the current density returns to 0.1 C, the discharge capacity can restore to 928 mAh·g<sup>-1</sup>, demonstrating a superior high-rate performance for high power LIBs. By contrast, the NiO rods exhibit much lower discharge capacity over the whole range than the h-NiO microtubes. According to the above results, the excellent electrochemical performance of the h-NiO microtubes compared to the NiO rods can be attributed to the unique hierarchical nanostructures, which provide a larger area for electrochemical reaction with lithium and relieve the strain induced by the volume change during the charge-discharge cycles. In addition, the nanosheet structures of the h-NiO microtubes offer a short pathway for Li-ion diffusion, thereby enhancing the rate capability.

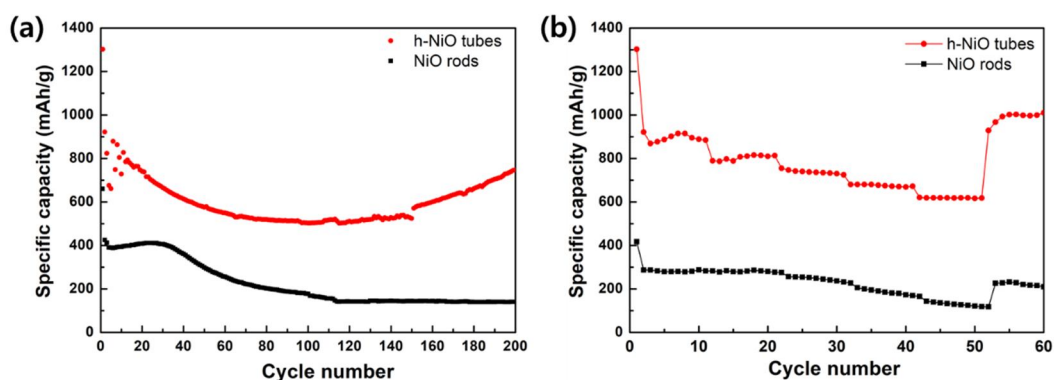


**Figure 4.6** (a) The cycle performance and (b) the rate performance of h-NiO microtubes and NiO rods.

Electrochemical impedance spectroscopy (EIS) measurements were further performed in order to elucidate the superior electrochemical performance of the h-NiO microtubes to that of the NiO rods, and the resulting Nyquist plots are presented fresh electrode and after five cycles as shown in Fig.4.7. The diameter of the semicircle in the high-middle frequency region can be assigned to the charge-transfer resistance ( $R_{ct}$ ) through the electrode and electrolyte, which is a large portion of the overall kinetic resistance of the cell. The diameters of the semicircles for the h-NiO microtubes and NiO rods decrease after five cycles, indicating the decrease of the charge transfer resistance, due to the wetting process between the electrode and the electrolyte. Moreover, it is clear that the charge transfer resistance for the h-NiO microtubes prior

to cycling and after five cycles is smaller than that of the NiO rods. This discrepancy confirms that the hierarchical nanostructure of the h-NiO microtubes facilitates the Li-ions and electron transfer and improve the electrical conductivity, resulting in the highly enhanced electrochemical performance of the h-NiO microtubes.

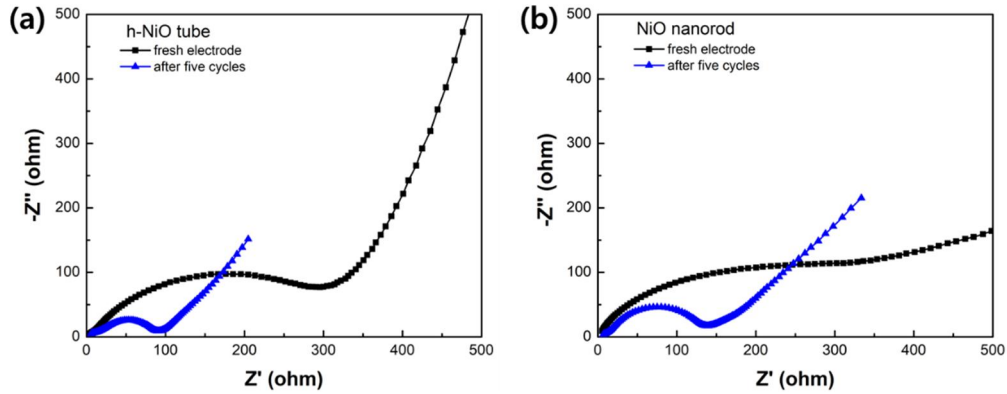


**Figure 4.7** Nyquist plots of fresh electrode and after five cycles for (a) h-NiO microtubes and (b) NiO rods.

#### 4.4 Summary

The hierarchical nanostructured NiO microtubes have been successfully synthesized by a simple wet-chemical method followed by the calcination of  $\alpha$ -Ni(OH)<sub>2</sub> precursor. In the h-NiO microtubes, the nanosheets are vertically synthesized on the surfaces of tubes and connected to each other, showing a larger surface area with many voids. The unique hierarchical nanostructure of h-NiO microtubes plays a crucial role in exhibiting the superior electrochemical performance for LIBs, which not only relieves the stress caused by the volume change during the charge-discharge cycles, but also provides a high surface area and pore volume to facilitate the electrochemical reaction as well as the electron and ion transfer. Therefore, compared to the NiO rods, the synthesized h-NiO microtubes as the anode electrode for LIBs demonstrate a superior cycle performance and excellent rate capability. The h-NiO microtubes show a high discharge capacity of 747 mAh·g<sup>-1</sup> at a current density of 0.5 C after 200 cycles, and also exhibit a discharge capacity of 616 mAh·g<sup>-1</sup> at a current density of 2 C.

Therefore, the proposed synthesis method and the h-NiO microtubes can be a promising method for improving the electrochemical performance in the application of LIBs.

## Chapter 5: Graphene quantum dots/Ni(OH)<sub>2</sub> nanocomposites on

### Carbon Cloth for Supercapacitors

#### 5.1 Introduction

As we all known, the main mechanism of lithium ion batteries is intercalate/de-intercalate the Li<sup>+</sup> which limits the charge/discharge rate of batteries and makes high costs. However, supercapacitors are other than lithium ion batteries, because of that they store charge by electrode materials surface reactions, they have high power density, stable property, short charge/discharge time, long cycle life and excellent high/low temperature performance. But researching into supercapacitors is still a long way off, we need to continuously improve the electrode material for increasing the power density and cycle stability of supercapacitors.

Pseudocapacitor, which mainly utilize the fast and reversible surface Faradic redox reaction of transition metal oxide and hydroxide materials such as MnO<sub>2</sub>, NiO, Ni(OH)<sub>2</sub> and Co<sub>3</sub>O<sub>4</sub>, can deliver a substantially higher specific capacitance. Among these metal oxide-based materials, Ni(OH)<sub>2</sub> has received significant attention for its high theoretical specific capacitance, its high stability in alkaline electrolyte, its abundance, and environmentally friendly. However, the actual specific capacitance of Ni(OH)<sub>2</sub>-based supercapacitor highly depends on its nanostructures and crystal structure, and the poor electrical conductivity ( $\sim 10^{-17}$  S·cm<sup>-1</sup>) Ni(OH)<sub>2</sub> is significantly lower than its theoretical value. To solve these drawbacks, various research has proposed the use of nanocomposites of Ni(OH)<sub>2</sub> with high electrically conductive carbon-based materials such as graphene, carbon nanotubes, and activated carbon.

Herein, in this chapter, we report a simple and cost-effective synthesis process for GQDs/Ni(OH)<sub>2</sub> nanocomposites on CC (denoted as G-NH//CC), which is directly used as binder-free electrodes in high-performance flexible supercapacitors. The G-NH//CC was prepared through simple hydrothermal synthesis of Ni(OH)<sub>2</sub> in the presence of

GQDs. The as-prepared sample shows a specific capacitance of  $1825 \text{ F}\cdot\text{g}^{-1}$  at a scan rate of  $1 \text{ A}\cdot\text{g}^{-1}$  and good cycle stability for 8000 cycles. Also, we assembled all-solid-state symmetric supercapacitor using the G-NH//CC electrodes, which demonstrates the excellent performance of high energy density of  $80.8 \text{ Wh}\cdot\text{kg}^{-1}$  at power density  $2021 \text{ W}\cdot\text{kg}^{-1}$  with good mechanical stability. These results show that the G-NH//CC can be a promising electrode for high-performance flexible supercapacitors.

**Table 5.1** Electrochemical performance of recently Ni(OH)<sub>2</sub>-Carbon materials.

Materials	Capacitance	Cycling performance	Reference
$\alpha$ -Ni(OH) <sub>2</sub>	516 F/g at 0.5 A/g	84% (1000 cycles)	Ref.128
$\beta$ -Ni(OH) <sub>2</sub>	324 F/g at 5 mV/s	78% (500 cycles)	Ref.129
Ultrafine $\beta$ -Ni(OH) <sub>2</sub> nanosheets	524.5 C/g at 5 A/g	80.8% (5000 cycles)	Ref.130
Ni(OH) <sub>2</sub>	701 F/g at 1 A/g	84.16% (5000 cycles)	Ref.131
Ni(OH) <sub>2</sub> hollow spheres	700 F/g at 1 A/g	76% (2000 cycles)	Ref.132
Ni(OH) <sub>2</sub> @NG hydrogel	896 F/g at 0.5 A/g	85.9% (5000cycles)	Ref.133
ZnO@Ni(OH) <sub>2</sub> nanoflakes	1830 F/g at 2 A/g	70% (1000 cycles)	Ref.134
CNT@Ni(OH) <sub>2</sub> core-shell composites	1136 F/g at 2 A/g	92% (1000 cycles)	Ref.135
ZnO@Ni(OH) <sub>2</sub> arrays	2028 F/g at 10 A/g	68% (500 cycles)	Ref.136
Ag-rGO/Ni(OH) <sub>2</sub> composites	1220 F/g at 1 A/g	90.4% (2000 cycles)	Ref.137
<b>GQDs-Ni(OH)<sub>2</sub>@CFCs</b>	<b>1825 F/g at 1 A/g</b>	<b>97.2% (8000 cycles)</b>	<b>Our Work</b>

## 5.2 Morphologies and Structures

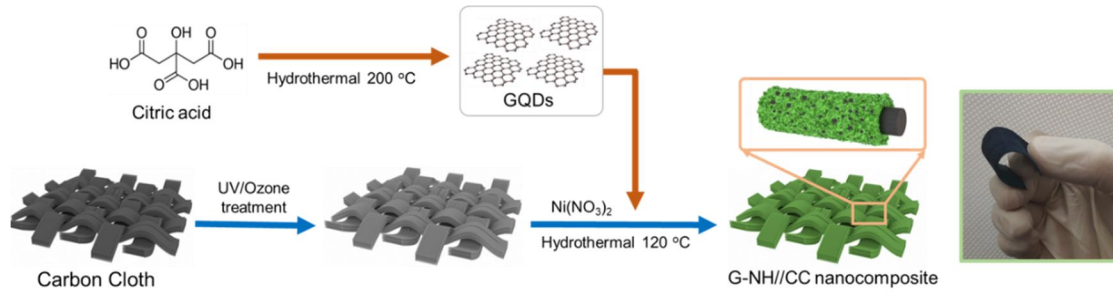
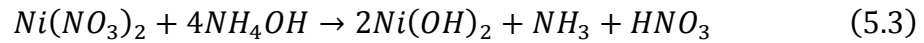
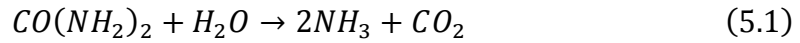


**Figure 5.1** Schematic illustration for the synthesis of GQDs/Ni(OH)<sub>2</sub> nanocomposite on carbon cloth.

The fabrication procedure of G-NH//CC is schematically shown in Fig.5.1. we used an ultraviolet/ozone treatment on the surface of carbon clothes to produce high levels of oxygen containing functional group which promotes crystal growth.<sup>138</sup> Then Ni(NO<sub>3</sub>)<sub>2</sub> was reacted with urea as precipitating agent at 120 °C to obtain Ni(OH)<sub>2</sub> growing on the surface of carbon clothes as follows:



Meanwhile there was a strong electrostatic adsorption between the Ni<sup>2+</sup> ion and graphene quantum dots because of the carbonxyl and hydroxyl groups on the GQDs.

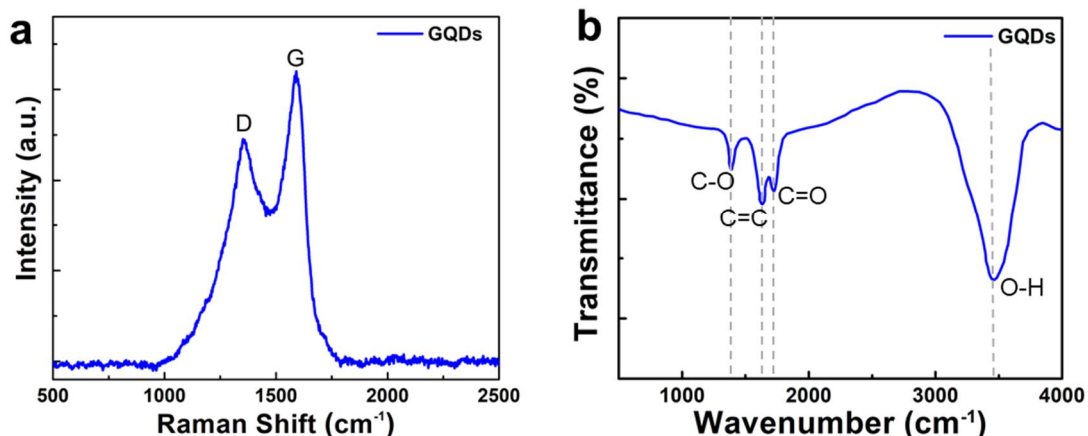


**Figure 5.2** (a) Raman spectra and (b) FT-IR spectra of the as-synthesized GQDs.

First of all, the as-synthesized GQDs was characterized by Raman spectroscopy and FT-IR (Fig.5.2). The Raman spectra of GQDs exhibits two distinct peaks of D-peak ( $\sim 1350\text{ cm}^{-1}$ ) and G-peak ( $\sim 1590\text{ cm}^{-1}$ ) and the FT-IR spectra shows characteristic peaks related to the deformation of C-O ( $\sim 1380\text{ cm}^{-1}$ ), in-plane vibration of C=C ( $\sim 1640\text{ cm}^{-1}$ ), the stretching vibration of C=O in the carboxyl group ( $\sim 1720\text{ cm}^{-1}$ ), and the stretching vibration of O-H ( $\sim 3460\text{ cm}^{-1}$ ). These results indicate the successful synthesis of GQDs by carbonization of citric acid.

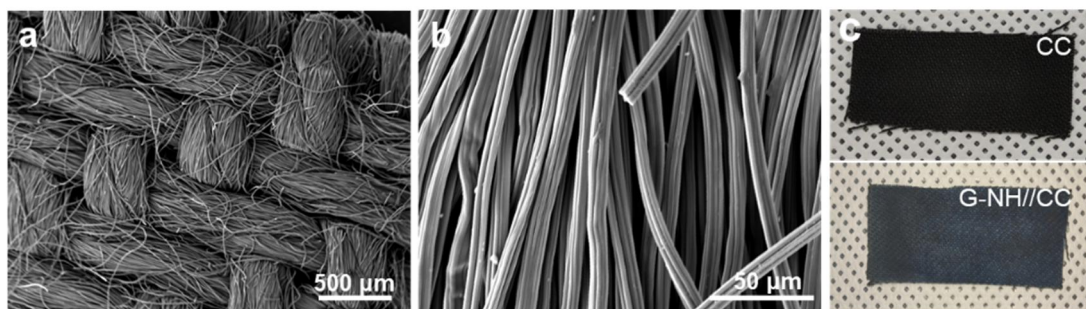


**Figure 5.3** (a-b) SEM images of pristine CC. (c) Photo images of pristine CC and as-synthesized G-NH//CC.

The pristine CC displays black color and consists of uniform carbon fibers with a smooth surface (Fig.5.3). After the hydrothermal reaction, the surface morphology of the G-NH//CC shows the formation of  $\text{Ni}(\text{OH})_2$  nanowalls vertically grown on the surface of carbon fibers, as shown in Fig.5.4a-c. It is also found that the G-NH//CC has similar nanostructure with NH//CC, but it has more irregular bumps on the surface of

carbon fibers (Fig.5.5). The HRTEM image of the G-NH//CC in Fig.5.5d shows that the GQDs are evenly bounded on the Ni(OH)<sub>2</sub> surface. Additionally, the high-resolution image in Fig.5.5e exhibits the lattice fringe of GQDs in the G-NH//CC sample, where the lattice spacing distance is 0.24 nm, corresponding to the (1120) lattice of graphene. The SEM image and corresponding elemental mapping images by energy-dispersive X-ray spectroscopy (EDS) in Fig.5.5f clearly show the uniform distribution of Ni, O, and C elements in the obtained G-NH//CC composite, confirming the successful synthesis of GQDs/Ni(OH)<sub>2</sub> nanocomposite.

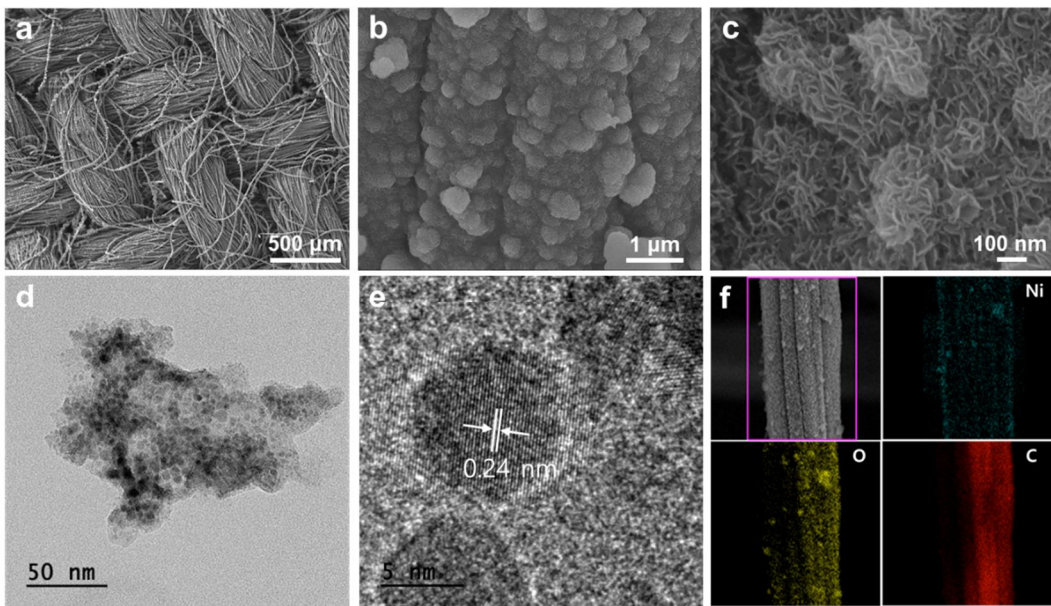


**Figure 5.4** (a-c) SEM images of G-NH//CC nanocomposite. (d) TEM image of G-NH//CC and (e) its high magnification image. (f) EDS elementary mapping of G-NH//CC.



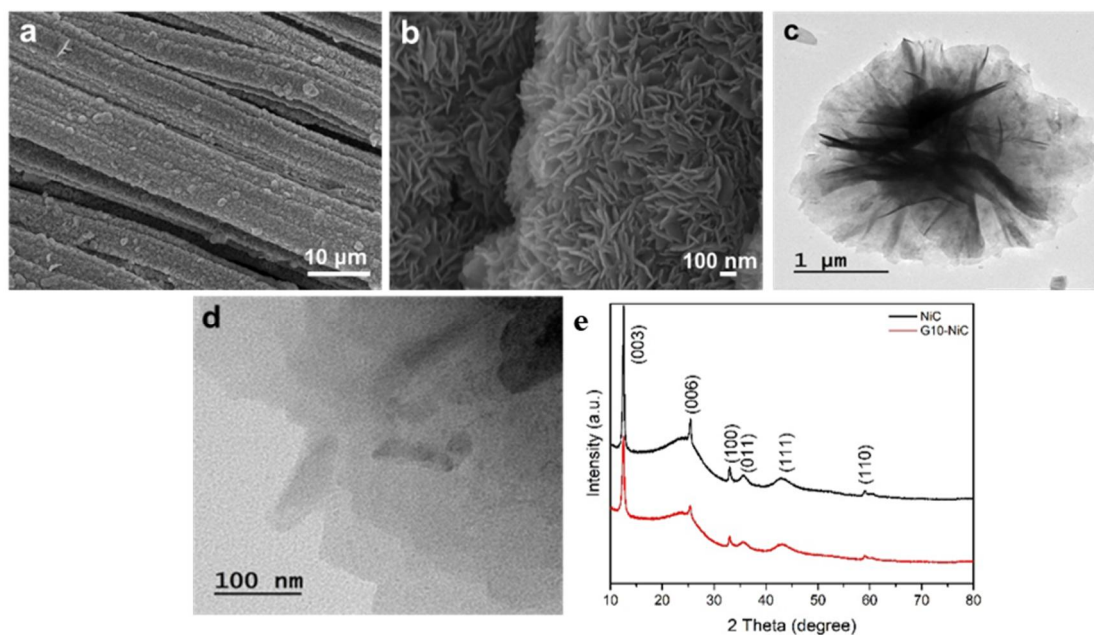


**Figure 5.5** (a-b) SEM images and (c-d) TEM images of NH//CC. (e) XRD spectra of GNH//CC and NH//CC.

The crystal structure and phase purity of the GNH//C and NH//C composites were characterized by XRD measurements (Fig.5.5e). The peaks located at 12.56°, 25.4°, 32.96°, 33.04°, 42.7° and 59.18° are from (003), (006), (100), (011), (111) and (110) planes of Ni(OH)<sub>2</sub> phase according to JCPDS No14-0117 card<sup>139</sup>, respectively. Among these peaks, the strong diffraction one at low angles (003) and (006) planes are belonging to the layer structure of hydrotalcite phase. As shown in the spectra of both GNH and NH, there are broad peaks around 20° to 26° which is assigned to amorphous form carbon from carbon clothes. There are no obvious peaks assigned to GQDs, because its crystallinity is low.<sup>140</sup> The data of XRD is clear that we have successfully synthesized GNH and NH.

XPS measurements were carried out to analyse the chemical compositions of G-NH//CC composite. As shown in Fig.5.6a, the XPS survey spectrum of G10-NH//CC sample shows the presence of Ni, O, and C in the composite, while C peak was not observed for NH//CC. The content of carbon in G10-NH//CC composite is calculated to be 3.8% from the XPS spectrum. The deconvolution of C 1s spectrum in Fig.5.6b shows different oxygen containing carbon functional groups, including sp<sup>2</sup> C-C at

284.3 eV,  $sp^3$  C-C at 285.4 eV, C-O-C at 287.4 eV and C=O at 288.5 eV. These peaks clarify the presence of GQDs in the composite sample. The deconvolution of Ni 2p spectrum of G10-NH//CC in Fig.5.6c can be assigned to two major peaks with satellite peaks of Ni 2p<sub>3/2</sub> (850 ~ 865 eV) and Ni 2p<sub>1/2</sub> (870 ~ 885 eV) spin-orbit levels, which shows Ni ion is in +2 valence state. The observed spin energy separation between Ni 2p<sub>3/2</sub> and Ni 2p<sub>1/2</sub> peaks are 17.6 eV, indicating characteristics of Ni(OH)<sub>2</sub> phase, and in accordance with previous reports.

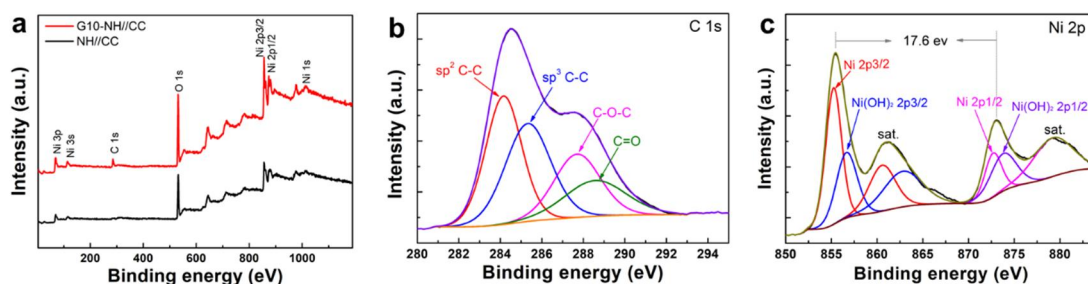


**Figure 5.6** (a) The XPS survey scan of G10-NH//CC and NH//CC. (b) High resolution C 1s and (c) Ni 2p XPS spectrum of G10-NH//CC.

### 5.3 Three electrodes system

The electrochemical performance of the obtained samples was investigated by a three-electrode system. The capacitive behaviors of the samples were measured by cyclic voltammetry (CV) at a scan rate of 20 mV s<sup>-1</sup> (Fig.5.7a). Two clear anodic and cathodic peaks are observed for all samples in the CV curves, indicating the pseudocapacitive behavior of Ni(OH)<sub>2</sub>-based electrode. This result indicates that the capacitance characteristics are mainly ascribed to the Faradic reactions. The current output in the CV curves shows that G-NH//CC composites are obviously higher than that of NH//CC at the same scan rate, indicating higher capacitance. This could be ascribed to the enhanced ion transport and electrical conductivity owing to the addition of GQDs. The calculated specific capacitance at 20 mV·s<sup>-1</sup> reveals that the G10-NH//CC composite shows superior performance of 1089 F·g<sup>-1</sup> compared to other samples (NH//CC=545 F·g<sup>-1</sup>, G5-NH//CC=753 F·g<sup>-1</sup>, and G15-NH//CC= 894 F·g<sup>-1</sup>).

Fig.5.7b shows the CV curves of the G10-NH//CC composite at different scan rates. It is shown that the current density simultaneously increases with the increasing scan rate, and the CV curves with symmetric redox peaks demonstrate a high reversibility of the charge-discharge reaction. In addition, the potentials of the anodic and cathodic peaks shift to more positive and negative potentials with the increasing scan rate, respectively, which is attributed to the polarization effect and ion diffusion.

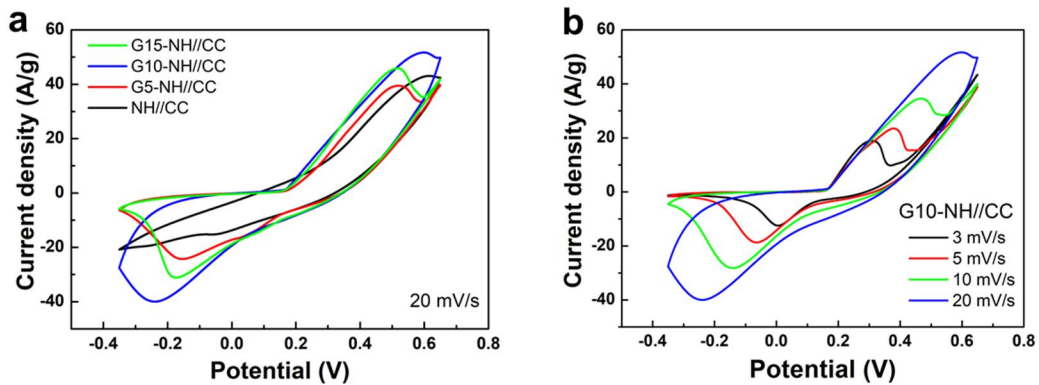


**Figure 5.7** (a) CV curves of different G-NH//CC composites and NH//CC. (b) CV curves of G10-NH//CC at different scan rates.

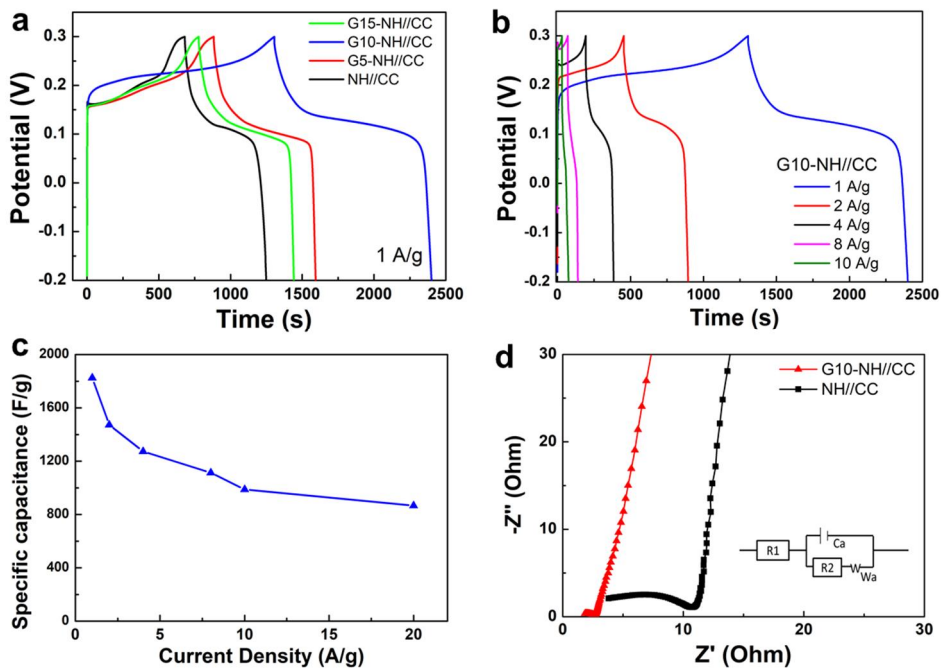


**Figure 5.8** (a) Galvanostatic charge-discharge curves of different G-NH//CC composites and NH//CC, (b) galvanostatic charge-discharge curves of G10-NH//CC at

different current densities. (c) Obtained specific capacitance of G10-NH//CC at different current densities. (d) Nyquist plots of G10-NH//CC and NH//CC.

The galvanostatic charge-discharge curves of the prepared samples were measured under voltage ranging from -0.2 to 0.3 V at a current density of  $1 \text{ A}\cdot\text{g}^{-1}$ . The charge-discharge curves in Fig.5.8a demonstrate that the area of the curves and the discharging time increase with the addition of GQDs, showing the specific capacitance is significantly enhanced due to GQDs. G10-NH//CC composite exhibits best charge-discharge performance among the prepared electrodes, which is optimal GQDs content. Also, the galvanostatic charge-discharge measurement of the G10-NH//CC composite was performed at a different current density from  $1 \text{ A}\cdot\text{g}^{-1}$  to  $10 \text{ A}\cdot\text{g}^{-1}$  (Fig.5.8b). A distinct potential plateau is observed in the charge and discharge curves, and it almost disappears at the current density of  $10 \text{ A}\cdot\text{g}^{-1}$ , showing the pseudocapacitive characteristics of  $\text{Ni}(\text{OH})_2$ -based electrode. It can be seen from Fig.5.8c that the obtained specific capacitance values decrease as the current density increases, which is due to the incremental voltage drop and an insufficient active material involved in the redox reaction at high current density. It also demonstrates that the supercapacitor performance of G10-NH//CC composite electrode among the prepared electrodes is superior to that of NH//CC electrode and due to the incorporation of GQDs (Fig.5.9). The calculated specific capacitances of G10-NH//CC are 1825, 1472, 1273, 1113, 988, and  $867 \text{ F}\cdot\text{g}^{-1}$  at current densities of 1, 2, 4, 8, 10, and  $20 \text{ A}\cdot\text{g}^{-1}$ , respectively. This capacitive performance of the binder free G10-NH//CC electrode is comparable to those of previously reported  $\text{Ni}(\text{OH})_2$  based-electrodes (Table 5.1). These high capacitance and good rate capability of G10-NH//CC composite suggest that it can be a promising electrode for supercapacitor applications. The electrochemical kinetics were further evaluated by the electrochemical impedance spectroscopy (EIS) measurements. Fig.5.8d show the Nyquist plots of G10-NH//CC and NH//CC electrodes composites with an equivalent circuit, where  $R_s$  represents the ionic resistance of the electrolyte solution, and  $R_{ct}$  is charge-transfer resistance at the contact interface between electrode and electrolyte. The plots of both electrodes are composed of a semicircle at the high

frequency region and a straight line at the low frequency region. The diameter of semicircle denotes the charge-transfer resistance ( $R_{ct}$ ), and the G10-NH//CC electrode exhibits a much lower  $R_{ct}$  value ( $1.66 \Omega$ ) than the NH//CC electrode ( $5.55 \Omega$ ), indicating that the GQDs enhance the electronic conductivity of electrode.

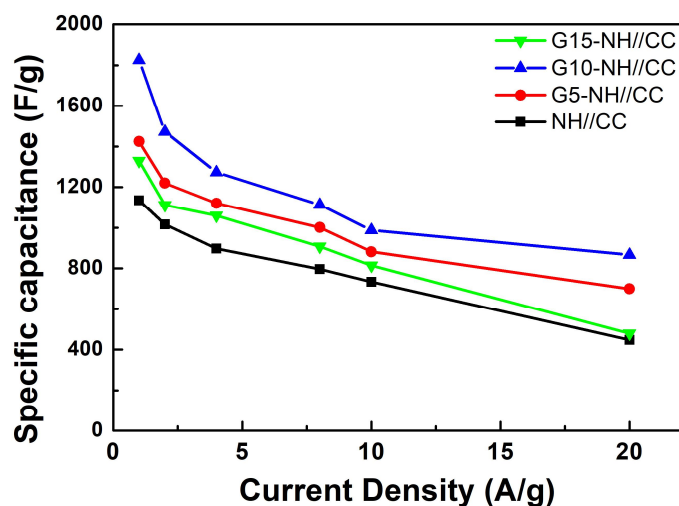


**Figure 5.9** Specific capacitance comparison of the prepared electrodes at different current densities.

The cycle stability of the G10-NH//CC electrode was further evaluated by the consecutive CV test up to 8000 cycles at a scan rate of  $50 \text{ mV} \cdot \text{s}^{-1}$ . As shown in Fig.5.10a, the specific capacitance increases about 10% during the first 200 cycles, which is due to the activation of the active materials through a slow diffusion of the electrolyte into nanostructure of G10-NH//CC electrode during the initial cycles. In particular, electrolyte has infiltrated into the nanostructured  $\text{Ni}(\text{OH})_2$  and the trapped  $\text{OH}^-$  ions gradually diffuse out, resulting in pseudocapacitive performance. It can be determined that 83.5% of the initial capacitance of G10-NH//CC electrode is retained after a successive 8000 cycles, however the NH//CC electrode retains only 55.2% of its initial capacitance, indicating the stable cycling performance of the G10-NH//CC electrode. The SEM images of G10-NH//CC electrodes after 2000 and 8000 cycles are shown in Fig.5.11. It reveals that G10-NH//CC electrode still maintains its initial microstructure without obvious structural change, which is responsible to the stable cycling performance. In addition, Nyquist plots after 2000 cycles (Fig.5.10b) show that  $R_{ct}$  of

the G10-NH//CC electrode increases slightly to 2.97  $\Omega$  and maintains its excellent charge transfer process after the cycle test, compared to the NH//CC electrode (10.01  $\Omega$ ).

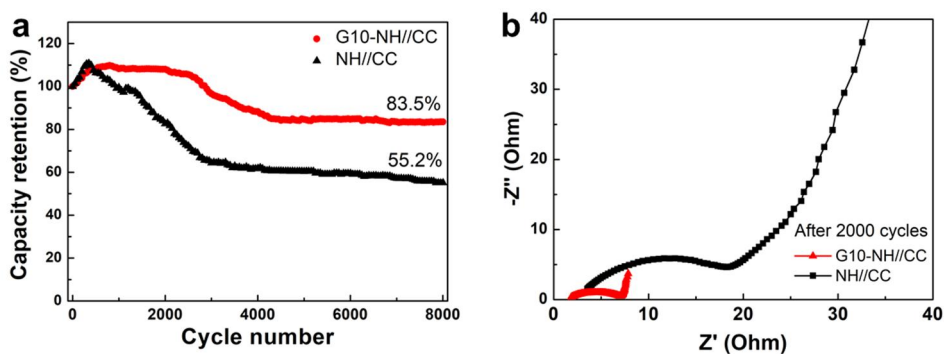


**Figure 5.10** (a) Specific capacitance retention of G10-NH//CC and NH//CC. (b) Nyquist plots of G10-NH//CC and NH//CC after 2000 cycles.

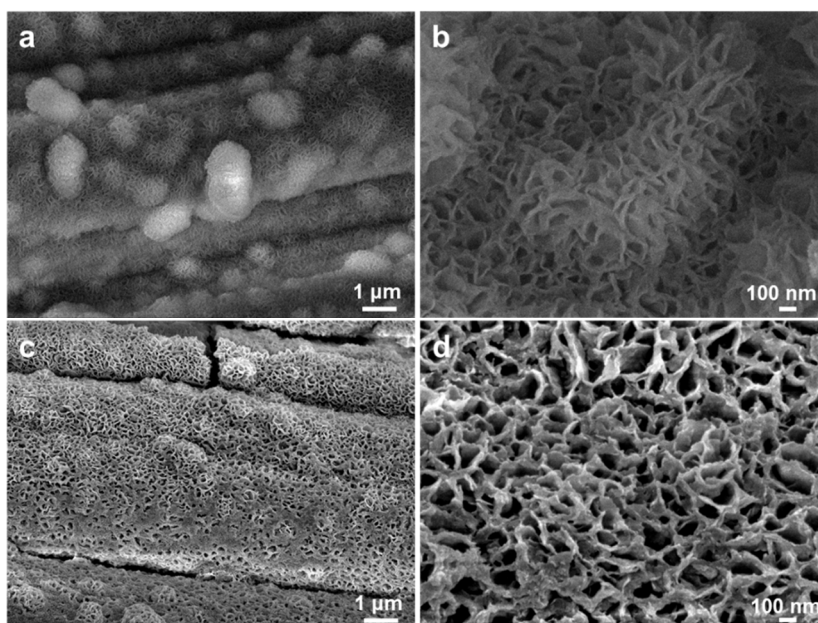


**Figure 5.11** SEM images of G10-NH//CC electrode after 2000 cycles (a-b) and 8000 cycles (c-d).

To understand the enhanced electrochemical performance by the incorporation of GQDs, the energy band structure of  $\text{Ni}(\text{OH})_2$  and GQDs was investigated, as shown in Fig.5.12. In the previous review, some group predicted that  $\beta$ - $\text{Ni}(\text{OH})_2$  is a semiconductor with a band gap around 2.9 eV and the work function is 3.7 eV. The

energy bandgap and work function of GQDs is related with their size by equation as following:

$$E_g = \frac{1.68}{L} \quad (5.4)$$

The size of GQDs in G-NH//CC is about 7 nm. Thus, the bandgap and work function of GQDs is 0.2 and 4.7 eV, respectively (Fig.5.12a). When Ni(OH)<sub>2</sub> contacts with GQDs, the free electrons will transfer from Ni(O)<sub>2</sub> to GQDs at the contact interface and the energy band of Ni(OH)<sub>2</sub> bends downward to align the Fermi levels (Fig.5.12b), due to higher work function of Ni(OH)<sub>2</sub> than GQDs. Therefore, GQDs/Ni(OH)<sub>2</sub> forms ohmic contact at the interface, and GQDs are negatively charged while Ni(OH)<sub>2</sub> is positively charged. This can facilitate the electrostatic attraction of GQDs with potassium ions of electrolytes as show in Fig.5.12b, resulting in enhancing specific capacitance. Moreover, the ohmic contact between GQDs and Ni(OH)<sub>2</sub> can improve the electrical conductivity of G-NH//CC electrode.

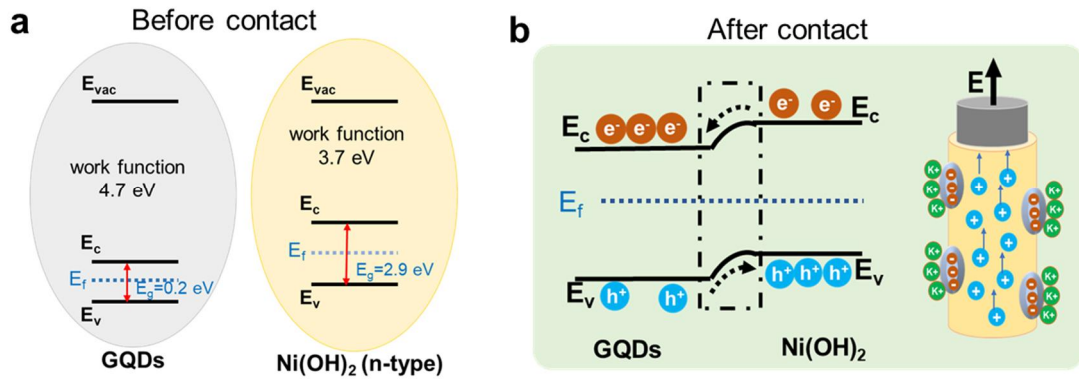


**Figure 5.12** Simplified energy band diagram of GQDs and Ni(OH)<sub>2</sub> (a) before contact and (b) after contact.

#### 5.4 Two electrodes system

To further evaluate the practical application of the G10-NH//CC electrode, an all-solid-state symmetric supercapacitor (SSC) was assembled. In symmetric device configuration, G10-NH//CC electrodes were used as both the cathode and anode with

poly(vinyl alcohol) (PVA)/KOH gel electrolyte and separator (Fig.5.13a). The photo images of Fig.5.13a show the bending state of the fabricated SSC, implying that the G10-NH//CC electrodes are highly flexible. The CV curves of the fabricated symmetric device at different scan rates were measured in the potential window of 0~1.54 V as shown in Fig.5.13b. The CV curves exhibit distorted quasi-rectangular shapes even at a high scan rate without distinct redox peaks, which indicates that the fabricated SSC using G10-NH//CC electrodes performs typical EDLC behaviour, suggesting the high-rate capability and low internal resistance. Furthermore, Fig.5.13c shows the galvanostatic charge-discharge curves of the fabricated SSC at different current densities from 0.5 to 4 A·g<sup>-1</sup>. The specific capacitances of SSC calculated from the curves are 90.9, 80.5, 62.3, and 36.4 F·g<sup>-1</sup> at current densities of 0.5, 1, 2 and 4 A·g<sup>-1</sup>, respectively. The energy density and power density of our SSC was compared with other Ni-based symmetric supercapacitors in the Ragone plot (Fig.5.13d). The SSC using G10-NH//CC electrodes delivers an energy density of 80.8 and 32.2 Wh·kg<sup>-1</sup> at a power density of 2021 and 16632 W·kg<sup>-1</sup>, respectively, superior to the previously reported devices. To further investigate the flexibility of our SSC, the CV curves were measured under different bending angles at a scan rate of 200 mV·s<sup>-1</sup> (Fig.5.13e). It can be observed that the CV shapes were well maintained even at a bending angle of 180°, suggesting good flexibility and mechanical stability of our SSC. To demonstrate the practical application of G10-NH//CC SSC device, two SSC devices were assembled in series and powered a green light-emitting diode (LED) bulb as shown in Fig.5.13f.



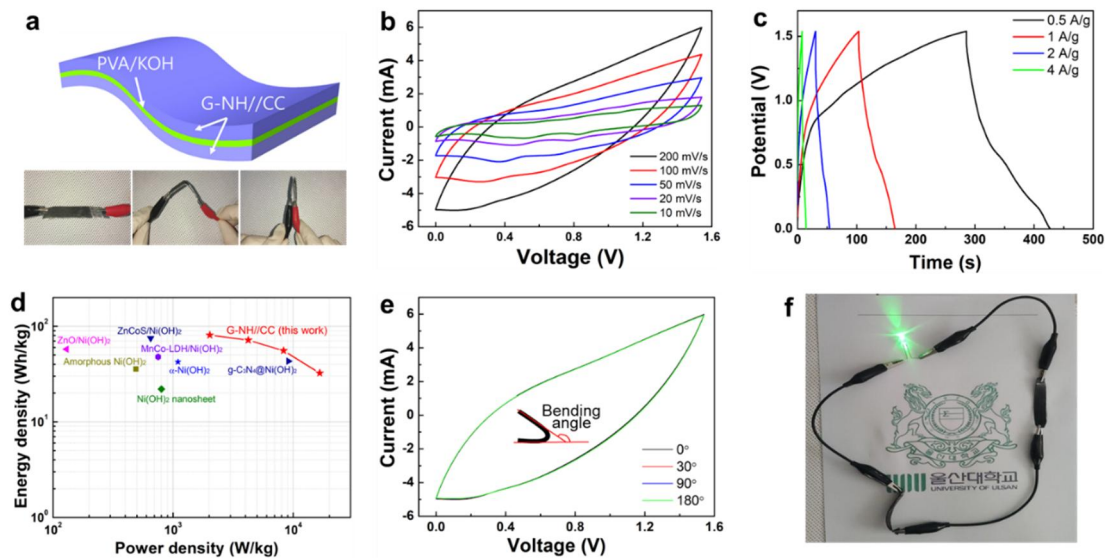


**Figure 5.13** (a) Schematic illustration of all-solid-state symmetric supercapacitor using G-NH//CC electrodes and photo images of the bending state. (b) CV curves at different scan rates and (c) galvanostatic charge-discharge curves at different current densities of the G-NH//CC SSC. (d) The Ragone plots of the G-NH//CC SSC and reported Ni(OH)<sub>2</sub>-based supercapacitors. (e) CV curves of the G-NH//CC SSC at different bending states. (f) Photo image of lighting LED bulb powered by two G-NH//CC SSCs in series.

## 5.5 Summary

All in all, a simple strategy was demonstrated to fabricate the GQDs/Ni(OH)<sub>2</sub> nanocomposite on flexible CC via the hydrothermal process. GQDs well embedded in Ni(OH)<sub>2</sub> nanowalls can enhance the overall electrical conductivity and ion diffusion, which result in the superior electrochemical performances. Therefore, the obtained G10-NH//CC electrode delivers an excellent specific capacitance of 1825 F·g<sup>-1</sup> at a current density of 1 A·g<sup>-1</sup> and a good cycle stability of 83.5% capacity retention after 8000 cycles. Moreover, the symmetric supercapacitor using G10-NH//CC electrodes performs a high energy density of 80.8 Wh·kg<sup>-1</sup> at a power density of 2021 W·kg<sup>-1</sup> with good flexibility. These results suggest that this novel strategy for fabricating various GQDs/metal oxide or GQDs/metal hydroxide provides great potential for advanced electrochemical energy storage devices.



## Chapter 6: Boron doped g-C<sub>3</sub>N<sub>4</sub> quantum dots/ Ni(OH)<sub>2</sub> nanocomposites on

### Nickel Foam for Supercapacitors

#### 6.1 Introduction

Among carbon materials (C-materials) as Ni(OH)<sub>2</sub> compositing components, 2-dimension(2D) C-materials appear on the horizon because of their large surface area, open van der Waals gaps and high mechanical strength (for instance, graphene and Mxene). Graphite carbon nitride (g-C<sub>3</sub>N<sub>4</sub>), similar with graphene, is one of 2D nanostructure materials with great chemical and thermodynamic stability. Because of its narrow band gap (2.7 eV), g-C<sub>3</sub>N<sub>4</sub> was already used as supercapacitor electrode material. Meanwhile compared with other 2D C-materials, g-C<sub>3</sub>N<sub>4</sub> is environment friendliness, low cost and simple preparation. And also, the lone pair of electrons present in the nitrogen atom from g-C<sub>3</sub>N<sub>4</sub> will improve the charge carrier mobility and wettability which is propitious to electrochemical properties, especially in the supercapacitor. However, because of its low surface area and low electronic conductivity, g-C<sub>3</sub>N<sub>4</sub> is restricted in the widely electrochemical application. In order to overcome this, composite g-C<sub>3</sub>N<sub>4</sub> with other conductive materials emerged. There is a scanty few of work discussing about boron-doped g-C<sub>3</sub>N<sub>4</sub> quantum dots (B-CNQDs) used as the electrode of supercapacitor. Previous studies show that B-CNQDs in photocatalyst application can not only improve the electrochemical properties due to the large contact area with electrolyte by quantum dots shape, but also enhance the charge storage and transfer within the doped C<sub>3</sub>N<sub>4</sub> structure, because boron atoms in the C<sub>3</sub>N<sub>4</sub> lattice shift the Fermi level toward the valence band.

In this chapter, we successfully synthesized n-type semiconductor of B-CNQDs and further composite it with p-type semiconductor of Ni(OH)<sub>2</sub> nanoflowers by impregnation method. These two materials assembled through electrostatics force and formed a p-n heterojunction. The structure of B-CNQDs and B-CNQDs modified

Ni(OH)<sub>2</sub> nanocomposites (B-CNQD<sub>x</sub>-Ni) were systematically checked by optical spectrum and electron microscope. After that, the composites were further used as a supercapacitor electrode, and their electrochemical properties were checked by electrochemical workstation, that exhibited outstanding cycling performance compared with the supercapacitor with bare Ni(OH)<sub>2</sub> as electrode. The diagram illustration for the synthesis of B-CNQD<sub>x</sub>-Ni nanoflowers has been shown in Fig.6.1.

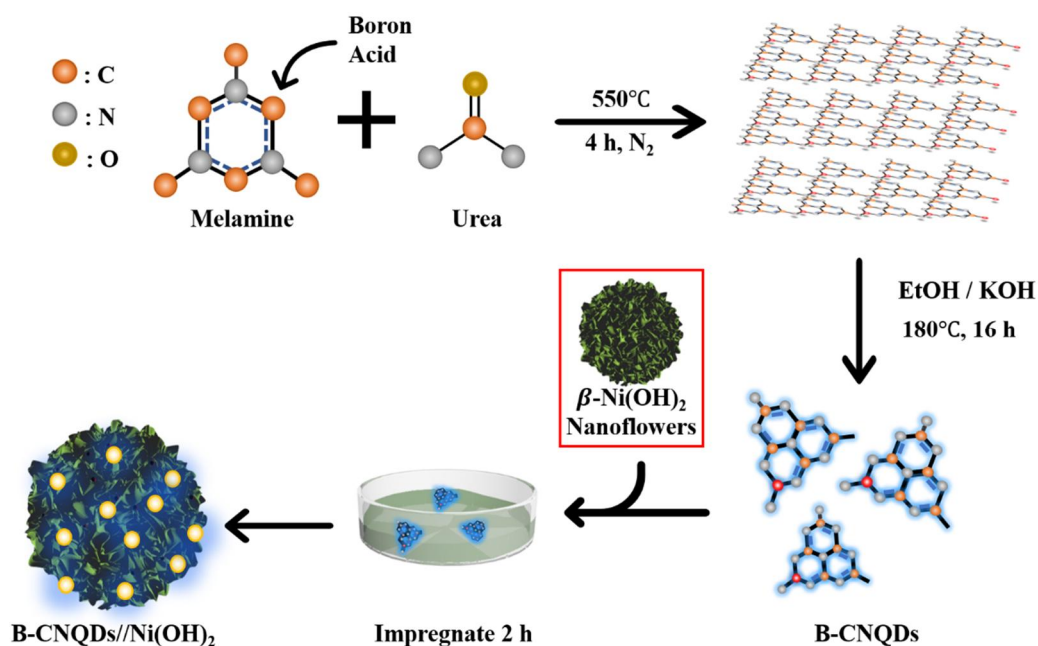


**Figure 6.1** Diagram illustration for the synthesis of B-CNQD<sub>x</sub>-Ni nanoflowers.

## 6.2 Morphologies and Structures

From XRD pattern (Fig.6.2a), both g-C<sub>3</sub>N<sub>4</sub> and B-C<sub>3</sub>N<sub>4</sub> have two core peaks at 13.2° and 26.6°, corresponding with (100) and (002) crystal planes, respectively (JCPDS 87-1526). One peak at 13.2° represents the in-planar repeating tri-s-triazine unit, and the other stronger peak at 26.6° signifies the layered stacking. The peak (100) of B-C<sub>3</sub>N<sub>4</sub> is weaker than that of g-C<sub>3</sub>N<sub>4</sub> because of reduced layers packing and boron atoms doping. By Scherrer's formula calculation based on (002) peaks, the crystal size of g-C<sub>3</sub>N<sub>4</sub> became smaller after being doped with boron atoms, and the values were 2.7 nm for g-C<sub>3</sub>N<sub>4</sub> and 2.2 nm for B-C<sub>3</sub>N<sub>4</sub>. The XRD patterns of Ni(OH)<sub>2</sub> and B-CNQD<sub>x</sub>-Ni are shown in Fig.6.3, and only Ni(OH)<sub>2</sub> crystalline phases can be observed, whereas

the loading of B-CNQD<sub>x</sub> caused no obvious change, probably due to the small amount and low crystallinity of B-CNQD<sub>x</sub> phase compared with Ni(OH)<sub>2</sub>. The FT-IR spectra (Fig.6.2b) also illustrate the structural changes between g-C<sub>3</sub>N<sub>4</sub> and B-C<sub>3</sub>N<sub>4</sub>. The broad bands from 2900 cm<sup>-1</sup> to 3500 cm<sup>-1</sup> derived from stretching vibration of -NH and H<sub>2</sub>O adsorbed by hydroxyl. The peaks at 805 cm<sup>-1</sup> correspond to tri-s-triazine units. With B-atoms doping, the wide range of peaks between 1233-1637 cm<sup>-1</sup>, relevant to C-N & C=N bonds, have a slight reduction in intensity. This is due to the vibration of B-N overlaps with C-N at 1200 cm<sup>-1</sup>. For quantum dots, fluorescence emission spectra (Fig.6.2c) were used to check the structure change of CNQDs and B-CNQDs (1 mg·mL<sup>-1</sup> in DI water). When excited at 285 nm, the CNQDs exhibited an emission peak at 345 nm. After B-atoms doped (B-CNQDs), the emission peak has a red shift to 385 nm and the intensity has increased 2 times than that of CNQDs, which shows a blue color under UV light irradiation (Fig.6.2c inset). This change can be attributed to the interaction between empty p-orbital of B-atoms and a large π-conjugated system of CNQDs, and p-π conjugation can form after the adding of B atoms into the C/N scaffold, leading to an increased electron density on the HOMO.

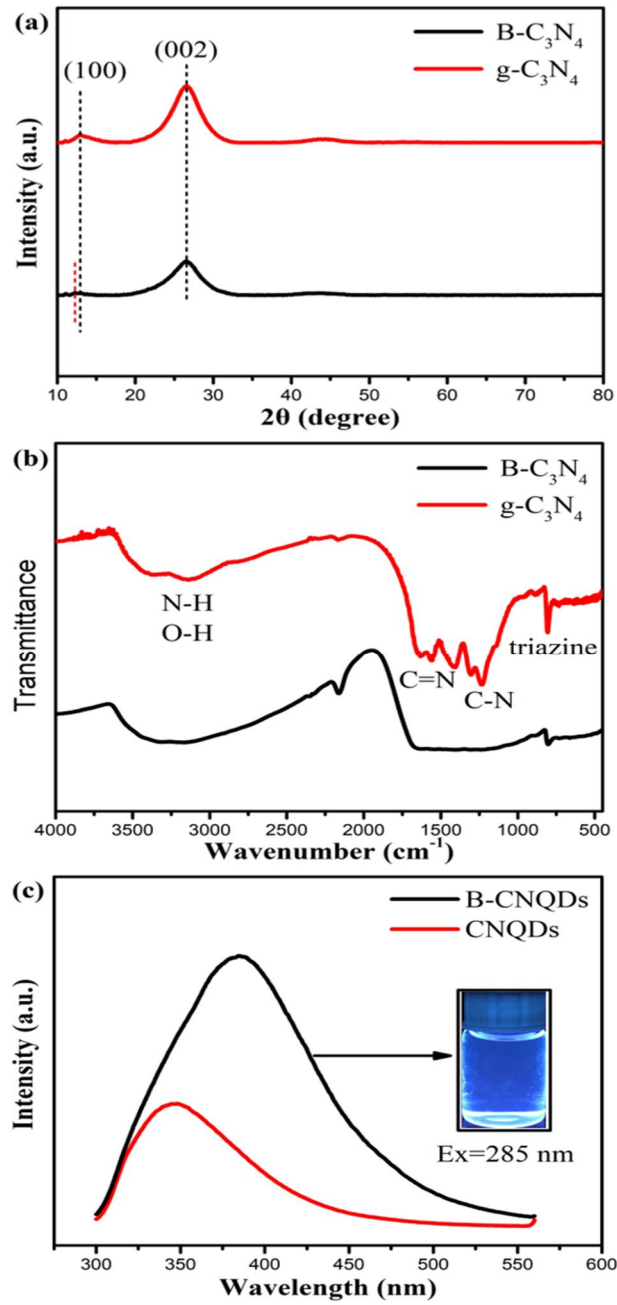


**Figure 6.2** (a) XRD pattern of B-C<sub>3</sub>N<sub>4</sub> and g- C<sub>3</sub>N<sub>4</sub>; (b) FT-IR pattern of B-C<sub>3</sub>N<sub>4</sub> and g- C<sub>3</sub>N<sub>4</sub>; (c) PL spectrum of B-CNQDs and CNQDs.

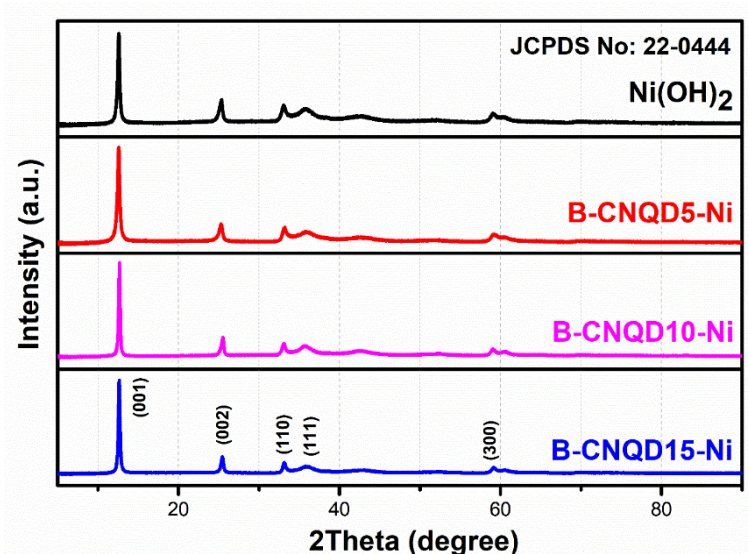


**Figure 6.3** XRD pattern of Ni(OH)<sub>2</sub> and B-CNQD<sub>x</sub>-Ni.

The morphology and microstructure of B-CNQD10-Ni nanocomposites are observed by the SEM and TEM in Fig.6.4. Ni(OH)<sub>2</sub> sample (Fig.6.4a) is like blooming flowers with the wall smaller than 20 nm, and the surface of flakes, which make up flowers, are almost smooth. After compositing with B-CNQDs (Fig.6.4b), the morphology of Ni(OH)<sub>2</sub> doesn't change obviously. The nanoflowers structure provides more access to the ions in electrolyte than bulk materials, which can promote the electrochemical performance and provide fast electrons pathway. More-over, the TEM and HRTEM of B-CNQD10-Ni shown in Fig.6.4(c-d) reveal B-CNQDs have an average size of 1.5 nm, which have successfully covered on the surface of Ni(OH)<sub>2</sub>. The zeta potential power spectra shown in Fig.6.5 have certified two materials composites by electro-static force. It is determined that Ni(OH)<sub>2</sub> and B-CNQDs exhibited zeta potentials of 5.11 and -25 mV, respectively. There may be some re-stacking B-CNQDs during the storage, resulting in two peaks in zeta potential plots after five day. Results of specific surface area (SSA) from BET method indicated that B-CNQDs had magnified SSA of the composite (best SSA of B-CNQD10-Ni:18.32 m<sup>2</sup>/g) compared with the value of bare Ni(OH)<sub>2</sub> ( 8.84 m<sup>2</sup>/g) (Fig.6.6). Both samples are mesoporous materials with type IV isotherm. The larger SSA of composite indicates that B-CNQD10-Ni has a larger contact surface with electrolyte that will enhance the capacitor's ability to store charge.

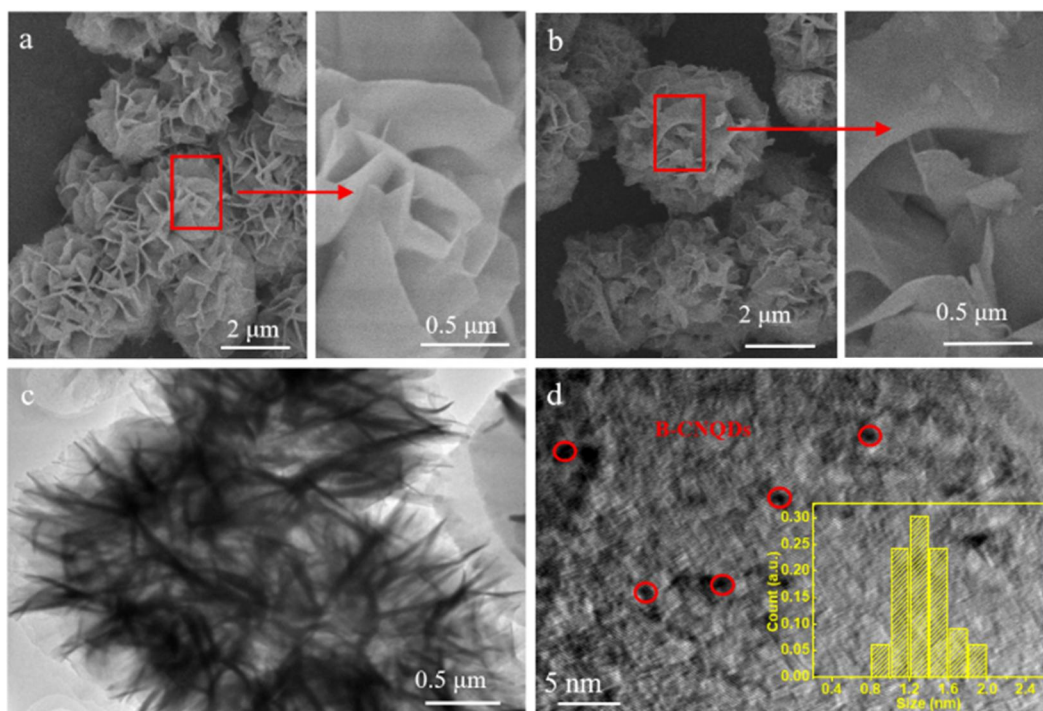


**Figure 6.4** (a) SEM images of  $\text{Ni}(\text{OH})_2$  nanoflowers, (b) SEM images of B-CNQD10-Ni nanocomposites, (c) TEM and (d) HRTEM images of B-CNQD10-Ni nanocomposites.

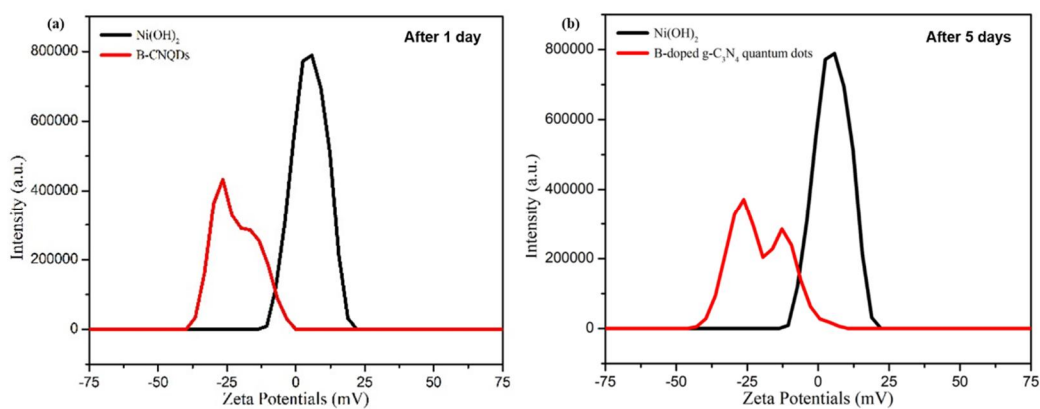


**Figure 6.5** Zeta Potential Power spectra obtained from B-doped  $\text{g-C}_3\text{N}_4$  quantum dots and  $\text{Ni}(\text{OH})_2$  (a) standing after 1 day, (b) standing after 5 days.



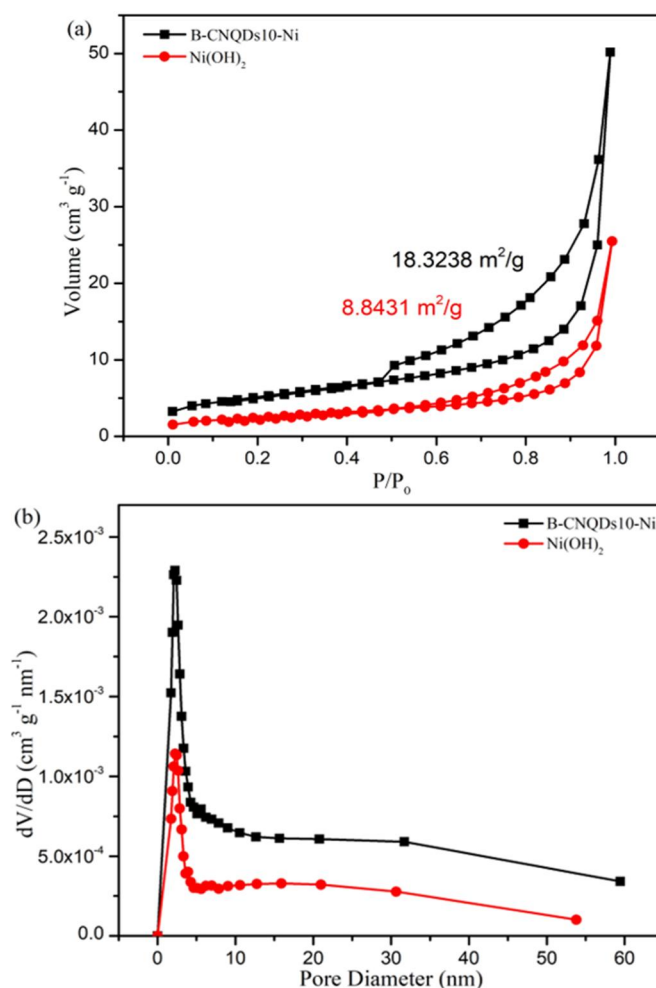


**Figure 6.6** (a) BET-N<sub>2</sub> adsorption/desorption isotherm and (b) Poresize distribution of B-CNQD10-Ni and Ni(OH)<sub>2</sub>.

The chemical nature of the synthesized B-CNQD10-Ni is studied by XPS (Fig.6.7). From the full scan XPS spectra (Fig.6.7a), Ni, O, C, N and B elements can be observed in the B-CNQD<sub>x</sub>-Ni composite, whereas B and N are missing in pure Ni(OH)<sub>2</sub>. Based on the XPS quantitative analysis, the atomic percentages of C, B, Ni, N and O in B-CNQD10-Ni are 17.48, 1.47, 50.3, 7.26 and 23.49%. In Ni 2p region (Fig.6.7b), the peaks of Ni 2p<sub>3/2</sub> from B-CNQD10-Ni are deconvoluted by two peaks at 855.28 eV, and satellite peak at 861.28 eV. Meanwhile, the peaks of Ni 2p<sub>1/2</sub> are also deconvoluted by peaks at 872.88 eV and the satellite peak at 879.18 eV. The spin energy separation of 17.6 eV has appeared between the two major Ni 2p peaks which confirmed the Ni(OH)<sub>2</sub> phase. For B1s region (Fig.6.7c), the main peak is at 192.0 eV, corresponding

to the characteristic peak for C-NB. The C 1s state (Fig.6.7d) has four signals at 284.6, 287.1, 288.9 and 291 eV, which are owing to the carbon components as following: graphitic carbon, N-C-N, N-C=N and shakeup satellite of the peak  $\pi-\pi^*$ . The survey spectrums of B-C<sub>3</sub>N<sub>4</sub> and g-C<sub>3</sub>N<sub>4</sub> are shown in Fig.6.8.

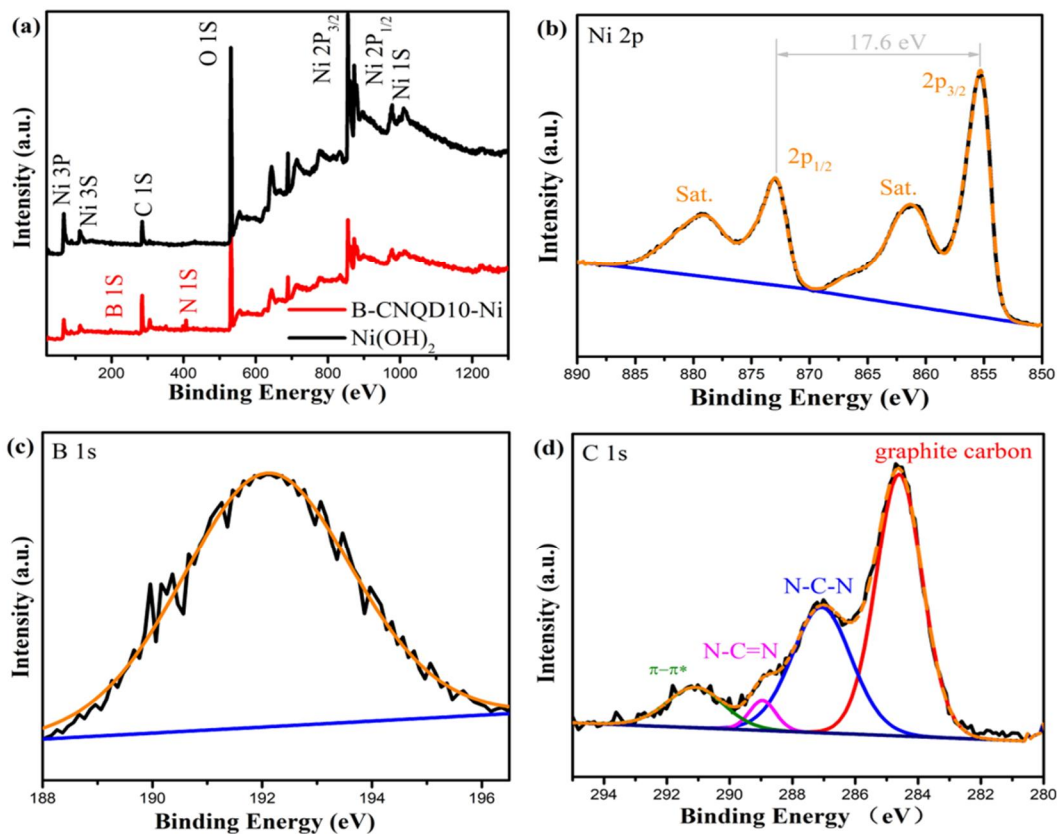


**Figure 6.7** (a) The XPS survey scan of B-CNQD10-Ni and Ni(OH)<sub>2</sub>. (b) High resolution Ni 1s, (c) B 1s and (d) C 1s XPS spectrum of B-CNQD10-Ni.

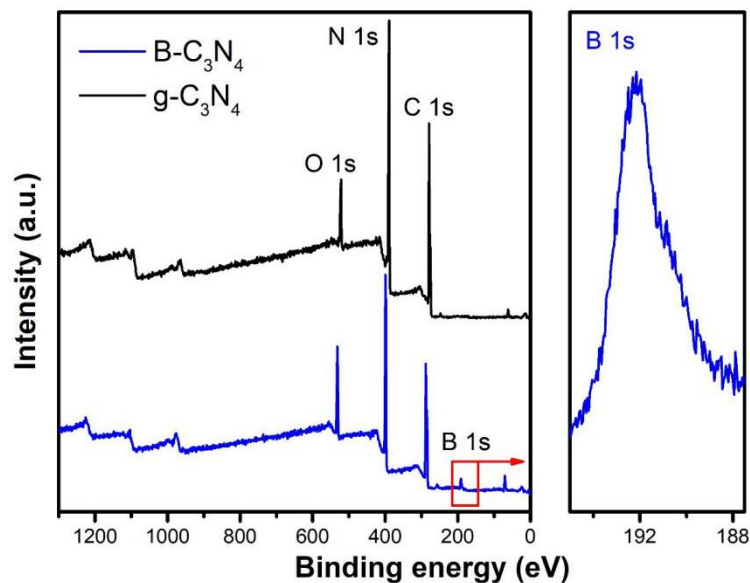


**Figure 6.8** The XPS survey scan of B-C<sub>3</sub>N<sub>4</sub> and g-C<sub>3</sub>N<sub>4</sub>.

UV-Vis spectra were used to characterize the B-CNQD10-Ni and Ni(OH)<sub>2</sub> nanoflowers (Fig.6.9). Both samples have a similar absorption band, appearing at 390 and 675 nm, assigning to the  $^3A_{2g}(F) \rightarrow ^3T_{1g}(P)$  and  $^3A_{2g}(F) \rightarrow ^3T_{1g}(F)$ , respectively. Kubelka-Munk plot is used to calculate the bandgap energy, which was 3.4 eV for composited sample (B-CNQD10-Ni) and 3.77 eV for Ni(OH)<sub>2</sub>. The smaller bandgap of B-CNQD10-Ni was due to the extremely small size of B-C<sub>3</sub>N<sub>4</sub> quantum dots, and those quantized B-CNQDs need lower energy to make electron transition. Thus, B-CNQD10-Ni has lower charge transfer resistance which may be good for transition metal oxides based pseudocapacitor.

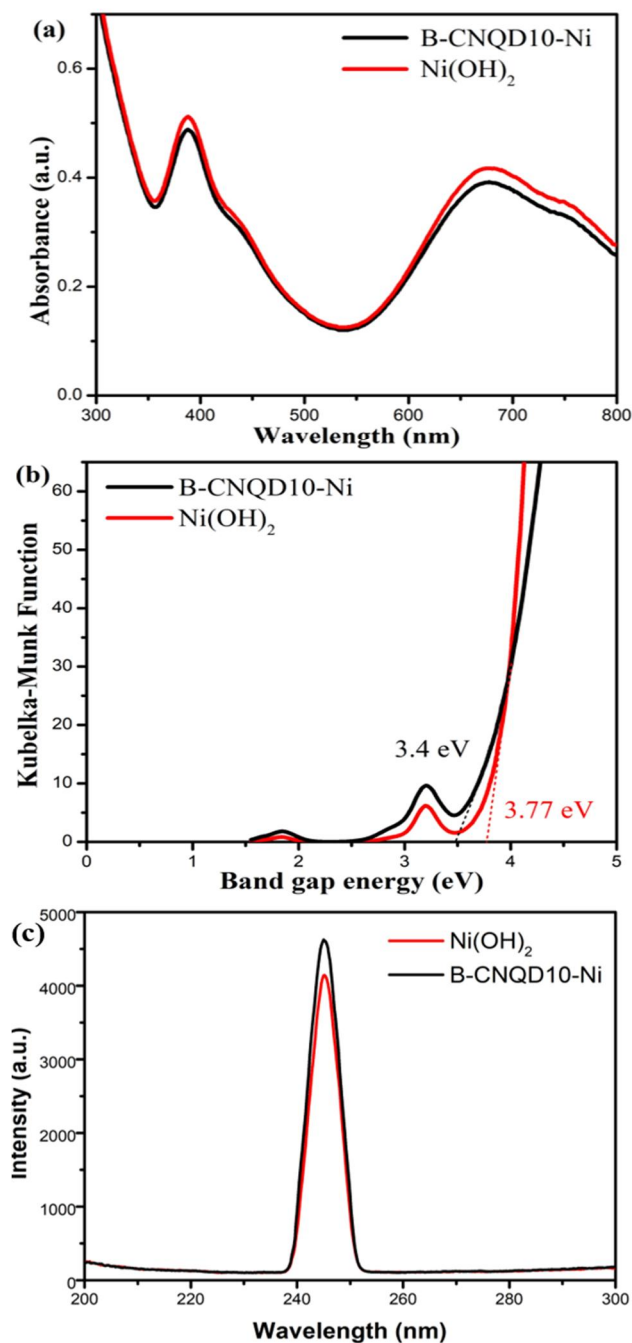


**Figure 6.9** UV-Vis diffuse reflectance spectra (a) and Kubelka-Munk plot (b) for estimating bandgap energy of Ni(OH)<sub>2</sub> and B-CNQD10-Ni. (c) PL emission spectra of pure Ni(OH)<sub>2</sub> and B-CNQD10-Ni.

Based on the characterizations and the literature reported properties of B-CNQDs (n-type semiconductor) and Ni(OH)<sub>2</sub> (p-type semiconductor), a diagram is used to indicate the charge transfer between B-CNQDx-Ni composites (Fig.6.10). After B-

CNQDs composited on the surface of Ni(OH)<sub>2</sub> nanoflower, a p-n heterojunction appears and partially bending occurs on the energy band of B-CNQDs and Ni(OH)<sub>2</sub> due to the positions of valance band(VB) and conductive band(CB) and also the related band gap. Thus, electrons(e<sup>-</sup>) transfers from CB<sub>Ni(OH)<sub>2</sub></sub> to CB<sub>B-CNQDs</sub>, while the holes(h<sup>+</sup>) shift from VB<sub>B-CNQDs</sub> to VB<sub>Ni(OH)<sub>2</sub></sub>. The formation of p-n hetero-junction between Ni(OH)<sub>2</sub> and B-CNQDs can accelerate charge transfer and format space-charge region, which is benefit to the following electrochemical performance when used as an electrode in supercapacitors. PL emission (as shown in Fig.6.9c) is used to explore the re-combination of photogenerated charge carriers. The B-CNQD10-Ni under 490 nm excitation exhibits a peak at 245 nm, which has a higher emission intensity than that of pure Ni(OH)<sub>2</sub>, indicating more charge carriers are produced for B-CNQDs/Ni(OH)<sub>2</sub> composite.

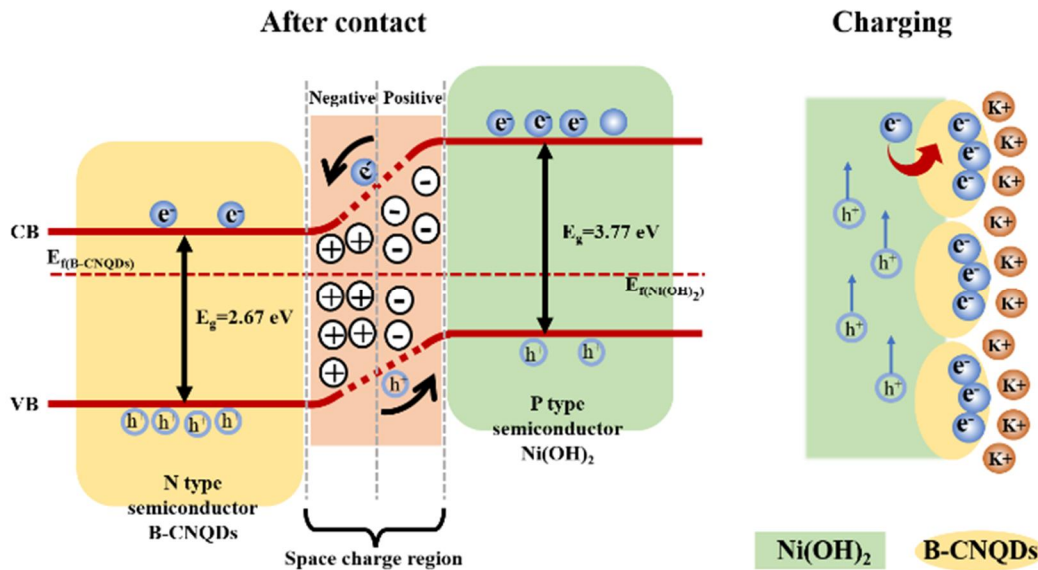
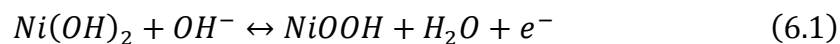


**Figure 6.10** Sketch of charge transfer between B-CNQDs and Ni(OH)<sub>2</sub>.

### 6.3 Electrochemical Performance

The electrochemical performances of Ni(OH)<sub>2</sub> and B-CNQD<sub>x</sub>-Ni nanocomposites are investigated by CV (Fig.6.11(a-c)). The CV curves exhibit two strong redox peaks in KOH (2M) electrolyte, which is normally from surface faradic redox reactions. For our B-CNQD<sub>x</sub>-Ni electrode materials, the surface faradaic reactions will proceed as:



In Fig.6.11(a-b), the CV curves of B-CNQD10-Ni and Ni(OH)<sub>2</sub> at different scan rate (5-200 mv·s<sup>-1</sup> between 0-0.6 V) have been demonstrated. Based on the CV curves with different scan rate (Fig.6.11a), the capacitances of B-CNQD10-Ni are 1433.3, 1009, 785, 532 and 432.4 F·g<sup>-1</sup> at scan rates of 10, 20, 50, 100 and 200 mV·s<sup>-1</sup>, respectively. The values are obviously higher than those of other samples at the same scan rate (Fig.6.11c). Different with CV curves of bare Ni(OH)<sub>2</sub> (Fig.6.11b), the redox peaks of B-CNQD10-Ni have no obvious moving along with the increasing of scan rate, indicating B-CNQD10-Ni has high-rate discharge performance and perfectly reversible redox reaction. The Nyquist plots with the frequency range from 0.01 to 1×10<sup>5</sup> Hz of Ni(OH)<sub>2</sub> and B-CNQDx-Ni nanocomposites electrodes are shown in Fig.6.11d. At the high-frequency region (inset in Fig.6.11d), all the sample have a small semicircle, which represents both the relationship between electrodes and the charge transfer impedance referring to Faraday's reaction and the resistance of the electrolyte. At the low-frequency region, there is a straight linear part that due to the Warburg impedance from ions in electrodes, which also named diffusion impedance. By fitting with circuit diagram in the inset, B-CNQD10-Ni demonstrates the smallest internal resistance of 7.421 Ω smaller than the resistance of other samples ((Ni(OH)<sub>2</sub>: 16.74 Ω, B-CNQD5-Ni: 10.86 Ω, B-CNQD15-Ni: 8.135 Ω).

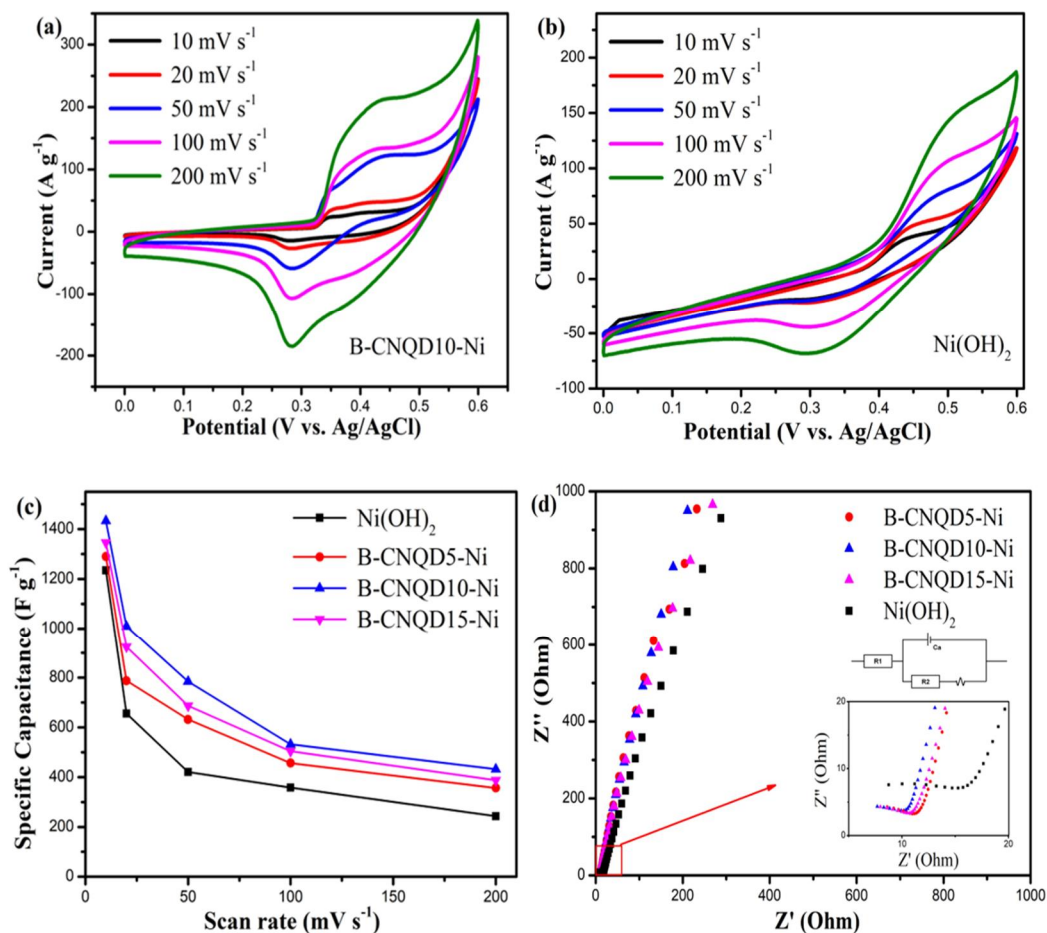


**Figure 6.11** CV curves of (a) B-CNQD10-Ni and (b) Ni(OH)<sub>2</sub> at a scan rate of 10-200 mV·s<sup>-1</sup>; (c) Capacitances as a function of scan rate; (d) Nyquist plots and insets show the enlarged Nyquist plots at high to medium frequencies.

Fig.6.12a shows galvanostatic charging and discharge (GCD) curve of Ni(OH)<sub>2</sub>, B-CNQD5-Ni, B-CNQD10-Ni and B-CNQD15-Ni at 1.5 A·g<sup>-1</sup>, where B-CNQD10-Ni still have the highest specific capacitance of 1700 F·g<sup>-1</sup> with the voltage window of 0-0.6 V. Under the same condition, the specific capacitance of Ni(OH)<sub>2</sub>, B-CNQD5-Ni and B-CNQD15-Ni are 1432.5, 1660 and 1634 F·g<sup>-1</sup>, respectively. Similar to CV curves, GCD curves also have two steps which are corresponding to redox reaction potential. Moreover, Fig.6.12b shows B-CNQD10-Ni GCD curve at different current density, and the calculated capacitances are 1700, 1579, 1474 and 1280 F·g<sup>-1</sup> at 1.5, 3, 6, 12 A·g<sup>-1</sup> with voltage window from 0 to 0.6 V which is higher than bare Ni(OH)<sub>2</sub> (Fig.6.12c). The cycling stability of B-CNQDx-Ni is checked at 50 mV·s<sup>-1</sup> (Fig.6.12d). The

capacitance after 3000 cycles is about 83-93% of the initial capacitance for B-CNQD<sub>x</sub>-Ni (B-CNQD5-Ni: 83%; B-CNQD10-Ni: 93%; B-CNQD15-Ni: 86%), much better than the 48% retaining ratio of Ni(OH)<sub>2</sub> after 3000. The capacitance of the best B-CNQD10-Ni continuously increases during the first 200 cycles and then reduces slowly to 609.6 F·g<sup>-1</sup> at the 5000th cycle (82%). The beginning of increasing is because of the electrochemical activity of the active material. The higher stability of B-CNQD10-Ni during long cycles are due to the well-keeping structure of B-CNQD10-Ni (Fig.6.12e-h). Because B-CNQDs can restrain the volume expansion of Ni(OH)<sub>2</sub> during the charging/discharging process. Compared with the collapsed morphology of Ni(OH)<sub>2</sub> nanoflowers after 1000 cycles, B-CNQD10-Ni expresses a full nanoflowers, which efficiently prevents the capacitance decay of B-CNQD10-Ni. In brief, B-CNQDs plays a vital role in the supercapacitors. The B-CNQDs modification of Ni(OH)<sub>2</sub> can not only improve the ions diffusion and redox reactions rate, but also enhance the cycle stability due to the uniform and homogeneous distribution of B-CNQDs on Ni(OH)<sub>2</sub> surface. However, when the specific weight of B-CNQDs increase, the sacrifice of contact area between Ni(OH)<sub>2</sub> and electrolyte will happen that lead to a negative effect on electrode performance.



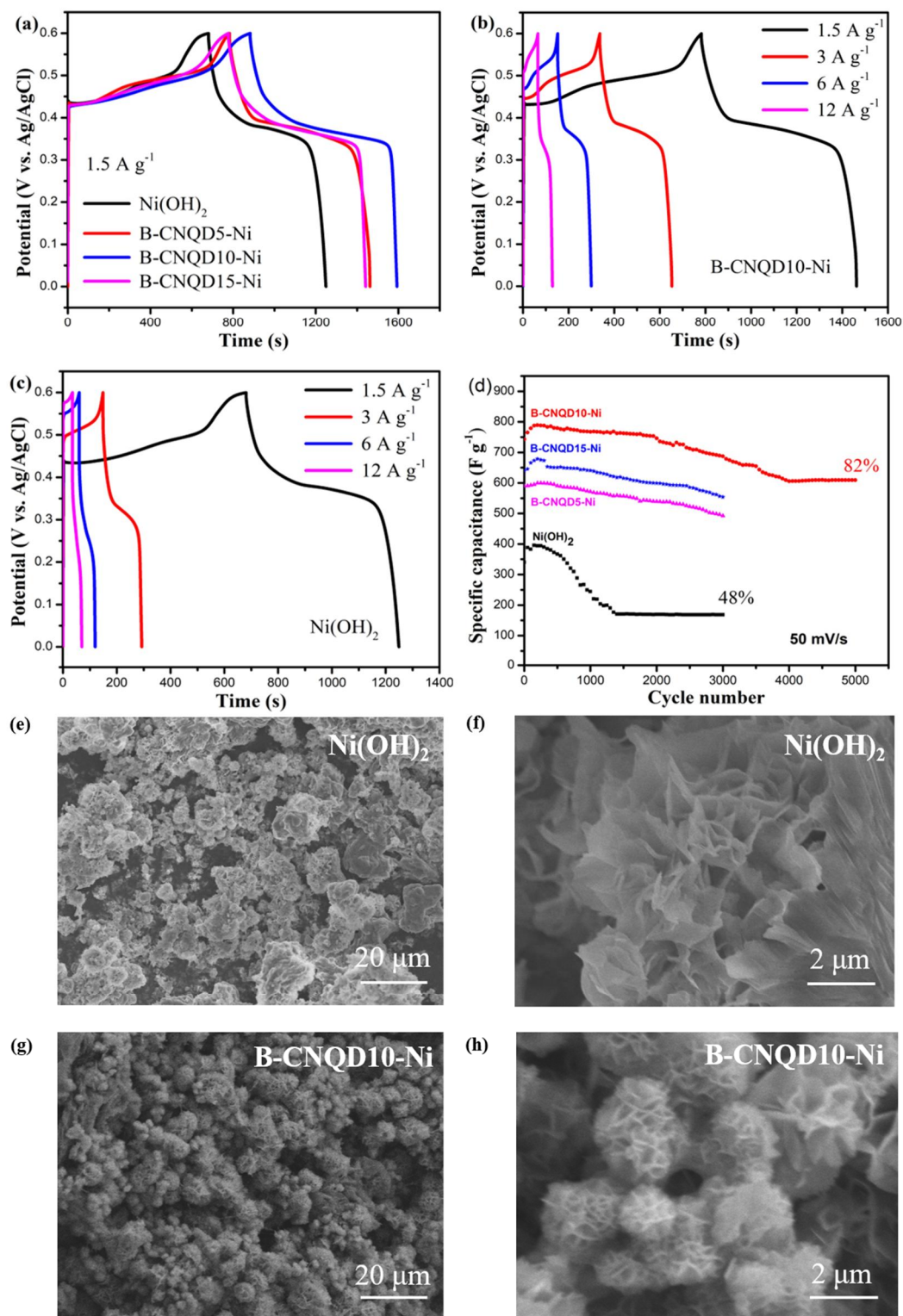


**Figure 6.12** (a) GCD curve of Ni(OH)<sub>2</sub> and B-CNQD<sub>x</sub>-Ni nanocomposites at 1.5 A·g<sup>-1</sup>; GCD curves of (b) B-CNQD10-Ni and (c) Ni(OH)<sub>2</sub> at different current densities of 1.5-12 A·g<sup>-1</sup>; (d) cycling specific capacitance retention of Ni(OH)<sub>2</sub> and B-CNQD<sub>x</sub>-Ni, (e-f) SEM images of Ni(OH)<sub>2</sub> after 1000 cycles in 1 M KOH, (g-h) SEM images of B-

CNQD10-Ni after 1000 cycles in 2 M KOH.

#### 6.4 Summary

Boron doping g-C<sub>3</sub>N<sub>4</sub> quantum dots (B-CNQDs) have been successfully synthesized, and further composited with Ni(OH)<sub>2</sub> nanoflowers by a mild impregnation method. B-CNQDs adsorbed on the surface of Ni(OH)<sub>2</sub> by electrostatic force and would not fall off even in the alkaline electrolyte. The modification of Ni(OH)<sub>2</sub> nanoflower by B-CNQDs creates a p-n heterojunction, which can not only reduce the bandgap energy of the composite, but also increase the contact surface area with electrolyte, resulting in a promoted electrochemical performance. In the composites with different ratio, B-CNQD10-Ni(OH)<sub>2</sub> displayed an excellent work in electrochemical performance with a specific capacitance of 1700 F·g<sup>-1</sup> at 1.5 A·g<sup>-1</sup>, low resistance of 7.421 Ω compared with Ni(OH)<sub>2</sub> (16.74 Ω) and great cycling performance even after 5000 cycles (82%).

## Chapter 7: Mxene quantum dots/ Ni(OH)<sub>2</sub> nanocomposites on Nickel Foam for

### Supercapacitors

#### 7.1 Introduction

A new type of 2D nanosheet materials (Mxene) has been synthesized by etching the “A” element (IIIA or IVA) from MAX phases in the field of energy storage. With super conductivity (2400 S/cm) and high surface area (98 m<sup>2</sup>/g), it has aroused great interest in its electrochemical performance. Different with other traditional 2D materials, Mxene owns the superior properties which can be candidates for energy storage as LIBs and SCs. The rich polar groups on the surfaces of Mxene, such as -OH, O and F, could provide strong chemical interactions for supercapacitors. Recently, Mxene (Ti<sub>2</sub>CT<sub>x</sub> or Ti<sub>3</sub>C<sub>2</sub>T<sub>x</sub>) with environmentally friendly property have been used as the electrode materials of SCs, resulting in dramatically improved cyclability and stability. On the other hand, Mxene quantum dots possess special physical and chemical properties due to their quantum confinement and edge effects which promotes the electronic infiltrate from electrolyte to electrode. Most importantly, the MXene-based composite is preferable for forming a closely-packed structure after alkaline electrolyte infiltration to acquire high volumetric capacity.

However, one of the disadvantages of QDs is that the self-aggregation will happen during charge/discharge cycles, its discrete distribution is not favorable for the electron transport. In this work, we synthesized Mxene quantum dots in different solvate (DMF, DMSO and ethanol) with microwave assistant. This gentle preparation method allowed the quantum dots to be uniformly dispersed in the solvent, which was conducive to the subsequent preparation of the composite. Subsequently, we used nickel foam as the skeleton and used a one-step method to make quantum dots and nickel hydroxide grow uniformly on it at the same time (as shown in Fig.7.1). These materials were named as e-M-NH/NF, f- M-NH/NF and o- M-NH/NF.

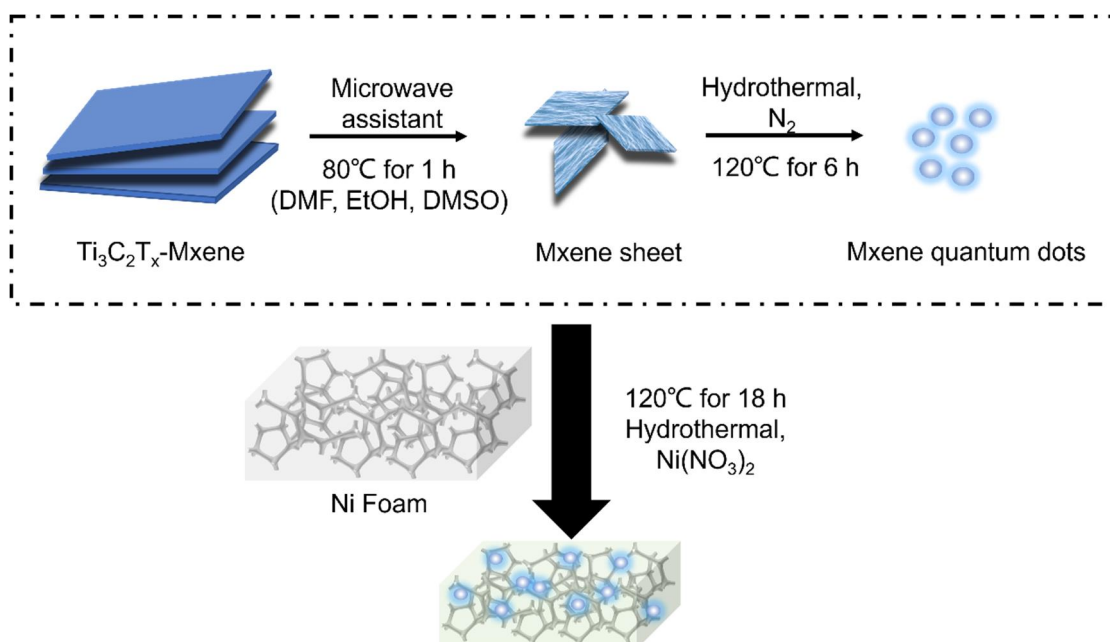


**Figure 7.1** Diagram illustration for the synthesis of M-NH/NF.

## 7.2 Morphologies and Structures

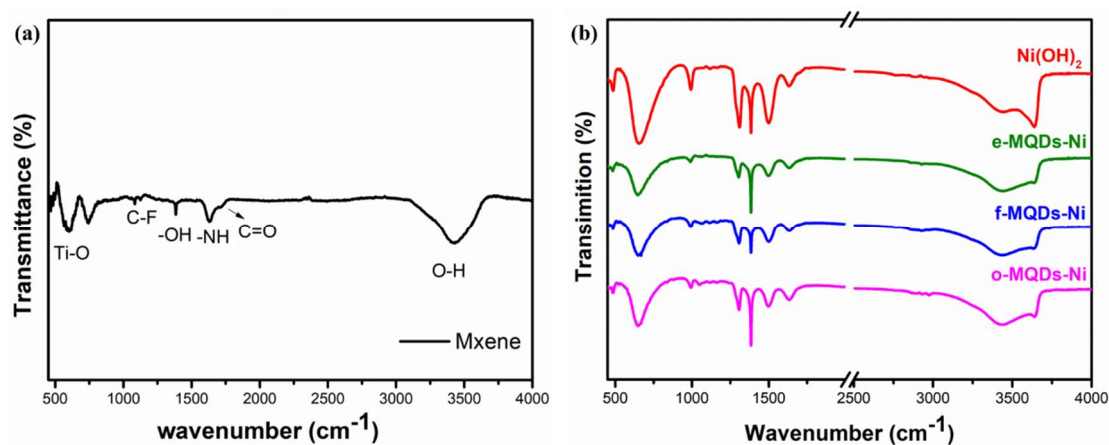


**Figure 7.2** FT-IR pattern of (a) Mxene and (b)  $\text{Ni}(\text{OH})_2$ , e-MQDs-Ni, f-MQDs-Ni and o- e-MQDs-Ni.

The FT-IR spectra (Fig.7.1) illustrate the structural changes between Mxene and bare  $\text{Ni}(\text{OH})_2$ , composite materials -MQDs-Ni, f-MQDs-Ni and o- e-MQDs-Ni. From, fig.7.1a, the broad bands from  $3000\text{ cm}^{-1}$  to  $3500\text{ cm}^{-1}$  derived from stretching vibration of O-H. The peaks at  $602\text{ cm}^{-1}$ ,  $1083\text{ cm}^{-1}$ ,  $1384\text{ cm}^{-1}$ ,  $1631\text{ cm}^{-1}$  correspond to Ti-O, C-F, -OH and NH, respectively. At the same time, there is a small peak very close to the NH peak from the carbon-oxygen double bond. As shown in fig 7.1b, compared

with bare Ni(OH)<sub>2</sub>, peaks at 660 cm<sup>-1</sup> from Ni-OH vibration, the peaks of other three composites materials have shift to 640 cm<sup>-1</sup> due to Ti-O vibration of Mxene effect.

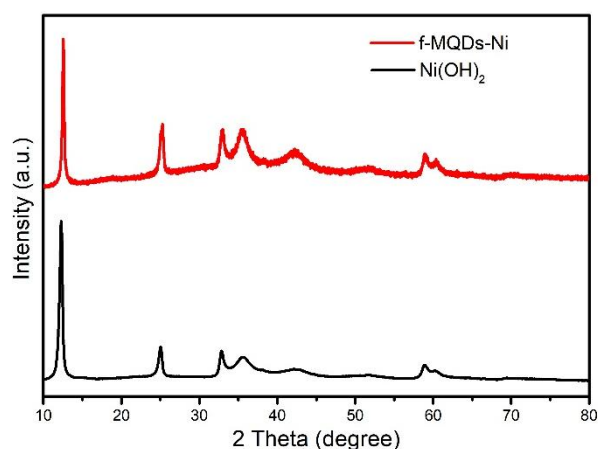


**Figure 7.3** XRD pattern of f-MQDs-Ni and Ni(OH)<sub>2</sub>.

XRD is another method used to characterize the crystal structure of materials. From XRD pattern (Fig.7.2), both of samples have the peaks from Ni(OH)<sub>2</sub>, that 12.5° of (001), 32° of (100) and 35° of (101). However, compared to composite materials, the number and position of peaks do not change much in Ni(OH)<sub>2</sub>. This is because the content of quantum dots is extremely small, and the peaks at some positions overlap with the peaks of nickel hydroxide.

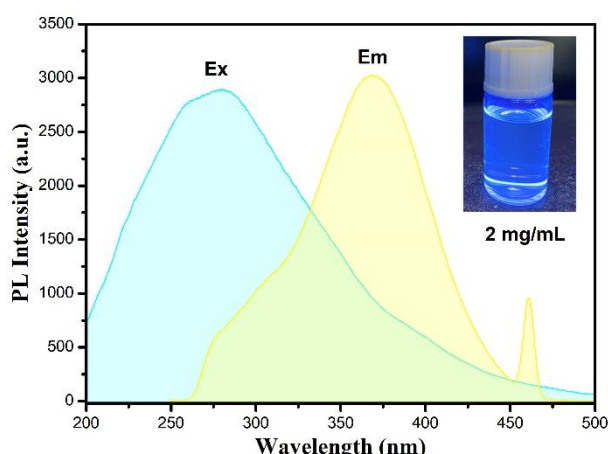


**Figure 7.4** The spectra of UV–vis absorption, maximum excitation (EX) and emission (EM) peaks of the as-prepared f-MQDs.

To investigate the optical properties of the MQDs in detail, UV–vis absorption and PL spectra were collected (Fig.7.3). From PL spectra, the f-MQDs showed the typical

peaks of the optimum excitation and emission wavelengths were 270 and 370 nm, respectively. In addition, the 2 mg/mL of f-MQDs emitted blue fluorescence upon irradiation with 365 nm UV lamp (inset figure).

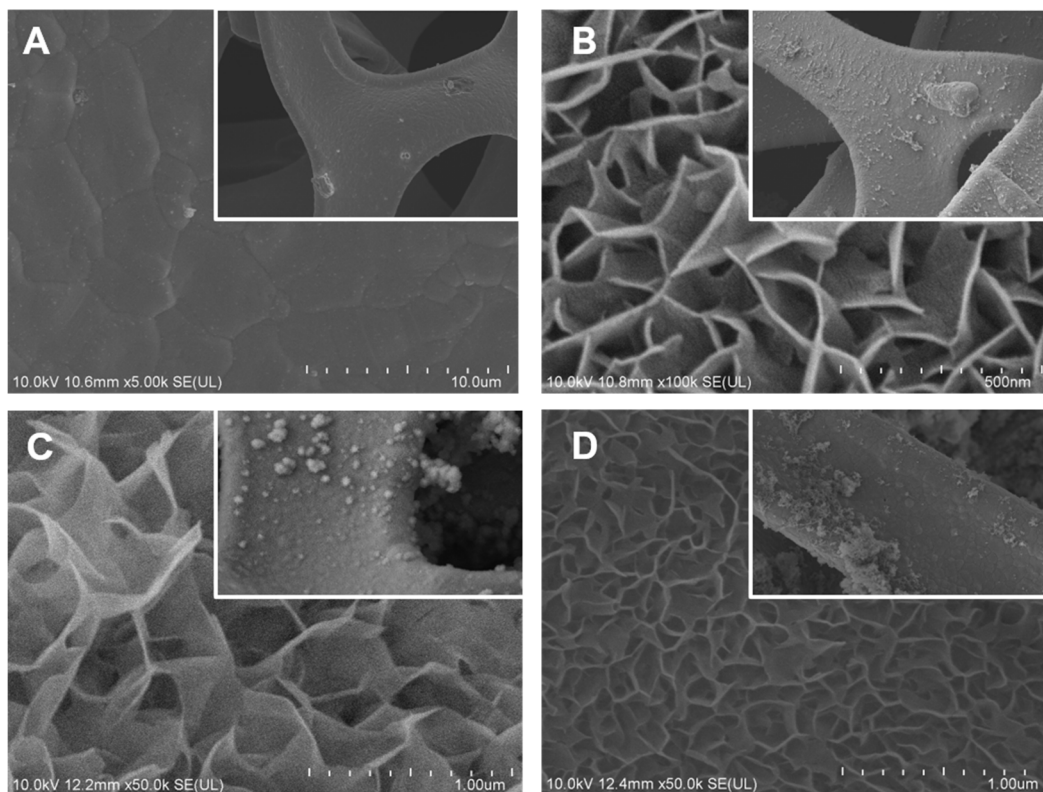


**Figure 7.5** SEM images of (a) Bare Ni foam, (b) e- M-NH//NF, (c) f- M-NH//NF, (d) o-M-NH//NF.

As the result of the hydrothermal reaction, the surface morphology of the M-NH//NF with different solvate shows the formation of  $\text{Ni}(\text{OH})_2$  nanowalls uniformly grow on the surface of carbon fibers, as shown in Fig.7.4. However, there is a little bit difference because of different solvent polarity. The morphology of f- M-NH//NF has the most fluffy and extremely thin surface flakes on the surface of Ni foam which will provide better SSA for the energy storage. On the contrary, the surface of the other two materials is more compact and closer to the bulk material.

### 7.3 Electrochemical Performance

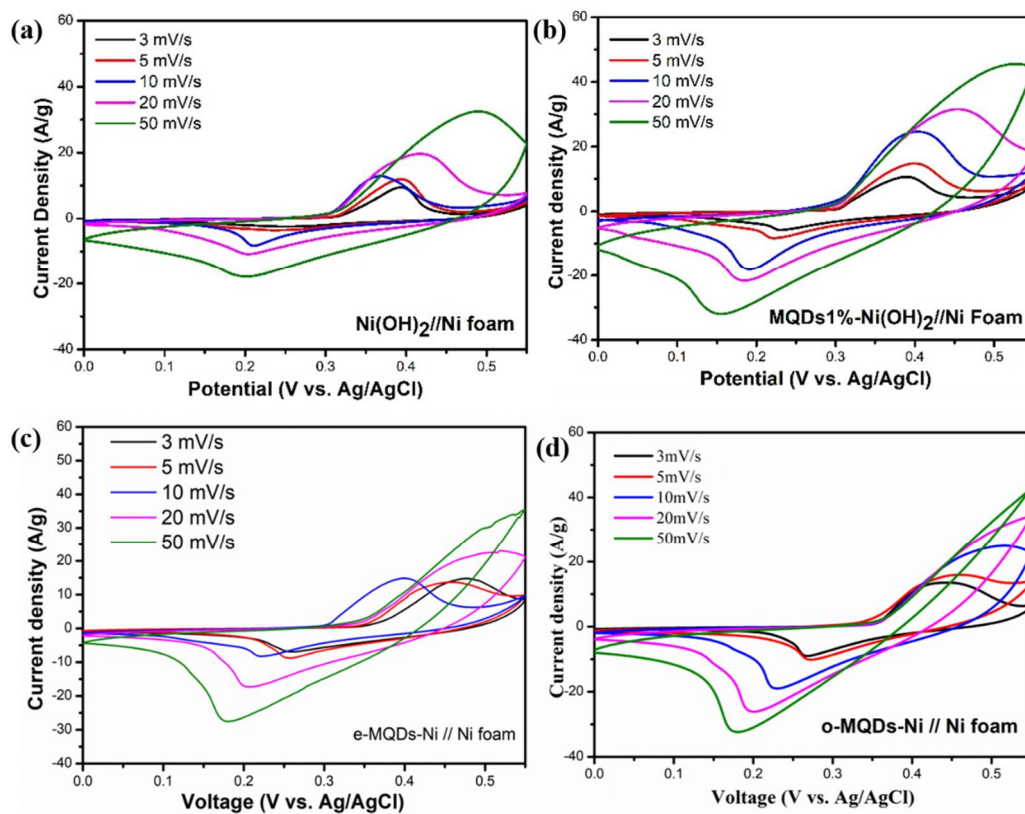


**Figure 7.6** CV curve of (a) NH//NF, (b) f- M-NH//NF, (c) e-M-NH//NF and (d) o-M-NH//NF.

The electrochemical performances of  $\text{Ni}(\text{OH})_2$  and M-NH//NF nanocomposites are investigated by CV (Fig.7.5). The CV curves exhibit two strong redox peaks in KOH (2M) electrolyte, which is normally from surface faradic redox reactions. In Fig.7.5b, the CV curves of f- M-NH//NF at different scan rate ( $3\text{--}50\text{ mV}\cdot\text{s}^{-1}$  between 0-0.6 V) have been demonstrated. Based on the CV curves with different scan rate, the capacitances of f- M-NH//NF are 1478.8, 1250.9, 960, 817 and 591.6 F/g at scan rates of 3, 5, 10, 20 and 50 mV/s, respectively. The values are obviously higher than those of other samples at the same scan rate (Fig.7.5a,c,d) and number is shown in table 7.1. Different with CV curves of bare  $\text{Ni}(\text{OH})_2$  (Fig.7.5a, the redox peaks of f- M-NH//NF have no obvious moving along with the increasing of scan rate, indicating it has high-rate discharge performance and perfectly reversible redox reaction.

**Table 7.1** the specific capacitance of NH//NF, f- M-NH//NF, e-M-NH//NF and o-M-NH//NF calculated by CV curve with different scan rate (F/g).

Sample	3 mV/s	5 mV/s	10 mV/s	20 mV/s	50 mV/s
NH//NF	800	676.4	454.5	437.3	314.2
e- M-NH//NF	1236	1138	814	497	256
o- M-NH//NF	1303	1050	1043	595	236
f- M-NH//NF	1478.8	1250	960	817	591.6
0.5%	1357	1203	1102	731.8	430
2%	1048.5	829.1	641.8	416	402.7

From Fig.7.6, CV curve of f- M-NH//NF with different percentage of MQDs can illustrated 1% of f-MQDs has the best electrochemical properties compared with 0.5% and 2%.

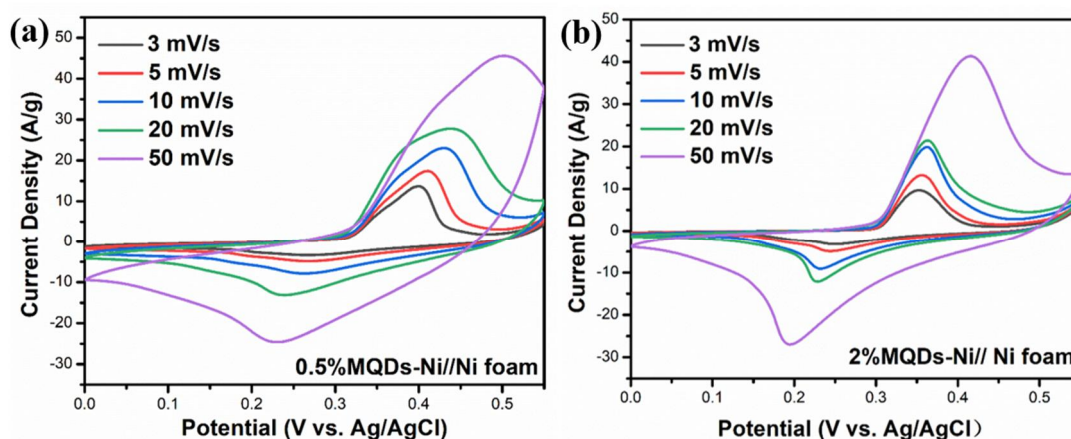


**Figure 7.7** CV curve of (a) 0.5% f- M-NH//NF, (b) 2% f- M-NH//NF.

Fig.7.7 shows galvanostatic charging and discharge (GCD) curve of f- M-NH//NF and NH//NF at current density of 1-16 A/g with the voltage window of 0-0.6 V. f- M-



NH//NF have the highest specific capacitance of 1660, 1440, 1191, 901.3 and 629.3 F/g at 1, 2, 4, 8 and 16 A/g. Under the same condition, the specific capacitance of NH//NF are 887, 785, 574, 455 and 345 F/g, respectively. Similar to CV curves, GCD curves also have a step which are corresponding to redox reaction potential.

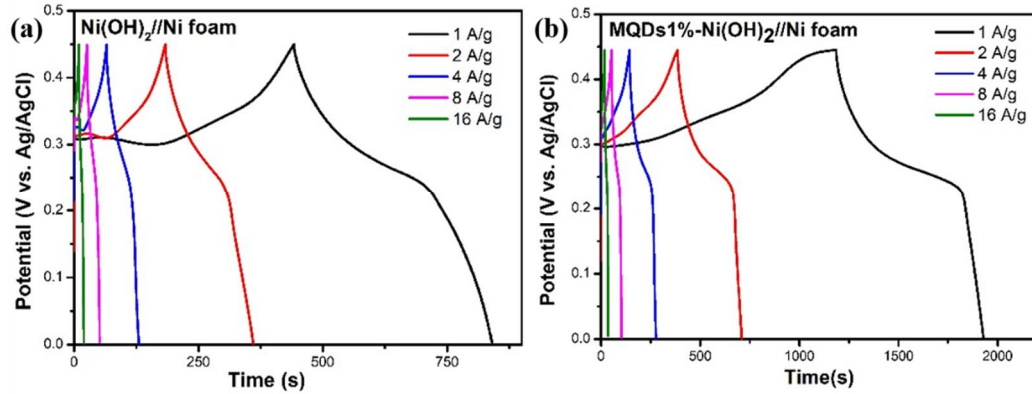


**Figure 7.8** GCD curve of (a) NH//NF and (b) f- M-NH//NF.

## 7.4 Summary

Mxene quantum dots have been successfully synthesized by microwave assistant, and further composited with Ni(OH)<sub>2</sub> and cover on the surface of Ni foam by a mild one step method. Mxene adsorbed on the surface of Ni(OH)<sub>2</sub> by electrostatic force while Ni(OH)<sub>2</sub> growth from the unit cell. Structure would not fall off even in the alkaline electrolyte. Among the three solvents with different polarities, the composite prepared by DMF has the best morphology and electrochemical performance of 1660 F/g at 1 A/g. In addition, 1% of MQDs is the best amount for f-M-NH//NF as electrode material than 0.5% and 2%. This work shows that Mxene quantum dots have good conductivity and are very suitable for increasing the electrical stability and energy density of supercapacitors.

## Chapter 8: Summary

### 8.1 Conclusion

In order to improve the energy storage performance of lithium batteries and supercapacitors, this dissertation discussed and prepared four kind of nickel-based composite with quantum dots, h-NiO, G-NH//CC, B-CNQD<sub>x</sub>-Ni and M-NH//NF. All of the novel materials have improved the electrochemical properties of Nickel oxide or hydroxide.

In the first part, we have synthesized the hierarchical nanostructured NiO microtubes successfully by a simple wet-chemical method followed by the calcination of  $\alpha$ -Ni(OH)<sub>2</sub> precursor. The unique hierarchical nanostructure of h-NiO microtubes plays a crucial role in exhibiting the superior electrochemical performance for LIBs, which not only relieves the stress caused by the volume change during the charge-discharge cycles, but also provides a high surface area and pore volume to facilitate the electrochemical reaction as well as the electron and ion transfer. The h-NiO microtubes show a high discharge capacity of 747 mAh/g at a current density of 0.5 C after 200 cycles, and also exhibit a discharge capacity of 616 mAh/g at a current density of 2 C. Therefore, the proposed synthesis method and the h-NiO microtubes can be a promising method for improving the electrochemical performance in the application of LIBs.

Through the second part, we have fabricated the GQDs/Ni(OH)<sub>2</sub> nanocomposite on flexible CC via the hydrothermal process. GQDs well embedded in Ni(OH)<sub>2</sub> nano-walls can enhance the overall electrical conductivity and ion diffusion, which result in the superior electrochemical performances. G10-NH//CC electrode delivers an excellent specific capacitance of 1825 F/g at a current density of 1 A/g and a good cycle stability of 83.5% capacity retention after 8000 cycles. Moreover, we also synthesized the symmetric supercapacitor using G10-NH//CC electrodes performs a high energy density of 80.8 Wh/kg at 2021 W/kg with good flexibility. These results suggest that

this novel strategy for fabricating various GQDs/metal oxide or GQDs/metal hydroxide provides great potential for advanced electrochemical energy storage devices.

For third part, boron doping g-C<sub>3</sub>N<sub>4</sub> quantum dots (B-CNQDs) have been successfully synthesized, and further composited with Ni(OH)<sub>2</sub> nanoflowers by a mild impregnation method. B-CNQDs adsorbed on the surface of Ni(OH)<sub>2</sub> by electrostatic force and would not fall off even in the alkaline electrolyte. In the composites with different ratio, B-CNQD10-Ni(OH)<sub>2</sub> displayed an excellent work in electrochemical performance with a specific capacitance of 1700 F·g<sup>-1</sup> at 1.5 A·g<sup>-1</sup>, low resistance of 7.421 Ω compared with Ni(OH)<sub>2</sub> (16.74 Ω) and great cycling performance even after 5000 cycles (82%).

In the final part, Mxene quantum dots were synthesized by hydrothermal reactions with microwave assistant with different solvent. The best MQD-Ni//Ni foam sample has an excellent specific capacitance of 1660 F/g at 1 A/g with 1% of MQDs in DMF solvate.

## **8.2 Recommendation**

In this thesis, I compounded the nickel-based material with the quantum dots, which originally had poor cycle performance, and greatly improved its electrochemical performance. However, the development of electrode materials for supercapacitors and lithium batteries is still a big problem. Although the safety of nickel-based discretion is relatively stable based on the micro-experimental data I have done, once it is applied to commercial support, its safety still needs further research. Blindly increasing the energy density of a battery or capacitor is very dangerous, and it is prone to explosions, liquid leakage, gas leakage and other dangers. Whether these materials can be used in business is what I want to study in the further.

## REFERENCE

- [1]. Bill Nussey, If we used this much fossil fuel in Edison's time, we'd have already run out, <https://www.freeingenergy.com/if-we-used-this-much-fossil-fuel-in-edisons-time-wed-have-already-run-out>, 2018-02-19.
- [2]. Zhang, Yadi, Jiangmin Jiang, Yufeng An, Langyuan Wu, Hui Dou, Jiaoxia Zhang, Yu Zhang et al. "Sodium ion capacitors: materials, mechanism and challenges." *ChemSusChem* (2020).
- [3]. 3. Zubi, Ghassan, Rodolfo Dufo-López, Monica Carvalho, and Guzay Pasaoglu. "The lithium-ion battery: State of the art and future perspectives." *Renewable and Sustainable Energy Reviews* 89 (2018): 292-308.
- [4]. Liu, Kai, Yayuan Liu, Dingchang Lin, Allen Pei, and Yi Cui. "Materials for lithium-ion battery safety." *Science advances* 4, no. 6 (2018): eaas9820.
- [5]. Yoshino, Akira. "The birth of the lithium ion battery." *Angewandte Chemie International Edition* 51, no. 24 (2012): 5798-5800.
- [6]. Manthiram, Arumugam. "An outlook on lithium-ion battery technology." *ACS central science* 3, no. 10 (2017): 1063-1069.
- [7]. Lu, Languang, Xuebing Han, Jianqiu Li, Jianfeng Hua, and Minggao Ouyang. "A review on the key issues for lithium-ion battery management in electric vehicles." *Journal of power sources* 226 (2013): 272-288.
- [8]. Curry, Claire. "Lithium-ion battery costs and market." *Bloomberg New Energy Finance* 5 (2017): 4-6.
- [9]. Daniel, Claus. "Materials and processing for lithium-ion batteries." *Jom* 60, no. 9 (2008): 43-48.
- [10]. Horiba, Tatsuo. "Lithium-ion battery systems." *Proceedings of the IEEE* 102, no. 6 (2014): 939-950.
- [11]. Chawla, Neha, Neelam Bharti, and Shailendra Singh. "Recent advances in non-flammable electrolytes for safer lithium-ion batteries." *Batteries* 5, no. 1 (2019): 19.
- [12]. Agubra, Victor, and Jeffrey Fergus. "Lithium-ion battery anode aging mechanisms." *Materials* 6, no. 4 (2013): 1310-1325.
- [13]. De las Casas, Charles, and Wenzhi Li. "A review of application of carbon nanotubes for lithium-ion battery anode material." *Journal of Power Sources* 208 (2012): 74-85.
- [14]. Manthiram, Arumugam. "A reflection on lithium-ion battery cathode chemistry." *Nature communications* 11, no. 1 (2020): 1-9.
- [15]. Zhang, Xiangchun, Ann Marie Sastry, and Wei Shyy. "Intercalation-induced stress and heat generation within single lithium-ion battery cathode particles." *Journal of The Electrochemical Society* 155, no. 7 (2008): A542.
- [16]. Nan, Caiyun, Jun Lu, Lihong Li, Lingling Li, Qing Peng, and Yadong Li. "Size and shape control of LiFePO<sub>4</sub> nanocrystals for better lithium-ion battery cathode materials." *Nano Research* 6, no. 7 (2013): 469-477.
- [17]. Zhang, Jianjun, Zhihong Liu, Qingshan Kong, Chuanjian Zhang, Shuping Pang,

- Liping Yue, Xuejiang Wang, Jianhua Yao, and Guanglei Cui. "Renewable and superior thermal-resistant cellulose-based composite nonwoven as lithium-ion battery separator." *ACS applied materials & interfaces* 5, no. 1 (2013): 128-134.
- [18]. Sloop, Steven E., John B. Kerr, and Kim Kinoshita. "The role of Li-ion battery electrolyte reactivity in performance decline and self-discharge." *Journal of power sources* 119 (2003): 330-337.
- [19]. Ritchie, Andrew, and Wilmont Howard. "Recent developments and likely advances in lithium-ion batteries." *Journal of Power Sources* 162, no. 2 (2006): 809-812.
- [20]. Fan, Xiao-Yong, Fu-Sheng Ke, Guo-Zhen Wei, Ling Huang, and Shi-Gang Sun. "Sn-Co alloy anode using porous Cu as current collector for lithium-ion battery." *Journal of Alloys and Compounds* 476, no. 1-2 (2009): 70-73.
- [21]. Deng, Da. "Li ion batteries: basics, progress, and challenges." *Energy Science & Engineering* 3, no. 5 (2015): 385-418.
- [22]. Galvez-Aranda, Diego E., Victor Ponce, and Jorge M. Seminario. "Molecular dynamics simulations of the first charge of a Li-ion—Si-anode nanobattery." *Journal of molecular modeling* 23, no. 4 (2017): 120.
- [23]. Roselin, L. Selva, Ruey-Shin Juang, Chien-Te Hsieh, Suresh Sagadevan, Ahmad Umar, Rosilda Selvin, and Hosameldin H. Hegazy. "Recent advances and perspectives of carbon-based nanostructures as anode materials for Li-ion batteries." *Materials* 12, no. 8 (2019): 1229.
- [24]. Radin, Maxwell D., Sunny Hy, Mahsa Sina, Chengcheng Fang, Haodong Liu, Julija Vinckeviciute, Minghao Zhang, M. Stanley Whittingham, Y. Shirley Meng, and Anton Van der Ven. "Narrowing the gap between theoretical and practical capacities in Li ion layered oxide cathode materials." *Advanced Energy Materials* 7, no. 20 (2017): 1602888.
- [25]. Buqa, Hilmi, Andreas Würsig, Jens Vetter, M. E. Spahr, Frank Krumeich, and Petr Novák. "SEI film formation on highly crystalline graphitic materials in lithium-ion batteries." *Journal of power sources* 153, no. 2 (2006): 385-390.
- [26]. Buqa, Hilmi, Andreas Würsig, Jens Vetter, M. E. Spahr, Frank Krumeich, and Petr Novák. "SEI film formation on highly crystalline graphitic materials in lithium-ion batteries." *Journal of power sources* 153, no. 2 (2006): 385-390.
- [27]. Peled, E., D. Golodntsky, G. Ardel, C. Menachem, D. Bar Tow, and V. Eshkenazy. "The role of SEI in lithium and lithium-ion batteries." *MRS Online Proceedings Library Archive* 393 (1995).
- [28]. Zhang, Liuyang, Diwen Shi, Tao Liu, Mietek Jaroniec, and Jiaguo Yu. "Nickel-based materials for supercapacitors." *Materials Today* 25 (2019): 35-65.
- [29]. Jiang, Yuqi, and Jinping Liu. "Definitions of pseudocapacitive materials: a brief review." *energy & environmental materials* 2, no. 1 (2019): 30-37.
- [30]. Obreja, Vasile VN. "On the performance of supercapacitors with electrodes based on carbon nanotubes and carbon activated material—a review." *Physica E: Low-dimensional Systems and Nanostructures* 40, no. 7 (2008): 2596-2605.
- [31]. Fan, Zhuangjun, Jun Yan, Tong Wei, Linjie Zhi, Guoqing Ning, Tianyou Li, and Fei Wei. "Asymmetric supercapacitors based on graphene/MnO<sub>2</sub> and activated

- carbon nanofiber electrodes with high power and energy density." *Advanced Functional Materials* 21, no. 12 (2011): 2366-2375.
- [32]. Wang, Rutao, Xingbin Yan, Junwei Lang, Zongmin Zheng, and Peng Zhang. "A hybrid supercapacitor based on flower-like  $\text{Co}(\text{OH})_2$  and urchin-like VN electrode materials." *Journal of materials chemistry A* 2, no. 32 (2014): 12724-12732.
- [33]. Jänes, Alar, Heisi Kurig, and Enn Lust. "Characterisation of activated nanoporous carbon for supercapacitor electrode materials." *Carbon* 45, no. 6 (2007): 1226-1233.
- [34]. Najib, Sumaiyah, and Emre Erdem. "Current progress achieved in novel materials for supercapacitor electrodes: mini review." *Nanoscale Advances* 1, no. 8 (2019): 2817-2827.
- [35]. Wang, Hailiang, Hernan Sanchez Casalongue, Yongye Liang, and Hongjie Dai. " $\text{Ni}(\text{OH})_2$  nanoplates grown on graphene as advanced electrochemical pseudocapacitor materials." *Journal of the American Chemical Society* 132, no. 21 (2010): 7472-7477.
- [36]. Iro, Zaharaddeen S., C. Subramani, and S. S. Dash. "A brief review on electrode materials for supercapacitor." *Int. J. Electrochem. Sci* 11, no. 12 (2016): 10628-10643.
- [37]. González, Ander, Eider Goikolea, Jon Andoni Barrena, and Roman Mysyk. "Review on supercapacitors: Technologies and materials." *Renewable and Sustainable Energy Reviews* 58 (2016): 1189-1206.
- [38]. Wu, Yuping, Changyin Jiang, Chunrong Wan, and Eishun Tsuchida. "Effects of catalytic oxidation on the electrochemical performance of common natural graphite as an anode material for lithium-ion batteries." *Electrochemistry Communications* 2, no. 4 (2000): 272-275.
- [39]. Li, Lingjie, Jie Zhang, Jinglei Lei, Jing Xu, Bo Shang, Lei Liu, Nianbing Li, and Fusheng Pan. "O-Vacancy-enriched  $\text{NiO}$  hexagonal platelets fabricated on Ni foam as a self-supported electrode for extraordinary pseudocapacitance." *Journal of Materials Chemistry A* 6, no. 16 (2018): 7099-7106.
- [40]. Mao, Yongyun, Jiyang Xie, Huan Liu, and Wanbiao Hu. "Hierarchical core-shell  $\text{Ag}@\text{Ni}(\text{OH})_2@ \text{PPy}$  nanowire electrode for ultrahigh energy density asymmetric supercapacitor." *Chemical Engineering Journal* 405 (2021): 126984.
- [41]. Liu, Fangyan, Xiang Chu, Haitao Zhang, Binbin Zhang, Hai Su, Long Jin, Zixing Wang, Haichao Huang, and Weiqing Yang. "Synthesis of self-assembly 3D porous  $\text{Ni}(\text{OH})_2$  with high capacitance for hybrid supercapacitors." *Electrochimica Acta* 269 (2018): 102-110.
- [42]. Bimberg, Dieter, and Udo W. Pohl. "Quantum dots: promises and accomplishments." *Materials Today* 14, no. 9 (2011): 388-397.
- [43]. Warburton, Richard J. "Self-assembled semiconductor quantum dots." *Contemporary physics* 43, no. 5 (2002): 351-364.
- [44]. Bockelmann, U., W. Heller, A. Filoramo, and Ph Roussignol. "Microphotoluminescence studies of single quantum dots. I. Time-resolved experiments." *Physical Review B* 55, no. 7 (1997): 4456.

- [45]. Ritter, Kyle A., and Joseph W. Lyding. "The influence of edge structure on the electronic properties of graphene quantum dots and nanoribbons." *Nature materials* 8, no. 3 (2009): 235-242.
- [46]. Shiohara, Amane, Sujay Prabakar, Angelique Faramus, Chia-Yen Hsu, Ping-Shan Lai, Peter T. Northcote, and Richard D. Tilley. "Sized controlled synthesis, purification, and cell studies with silicon quantum dots." *Nanoscale* 3, no. 8 (2011): 3364-3370.
- [47]. Bacon, Mitchell, Siobhan J. Bradley, and Thomas Nann. "Graphene quantum dots." *Particle & Particle Systems Characterization* 31, no. 4 (2014): 415-428.
- [48]. Chen, Jin-Long, and Chang-Qing Zhu. "Functionalized cadmium sulfide quantum dots as fluorescence probe for silver ion determination." *Analytica Chimica Acta* 546, no. 2 (2005): 147-153.
- [49]. Pejova, Biljana, Atanas Tanuševski, and Ivan Grozdanov. "Semiconducting thin films of zinc selenide quantum dots." *Journal of Solid State Chemistry* 177, no. 12 (2004): 4785-4799.
- [50]. Peterson, Jeffrey J., and Todd D. Krauss. "Fluorescence spectroscopy of single lead sulfide quantum dots." *Nano letters* 6, no. 3 (2006): 510-514.
- [51]. Zhang, Xingyan, Qiangang Fu, Heming Huang, Lu Wei, and Xin Guo. "Silver quantum dot modified MoO<sub>3</sub> and MnO<sub>2</sub> paper like freestanding films for flexible solid state asymmetric supercapacitors." *Small* 15, no. 13 (2019): 1805235.
- [52]. Deng, Gang, Dongliang Chao, Yuwei Guo, Zhen Chen, Huanhuan Wang, Serguei V. Savirov, Jianyi Lin, and Ze Xiang Shen. "Graphene quantum dots-shielded Na<sub>3</sub>(VO)<sub>2</sub>(PO<sub>4</sub>)<sub>2</sub>F@C nanocuboids as robust cathode for Na-ion battery." *Energy Storage Materials* 5 (2016): 198-204.
- [53]. Wu, Ping, Yuxia Xu, Jingyi Zhan, Yan Li, Huaiguo Xue, and Huan Pang. "The research development of quantum dots in electrochemical energy storage." *Small* 14, no. 42 (2018): 1801479.
- [54]. Yuan, Jun, Xiang Hu, Junxiang Chen, Yangjie Liu, Taizhong Huang, and Zhenhai Wen. "In situ formation of vanadium nitride quantum dots on N-doped carbon hollow spheres for superior lithium and sodium storage." *Journal of Materials Chemistry A* 7, no. 15 (2019): 9289-9296.
- [55]. Srinivasan, Venkat, and John W. Weidner. "An electrochemical route for making porous nickel oxide electrochemical capacitors." *Journal of the Electrochemical Society* 144.8 (1997): L210.
- [56]. Chavan, U. S., P. E. Lokhande, and Suraj Bhosale. "Nickel hydroxide nanosheets grown on nickel foam for high performance supercapacitor applications." *Materials Technology* (2021): 1-7.
- [57]. Yue, G. H., Y. C. Zhao, C. G. Wang, X. X. Zhang, X. Q. Zhang, and Q. S. Xie. "Flower-like nickel oxide nanocomposites anode materials for excellent performance lithium-ion batteries." *Electrochimica Acta* 152 (2015): 315-322.
- [58]. Zou, Yuqin, and Yong Wang. "Microwave-assisted synthesis of porous nickel oxide nanostructures as anode materials for lithium-ion batteries." *Rare Metals* 30, no. 1 (2011): 59-62.

- [59]. Ni, Shibing, Xiaohu Lv, Jianjun Ma, Xuelin Yang, and Lulu Zhang. "A novel electrochemical reconstruction in nickel oxide nanowalls on Ni foam and the fine electrochemical performance as anode for lithium-ion batteries." *Journal of Power Sources* 270 (2014): 564-568.
- [60]. Cao, Peiqi, Lincai Wang, Yanjie Xu, Yanbao Fu, and Xiaohua Ma. "Facile hydrothermal synthesis of mesoporous nickel oxide/reduced graphene oxide composites for high performance electrochemical supercapacitor." *Electrochimica Acta* 157 (2015): 359-368.
- [61]. Chen, Wei, Dayong Gui, and Jianhong Liu. "Nickel oxide/graphene aerogel nanocomposite as a supercapacitor electrode material with extremely wide working potential window." *Electrochimica Acta* 222 (2016): 1424-1429.
- [62]. Zhang, Jing, Xi-bin Yi, Xiu-Chun Wang, Jie Ma, Shuo Liu, and Xiao-Jun Wang. "Nickel oxide grown on carbon nanotubes/carbon fiber paper by electrodeposition as flexible electrode for high-performance supercapacitors." *Journal of Materials Science: Materials in Electronics* 26, no. 10 (2015): 7901-7908.
- [63]. Sun, Xiang, Gongkai Wang, Hongtao Sun, Fengyuan Lu, Mingpeng Yu, and Jie Lian. "Morphology controlled high performance supercapacitor behaviour of the Ni-Co binary hydroxide system." *Journal of power sources* 238 (2013): 150-156.
- [64]. Liu, Jilei, Minghua Chen, Lili Zhang, Jian Jiang, Jiayu Yan, Yizhong Huang, Jianyi Lin, Hong Jin Fan, and Ze Xiang Shen. "A flexible alkaline rechargeable Ni/Fe battery based on graphene foam/carbon nanotubes hybrid film." *Nano letters* 14, no. 12 (2014): 7180-7187.
- [65]. Wang, De-Gao, Zibin Liang, Song Gao, Chong Qu, and Ruqiang Zou. "Metal-organic framework-based materials for hybrid supercapacitor application." *Coordination Chemistry Reviews* 404 (2020): 213093.
- [66]. Zhao, Shaofei, Lizhen Zeng, Gao Cheng, Lin Yu, and Huaqiang Zeng. "Ni/Co-based metal-organic frameworks as electrode material for high performance supercapacitors." *Chinese Chemical Letters* 30, no. 3 (2019): 605-609.
- [67]. Du, Pengcheng, Yuman Dong, Chang Liu, Wenli Wei, Dong Liu, and Peng Liu. "Fabrication of hierarchical porous nickel-based metal-organic framework (Ni-MOF) constructed with nanosheets as novel pseudo-capacitive material for asymmetric supercapacitor." *Journal of colloid and interface science* 518 (2018): 57-68.
- [68]. Rawool, Chaitali R., Shashi P. Karna, and Ashwini K. Srivastava. "Enhancing the supercapacitive performance of Nickel based metal organic framework-carbon nanofibers composite by changing the ligands." *Electrochimica Acta* 294 (2019): 345-356.
- [69]. Zhang, Xu, Ning Qu, Shixuan Yang, Qiuyu Fan, Da Lei, Anmin Liu, and Xi Chen. "Shape-controlled synthesis of Ni-based metal-organic frameworks with albizia flower-like spheres@ nanosheets structure for high performance supercapacitors." *Journal of colloid and interface science* 575 (2020): 347-355.
- [70]. He, Fan, Nana Yang, Kanshe Li, Xiaoqin Wang, Shaoling Cong, Linsen Zhang,



- Shanxin Xiong, and Anning Zhou. "Hydrothermal synthesis of Ni-based metal organic frameworks/graphene oxide composites as supercapacitor electrode materials." *Journal of Materials Research* 35, no. 11 (2020): 1439-1450.
- [71]. Liu, Kang, Liming Deng, Hongdong Li, Yuxiang Bao, Zhenyu Xiao, Bin Li, Qi Zhou, Yanling Geng, and Lei Wang. "Two isostructural Co/Ni fluorine-containing metal-organic frameworks for dye adsorption and supercapacitor." *Journal of Solid State Chemistry* 275 (2019): 1-7.
- [72]. Chen, Xiaoye, Xuemin Wu, Hongxu Guo, and Wei Fu. "Improvement of capacitance activity for Cu doped Ni based metal-organic frameworks by adding potassium hexacyanoferrate into KOH electrolyte." *Applied Organometallic Chemistry* 33, no. 11 (2019): e5193.
- [73]. Patterson, Nigel, Bo Xiao, and Anna Ignaszak. "Polypyrrole decorated metal-organic frameworks for supercapacitor devices." *RSC Advances* 10, no. 34 (2020): 20162-20172.
- [74]. Wang, Aming, Hailong Wang, Shengyi Zhang, Changjie Mao, Jiming Song, Helin Niu, Baokang Jin, and Yupeng Tian. "Controlled synthesis of nickel sulfide/graphene oxide nanocomposite for high-performance supercapacitor." *Applied surface science* 282 (2013): 704-708.
- [75]. Liu, Shude, Kalimuthu Vijaya Sankar, Aniruddha Kundu, Ming Ma, Jang-Yeon Kwon, and Seong Chan Jun. "Honeycomb-like interconnected network of nickel phosphide heteronanoparticles with superior electrochemical performance for supercapacitors." *ACS applied materials & interfaces* 9, no. 26 (2017): 21829-21838.
- [76]. Shen, Ting, Liping Yang, Mei Er Pam, Yumeng Shi, and Hui Ying Yang. "Quantum dot-carbonaceous nanohybrid composites: preparation and application in electrochemical energy storage." *Journal of Materials Chemistry A* 8, no. 43 (2020): 22488-22506.
- [77]. Li, Xiaoming, Muchen Rui, Jizhong Song, Zihan Shen, and Haibo Zeng. "Carbon and graphene quantum dots for optoelectronic and energy devices: a review." *Advanced Functional Materials* 25, no. 31 (2015): 4929-4947.
- [78]. Bak, Sora, Doyoung Kim, and Hyoyoung Lee. "Graphene quantum dots and their possible energy applications: A review." *Current Applied Physics* 16, no. 9 (2016): 1192-1201.
- [79]. Chen, Qing, Yue Hu, Chuangang Hu, Huhu Cheng, Zhipan Zhang, Huibo Shao, and Liangti Qu. "Graphene quantum dots-three-dimensional graphene composites for high-performance supercapacitors." *Physical Chemistry Chemical Physics* 16, no. 36 (2014): 19307-19313.
- [80]. Lee, Keunsik, Hanleem Lee, Yonghun Shin, Yeohyeung Yoon, Doyoung Kim, and Hyoyoung Lee. "Highly transparent and flexible supercapacitors using graphene-graphene quantum dots chelate." *Nano Energy* 26 (2016): 746-754.
- [81]. Wang, Aiwu, Chundong Wang, Li Fu, Winnie Wong-Ng, and Yucheng Lan. "Recent advances of graphitic carbon nitride-based structures and applications in catalyst, sensing, imaging, and LEDs." *Nano-micro letters* 9, no. 4 (2017): 1-21.

- [82]. Meenu, Preetha Chandrasekharan, Santanu Prasad Datta, Satyapaul A. Singh, Srikanta Dinda, Chanchal Chakraborty, and Sounak Roy. "Polyaniline supported g-C<sub>3</sub>N<sub>4</sub> quantum dots surpass benchmark Pt/C: Development of morphologically engineered g-C<sub>3</sub>N<sub>4</sub> catalysts towards "metal-free" methanol electro-oxidation." *Journal of Power Sources* 461 (2020): 228150.
- [83]. Chen, Xiang, Qing Liu, Qiliang Wu, Pingwu Du, Jun Zhu, Songyuan Dai, and Shangfeng Yang. "Incorporating graphitic carbon nitride (g C<sub>3</sub>N<sub>4</sub>) quantum dots into bulk heterojunction polymer solar cells leads to efficiency enhancement." *Advanced Functional Materials* 26, no. 11 (2016): 1719-1728.
- [84]. Naguib, Michael, Murat Kurtoglu, Volker Presser, Jun Lu, Junjie Niu, Min Heon, Lars Hultman, Yury Gogotsi, and Michel W. Barsoum. "Two dimensional nanocrystals produced by exfoliation of Ti<sub>3</sub>AlC<sub>2</sub>." *Advanced materials* 23, no. 37 (2011): 4248-4253.
- [85]. Xue, Qi, Huijie Zhang, Minshen Zhu, Zengxia Pei, Hongfei Li, Zifeng Wang, Yang Huang et al. "Photoluminescent Ti<sub>3</sub>C<sub>2</sub> MXene quantum dots for multicolor cellular imaging." *Advanced Materials* 29, no. 15 (2017): 1604847.
- [86]. Zhao, Lin, Zhao Wang, Yan Li, Sen Wang, Lifeng Wang, Zhaojun Qi, Qiang Ge, Xiaoguang Liu, and Jin Zhong Zhang. "Designed synthesis of chlorine and nitrogen co-doped Ti<sub>3</sub>C<sub>2</sub> MXene quantum dots and their outstanding hydroxyl radical scavenging properties." *Journal of Materials Science & Technology* 78 (2021): 30-37.
- [87]. Dupin, Jean-Charles, Danielle Gonbeau, Philippe Vinatier, and Alain Levasseur. "Systematic XPS studies of metal oxides, hydroxides and peroxides." *Physical Chemistry Chemical Physics* 2, no. 6 (2000): 1319-1324.
- [88]. Vander Wal, Randy L., Vicky M. Bryg, and Michael D. Hays. "XPS analysis of combustion aerosols for chemical composition, surface chemistry, and carbon chemical state." *Analytical chemistry* 83, no. 6 (2011): 1924-1930.
- [89]. Biesinger, Mark C., Brad P. Payne, Andrew P. Grosvenor, Leo WM Lau, Andrea R. Gerson, and Roger St C. Smart. "Resolving surface chemical states in XPS analysis of first row transition metals, oxides and hydroxides: Cr, Mn, Fe, Co and Ni." *Applied Surface Science* 257, no. 7 (2011): 2717-2730.
- [90]. Yamashita, Toru, and Peter Hayes. "Analysis of XPS spectra of Fe<sup>2+</sup> and Fe<sup>3+</sup> ions in oxide materials." *Applied surface science* 254, no. 8 (2008): 2441-2449.
- [91]. Baer, Donald R., Daniel J. Gaspar, Ponnusamy Nachimuthu, Sirnegeda D. Techane, and David G. Castner. "Application of surface chemical analysis tools for characterization of nanoparticles." *Analytical and bioanalytical chemistry* 396, no. 3 (2010): 983-1002.
- [92]. Hüfner, Stephan. *Photoelectron spectroscopy: principles and applications*. Springer Science & Business Media, 2013.
- [93]. Fadley, Charles S. "X-ray photoelectron spectroscopy: Progress and perspectives." *Journal of Electron Spectroscopy and Related Phenomena* 178 (2010): 2-32.
- [94]. Drits, Victor, Jan Środoń, and D. D. Eberl. "XRD measurement of mean crystallite thickness of illite and illite/smectite: Reappraisal of the Kubler index

- and the Scherrer equation." *Clays and clay minerals* 45, no. 3 (1997): 461-475.
- [95]. Whittig, L. D., and W. R. Allardice. "X ray diffraction techniques." *Methods of Soil Analysis: Part 1 Physical and Mineralogical Methods* 5 (1986): 331-362.
- [96]. Bunaciu, Andrei A., Elena Gabriela Udriștioiu, and Hassan Y. Aboul-Enein. "X-ray diffraction: instrumentation and applications." *Critical reviews in analytical chemistry* 45, no. 4 (2015): 289-299.
- [97]. Monshi, Ahmad, Mohammad Reza Foroughi, and Mohammad Reza Monshi. "Modified Scherrer equation to estimate more accurately nano-crystallite size using XRD." *World journal of nano science and engineering* 2, no. 3 (2012): 154-160.
- [98]. Holmboe, Michael, Susanna Wold, and Mats Jonsson. "Porosity investigation of compacted bentonite using XRD profile modeling." *Journal of Contaminant Hydrology* 128, no. 1-4 (2012): 19-32.
- [99]. Holzwarth, Uwe, and Neil Gibson. "The Scherrer equation versus the 'Debye-Scherrer equation'." *Nature nanotechnology* 6, no. 9 (2011): 534-534.
- [100]. Faix, O. "Fourier transform infrared spectroscopy." In *Methods in lignin chemistry*, pp. 83-109. Springer, Berlin, Heidelberg, 1992.
- [101]. Izzo, Francesco, Chiara Germinario, Celestino Grifa, Alessio Langella, and Mariano Mercurio. "External reflectance FTIR dataset (4000–400  $\text{cm}^{-1}$ ) for the identification of relevant mineralogical phases forming Cultural Heritage materials." *Infrared Physics & Technology* 106 (2020): 103266.
- [102]. Krafft, C., and Valter Sergio. "Biomedical applications of Raman and infrared spectroscopy to diagnose tissues." *Spectroscopy* 20, no. 5-6 (2006): 195-218.
- [103]. Lingegowda, Deepashree C., J. Komal Kumar, AG Devi Prasad, Mahsa Zarei, and Shubha Gopal. "FTIR spectroscopic studies on Cleome gynandra—comparative analysis of functional group before and after extraction." *Romanian Journal of Biophysics* 22, no. 3-4 (2012): 137-143.
- [104]. McMullan, D. "Scanning electron microscopy 1928–1965." *Scanning* 17, no. 3 (1995): 175-185.
- [105]. Goldstein, Joseph, ed. *Practical scanning electron microscopy: electron and ion microprobe analysis*. Springer Science & Business Media, 2012.
- [106]. Grime, G. W., M. Dawson, M. Marsh, I. C. McArthur, and F. Watt. "The Oxford submicron nuclear microscopy facility." *Nuclear Instruments and Methods in Physics Research Section B: Beam Interactions with Materials and Atoms* 54, no. 1-3 (1991): 52-63.
- [107]. Crewe, Albert V., M. Isaacson, and D. Johnson. "A simple scanning electron microscope." *Review of Scientific Instruments* 40, no. 2 (1969): 241-246.
- [108]. Seiler, H. "Secondary electron emission in the scanning electron microscope." *Journal of Applied Physics* 54, no. 11 (1983): R1-R18.
- [109]. Williams, David B., and C. Barry Carter. "The transmission electron microscope." In *Transmission electron microscopy*, pp. 3-17. Springer, Boston, MA, 1996.
- [110]. Han, Yufeng, Jixiao Wang, Hairui Zhang, Song Zhao, Qiang Ma, and Zhi Wang. "Electrochemical impedance spectroscopy (EIS): an efficiency method to

- monitor resin curing processes." *Sensors and Actuators A: Physical* 250 (2016): 78-86.
- [111]. Kwon, Woosung, Jung-Min Kim, and Shi-Woo Rhee. "A new equivalent circuit model for porous carbon electrodes in charge transfer reaction of iodide/triiodide redox couples." *Electrochimica acta* 68 (2012): 110-113.
- [112]. Zhang, Jiaoxia, Zhuangzhuang Zhang, Yueting Jiao, Hongxun Yang, Yuqing Li, Jing Zhang, and Peng Gao. "The graphene/lanthanum oxide nanocomposites as electrode materials of supercapacitors." *Journal of Power Sources* 419 (2019): 99-105.
- [113]. Lu, Zhiyi, Zheng Chang, Junfeng Liu, and Xiaoming Sun. "Stable ultrahigh specific capacitance of NiO nanorod arrays." *Nano research* 4, no. 7 (2011): 658-665.
- [114]. Aghazadeh, Mustafa, Amir Rashidi, Mohammad Reza Ganjali, and Mohammad Ghannadi Maragheh. "Nickel oxide nano-rods/plates as a high-performance electrode material for supercapacitors; electrosynthesis and evolution of charge storage ability." *Int. J. Electrochem. Sci* 11 (2016): 11002-11015.
- [115]. Kong, Menglai, Zao Wang, Weiyi Wang, Min Ma, Danni Liu, Shuai Hao, Rongmei Kong et al. "NiCoP nanoarray: a superior pseudocapacitor electrode with high areal capacitance." *Chemistry—A European Journal* 23, no. 18 (2017): 4435-4441.
- [116]. Jiang, Cheng, Bojun Wang, Zhenrui Wu, Jiliang Qiu, Zhengping Ding, Jian Zou, Shulin Chen et al. "Electrolyte-assisted dissolution-recrystallization mechanism towards high energy density and power density CF cathodes in potassium cell." *Nano Energy* 70 (2020): 104552.
- [117]. Yang, Hao, Santhakumar Kannappan, Amaresh S. Pandian, Jae-Hyung Jang, Yun Sung Lee, and Wu Lu. "Graphene supercapacitor with both high power and energy density." *Nanotechnology* 28, no. 44 (2017): 445401.
- [118]. Luo, Yuanyuan, Guanghai Li, Guotao Duan, and Lide Zhang. "One-step synthesis of spherical  $\alpha$ -Ni(OH)<sub>2</sub> nanoarchitectures." *Nanotechnology* 17, no. 16 (2006): 4278.
- [119]. Hall, David S., David J. Lockwood, Christina Bock, and Barry R. MacDougall. "Nickel hydroxides and related materials: a review of their structures, synthesis and properties." *Proceedings of the Royal Society A: Mathematical, Physical and Engineering Sciences* 471, no. 2174 (2015): 20140792.
- [120]. Xu, Qing-Sheng, Yan-Juan Zhu, Liang-Guo Huang, Jie Luo, Zhong-Ju Zhang, Cheng-Cheng Miao, and Hu Ye. "Phase and particle of Y-doped Ni(OH)<sub>2</sub> prepared from different nickel sources and Na<sub>2</sub>CO<sub>3</sub> amount." *Rare Metals* 33, no. 2 (2014): 219-224.
- [121]. Al-Nafiey, Amer, Anurag Kumar, Malika Kumar, Ahmed Addad, Brigitte Sieber, Sabine Szunerits, Rabah Boukherroub, and Suman L. Jain. "Nickel oxide nanoparticles grafted on reduced graphene oxide (rGO/NiO) as efficient photocatalyst for reduction of nitroaromatics under visible light irradiation." *Journal of Photochemistry and Photobiology A: Chemistry* 336 (2017): 198-207.
- [122]. Li, Xifei, Abirami Dhanabalan, Kevin Bechtold, and Chunlei Wang. "Binder-

- free porous core–shell structured Ni/NiO configuration for application of high performance lithium ion batteries." *Electrochemistry Communications* 12, no. 9 (2010): 1222-1225.
- [123]. Wang, Chong, Dianlong Wang, Qiuming Wang, and Huanjun Chen. "Fabrication and lithium storage performance of three-dimensional porous NiO as anode for lithium-ion battery." *Journal of Power Sources* 195, no. 21 (2010): 7432-7437.
- [124]. Zhou, Guangmin, Da-Wei Wang, Feng Li, Lili Zhang, Na Li, Zhong-Shuai Wu, Lei Wen, Gao Qing Lu, and Hui-Ming Cheng. "Graphene-wrapped Fe<sub>3</sub>O<sub>4</sub> anode material with improved reversible capacity and cyclic stability for lithium ion batteries." *Chemistry of materials* 22, no. 18 (2010): 5306-5313.
- [125]. Wang, Hailiang, Li-Feng Cui, Yuan Yang, Hernan Sanchez Casalongue, Joshua Tucker Robinson, Yongye Liang, Yi Cui, and Hongjie Dai. "Mn<sub>3</sub>O<sub>4</sub>-graphene hybrid as a high-capacity anode material for lithium ion batteries." *Journal of the American Chemical Society* 132, no. 40 (2010): 13978-13980.
- [126]. Sun, Xiaolei, Chenglin Yan, Yao Chen, Wenping Si, Junwen Deng, Steffen Oswald, Lifeng Liu, and Oliver G. Schmidt. "Three dimensionally "curved" NiO nanomembranes as ultrahigh rate capability anodes for Li ion batteries with long cycle lifetimes." *Advanced Energy Materials* 4, no. 4 (2014): 1300912.
- [127]. Liu, Chueh, Changling Li, Kazi Ahmed, Zafer Mutlu, Cengiz S. Ozkan, and Mihrimah Ozkan. "Template free and binderless NiO nanowire foam for Li-ion battery anodes with long cycle life and ultrahigh rate capability." *Scientific reports* 6, no. 1 (2016): 1-8.
- [128]. Wiston, Biny R., and M. Ashok. "Electrochemical performance of hydrothermally synthesized flower-like  $\alpha$ -nickel hydroxide." *Vacuum* 160 (2019): 12-17.
- [129]. Gund, Girish S., Deepak P. Dubal, Sujata S. Shinde, and Chandrakant D. Lokhande. "One step hydrothermal synthesis of micro-belts like  $\beta$ -Ni(OH)<sub>2</sub> thin films for supercapacitors." *Ceramics International* 39, no. 6 (2013): 7255-7261.
- [130]. Mao, Yuqiong, Taotao Li, Chunli Guo, Fuchun Zhu, Chunchen Zhang, Yinghui Wei, and Lifeng Hou. "Cycling stability of ultrafine  $\beta$ -Ni(OH)<sub>2</sub> nanosheets for high capacity energy storage device via a multilayer nickel foam electrode." *Electrochimica Acta* 211 (2016): 44-51.
- [131]. Wiston, Biny R., and M. Ashok. "Electrochemical performance of nickel hydroxide nanopetals for supercapacitor electrodes." *Materials Letters* 235 (2019): 76-79.
- [132]. Sun, Haiyan, Suwen Liu, Qifang Lu, and Hongyan Zhong. "Template-synthesis of hierarchical Ni (OH) 2 hollow spheres with excellent performance as supercapacitor." *Materials Letters* 128 (2014): 136-139.
- [133]. Li, Jing, Huilian Hao, Jianjun Wang, Wenyao Li, and Wenzhong Shen. "Hydrogels that couple nitrogen-enriched graphene with Ni(OH)<sub>2</sub> nanosheets for high-performance asymmetric supercapacitors." *Journal of Alloys and Compounds* 782 (2019): 516-524.
- [134]. Lo, I-Hsiang, Jun-Yi Wang, Kuo-Yen Huang, Jin-Hua Huang, and Weng P.

Kang. "Synthesis of Ni(OH)<sub>2</sub> nanoflakes on ZnO nanowires by pulse electrodeposition for high-performance supercapacitors." *Journal of Power Sources* 308 (2016): 29-36.

- [135]. Yi, Huan, Huanwen Wang, Yuting Jing, Tianquan Peng, Yiran Wang, Jiang Guo, Qingliang He, Zhanhu Guo, and Xuefeng Wang. "Advanced asymmetric supercapacitors based on CNT@Ni(OH)<sub>2</sub> core-shell composites and 3D graphene networks." *Journal of Materials Chemistry A* 3, no. 38 (2015): 19545-19555.
- [136]. Pu, Zonghua, Qian Liu, Abdullah H. Qusti, Abdullah M. Asiri, Abdulrahman O. Al-Youbi, and Xuping Sun. "Fabrication of Ni(OH)<sub>2</sub> coated ZnO array for high-rate pseudocapacitive energy storage." *Electrochimica Acta* 109 (2013): 252-255.
- [137]. Cho, Er-Chieh, Cai-Wan Chang-Jian, Kuen-Chan Lee, Jen-Hsien Huang, Bo-Cheng Ho, Rou-Zhen Liu, and Yu-Sheng Hsiao. "Ternary composite based on homogeneous Ni(OH)<sub>2</sub> on graphene with Ag nanoparticles as nanospacers for efficient supercapacitor." *Chemical Engineering Journal* 334 (2018): 2058-2067.
- [138]. Naik, Jaya Prakash, Prasanta Sutradhar, and Mitali Saha. "Molecular scale rapid synthesis of graphene quantum dots (GQDs)." *Journal of Nanostructure in Chemistry* 7, no. 1 (2017): 85-89.
- [139]. Li, Songzhan, Jian Wen, Tian Chen, Liangbin Xiong, Jianbo Wang, and Guojia Fang. "In situ synthesis of 3D CoS nanoflake/Ni (OH)<sub>2</sub> nanosheet nanocomposite structure as a candidate supercapacitor electrode." *Nanotechnology* 27, no. 14 (2016): 145401.
- [140]. Wei, Ji Shi, Hui Ding, Peng Zhang, Yan Fang Song, Jie Chen, Yong Gang Wang, and Huan Ming Xiong. "Carbon dots/NiCo<sub>2</sub>O<sub>4</sub> nanocomposites with various morphologies for high performance supercapacitors." *Small* 12, no. 43 (2016): 5927-5934.

## LIST OF PUBLICATIONS

### Journal Publications:

1. Hong, Yiwen, Jingxia Yang\*, WonMook Choi, Jinjie Wang, and Jingli Xu\*. "B-Doped g-C<sub>3</sub>N<sub>4</sub> Quantum Dots-Modified Ni(OH)<sub>2</sub> Nanoflowers as an Efficient and Stable Electrode for Supercapacitors." *ACS Applied Energy Materials* (2021).
2. Hong, Yiwen, Jingli Xu, Jin Suk Chung, and Won Mook Choi\*. "Graphene quantum dots/Ni(OH)<sub>2</sub> nanocomposites on carbon cloth as a binder-free electrode for supercapacitors." *Journal of Materials Science & Technology* 58 (2020): 73-79.
3. Hong, Yiwen, Jingxia Yang, Jingli Xu, and Won Mook Choi\*. "Template-free synthesis of hierarchical NiO microtubes as high-performance anode materials for Li-ion batteries." *Current Applied Physics* 19, no. 6 (2019): 715-720.

## 요약

리튬 이온 전지 및 슈퍼 커패시터의 전기 화학적 특성을 높이기 위해 친환경 공법으로 여러 종류의 전극 소재를 개발했습니다. 하나의 복합 재료는 p 형 반도체의 니켈 산화물 또는 수산화물이고 다른 하나는 양자점의 n 형 반도체입니다. 박사 학위 논문은 니켈 기반 재료와 2D 양자점을 사용하는 복합 재료와 관련된 네 가지 주제를 포함합니다. 복합재는 슈퍼 커패시터 전극 또는 리튬 이온 배터리 양극으로 추가로 사용되었으며, 뛰어난 사이클링 성능을 나타내는 전기 화학 워크 스테이션에서 전기 화학적 특성을 확인했습니다. 첫 번째 부분에서는 주형이나 계면 활성제를 사용하지 않고 층상 나노 구조 전구체  $\alpha$ -Ni(OH)<sub>2</sub> 를 간단한 습식 화학 합성 방법으로 준비한 다음 NiO (h-NiO) 마이크로 튜브로 하소했습니다. Li-ion 배터리의 양극 전극 인 h-NiO 마이크로 튜브는 200 사이클 후 0.5C (1C = 717mA/g)의 전류 밀도에서 770mAh/g 의 크게 향상된 사이클 용량과 98.8%의 매우 높은 컬럼 빅 효율을 제공합니다. 두 번째 부분에서는 붕소 도핑 g-C<sub>3</sub>N<sub>4</sub> 양자점 (B-CNQD)이 KOH 절단에 의해 합성되었습니다. 그런 다음 함 침법에 의해 표면 Ni(OH)<sub>2</sub> 나노 플라워에 흡착됩니다. 최고의 B-CNQD<sub>x</sub>-Ni 샘플은 1.5 A/g 에서 1700 F/g 의 우수한 비 정전 용량을 가지고 있습니다. 세 번째 부분에서는 간단한 열수 반응을 통해 제조된 탄소 천



(G-NH//CC)에 합성 그래핀 양자점 GQD/Ni(OH)<sub>2</sub> 가 있습니다. 최대 비정전 용량은 1 A/g 에서 1825 F/g 이고 높은 에너지 밀도는 2021 W/kg 에서 80.8 Wh/kg 입니다. 마지막으로, Mxene 양자점은 다른 용매를 사용하여 마이크로파 보조제와 열수 반응을 통해 합성되었습니다. 최고의 MQD-Ni/Ni 폼 샘플은 1 A/g 에서 1660 F/g 의 뛰어난 비 용량을 가지고 있습니다.